2

CR 114508
AVAILABLE TO THE PUBLIC

(NASA-CR-114508) DENSITY AND OPTICAL PROPERTIES OF SPARCS PLUMES W.A. Brown, et al (Lockheed Missiles and Space Co.) Nov. 1972 110 p CSCL 21B

N73-12958

G3/33 Unclas 48055

Lockheed

MISSILES & SPACE COMPANY, INC.

A SUBSIDIARY OF LOCKHEED AIRCRAFT CORPORATION

SUNNYVALE, CA

NASA CR114508

Available to the Public

DENSITY AND OPTICAL PROPERTIES OF SPARCS PLUMES

By

William A. Brown
John B. Kumer
Charles E. Cooper, Jr.

November 1972

Prepared Under Contract No. NAS2-6573 by
Lockheed Palo Alto Research Laboratory
Palo Alto, California 94034

For

Ames Research Center
National Aeronautics and Space Administration

TABLE OF CONTENTS

DENSITY AND OPTICAL PROPERTIES OF SPARCS PLUMES

By

William A. Brown
John B. Kumer
Charles E. Cooper, Jr.*

Lockheed Palo Alto Research Laboratory
and*Lockheed Huntsville Research Center

SUMMARY

Propellant gases emitted by attitude control systems such as SPARCS (Solar Pointing Aerobee Rocket Control System) may interfere with experiments aboard the payloads. This report surveys the optical properties of seven actual and potential gases emitted by propellant systems (CF_4, N_2H_4, NH_3, N_2, CO_2, Ar, and He) and provides a compilation of absorption coefficients from 1A to 50 μm and a summary of fluorescent spectra and efficiencies. Since Freon-14 (CF_4) is of primary importance to SPARCS, an experimental search for the fluorescent spectrum of CF_4 was performed by exciting the gas with 920Å UV photons. The result was compared with an electron impact induced spectrum of CF_4, and conclusions drawn about the nature of the radiating species. A detailed study of the CF_4 flow fields and plume densities for typical SPARCS controlled payloads was made using gas dynamic codes which included the effects of vehicle shading and condensation. The importance of the optical properties of CF_4 plumes was investigated and it is concluded that absorption is negligible but fluoresence may be significant in some cases.

I. INTRODUCTION

Propellant gases emitted by attitude control jets on SPARCS or other control devices for rockets or satellites may interfere with on-board experiments. The purpose of the investigations reported here was to estimate the importance of this potential interference, and to provide data upon which a quantitative assessment of interference can be made. The SPARCS system is designed to provide attitude control for Aerobee and other rockets by a combination of solar pointing and magnetic roll stabilization, thus avoiding the use of gyros.

Attitude control is provided by eight pulsed thrust nozzles. The length and frequency of the pulses determines the net torque on the rocket payload. The centerlines of the SPARCS thrust nozzles lie in planes perpendicular to the roll axis of the roll axis of the rocket and most of the gas emitted is directed away from the sides of the vehicle. A study of the density distribution (Section III) reveals that some gas appears ahead of the payload. The implications of this for optical experiments are discussed in Section IV. Gases can interfere with on-board experiments in three ways. One of these, direct interaction with optical surfaces or other instrument components is not discussed here. The absorption of radiation and fluorescence due to illumination of the gases by sunlight is the subject of Sections II and IV.

II. OPTICAL PROPERTIES OF GASES

Gases emitted by attitude control systems have two potential means of interfering with optical experiments on the payload. They can absorb light in specific spectral intervals and they can scatter light or fluoresce. Information on the molecular and atomic properties of seven gases are included. These are CF_4 (freon-14), N_2H_4 (hydrazine), NH_3 (ammonia), CO_2 (carbon dioxide), Ar (argon), N_2 (nitrogen), and He (helium).

1. Absorption Coefficients

Absorption coefficient data for gases of present and potential future importance for pointing control systems are presented in this section and Appendix A. These data were compiled from a number of sources listed in the references and cited in Appendix A. This section treats the absorption coefficient data of the individual molecules. The absorption of the gas clouds output by the SPARCS pointing control systems is discussed in Section IV, where estimates of gas density are combined with absorption coefficient data.

The absorption coefficient data presented for the molecules considered in this study contain both continuous and discrete spectra. There is a fundamental difference in the interpretation of the data depending upon whether the spectra are discrete or continuous. All the atoms and molecules have a continuous absorption spectrum in the x-ray region at wavelengths of from one to several hundred angstroms, interrupted by a number of discrete edges. In the vacuum UV region of the spectrum from the mid hundreds to

about two thousand angstroms there are both continuua and discrete line and band spectra. The molecules and atoms are essentially transparent in the visible and again show discrete absorption spectra in the near and far infrared. For each of the gases considered in this study, a chart or graph was prepared spanning the wavelength region from one angstrom to fifty microns (1Å = 10^{-8} cm, 1 micron = 10^{-4} cm). In cases where the absorption coefficient is continuous it is plotted as a function of wavelength, but in cases where discrete lines and bands exist, it is inconvenient and sometimes misleading to plot absorption coefficient. Supplementary graphs and tables are used to display details of the absorption coefficient data in selected spectral intervals.

The absorption coefficient is given in units of cm^{-1} atm^{-1}, usually abbreviated simply as cm^{-1}, and is simply related to the absorption cross section, σ cm^2, at a particular frequency by the factor 2.687×10^{19} particles/cm^3 atm, Loschmidt's number. In the case of a discrete transition in an atom or molecule, the quantity that is usually measured is the integral of the absorption coefficient over a wavelength interval which includes all or part of the line or band in question. This integral is a constant for each molecule depending on internal quantum mechanical properties of the atom or molecule. The oscillator strength or f-number of a discrete transition is related to the integral of the absorption cross section, σ, by:

$$\int \sigma \, d\nu = \frac{\pi e^2}{mc} \, f \qquad (1)$$

where $\pi e^2/mc = 0.0266$ cm^2/sec, and ν is the frequency in Hz, where $\lambda\nu = c$.

To illustrate the problem of presenting absorption coefficient data for lines or bands, consider the resonance absorption line of the helium atom at 584Å. The dimensionless f-number for this transition is 0.26 corresponding to an Einstein spontaneous transition probability of 18×10^8 transitions per second. The absorption cross section for this line is given by unfolding the integral of equation 1. To do this, let σ_o be the value of the function $\sigma = \sigma(\nu)$ at the line center. It depends on the shape of the absorption line, which depends in turn on the particle velocity or kinetic temperature and the pressure, or where these are small, the lifetime of the excited state of the atom. Two cases are worked out as examples. Consider the helium atom in free space at zero temperature. The width of the absorption line at 584Å will be determined solely by its natural line width which is, in frequency units, 1.8×10^9 Hz. Replacing the left-hand side of equation 1 by the product of this frequency interval and an average cross section yields $\sigma_o = 4 \times 10^{-12}$ cm^2. Now consider a gas of helium atoms at 200 degrees Kelvin. The shape of the absorption line will be dominated by Doppler broadening which is the result of random kinetic motion of the atoms. The full Doppler line width at half maximum at 200°K for the helium 584Å line is 2.5×10^{10} Hz so that an estimate of the absorption cross section at line center for this case is 3×10^{-13} cm^2, an order of magnitude smaller than the cross section for an atom at zero kinetic temperature. In both cases the integral of the absorption coefficient or cross section over frequency or wavelength is the same and only the shape and height of the function $\sigma(\nu)$ differs.

Figures 1 through 7 give absorption coefficient data for the gases studied over the spectral range from soft x-ray to far infrared.

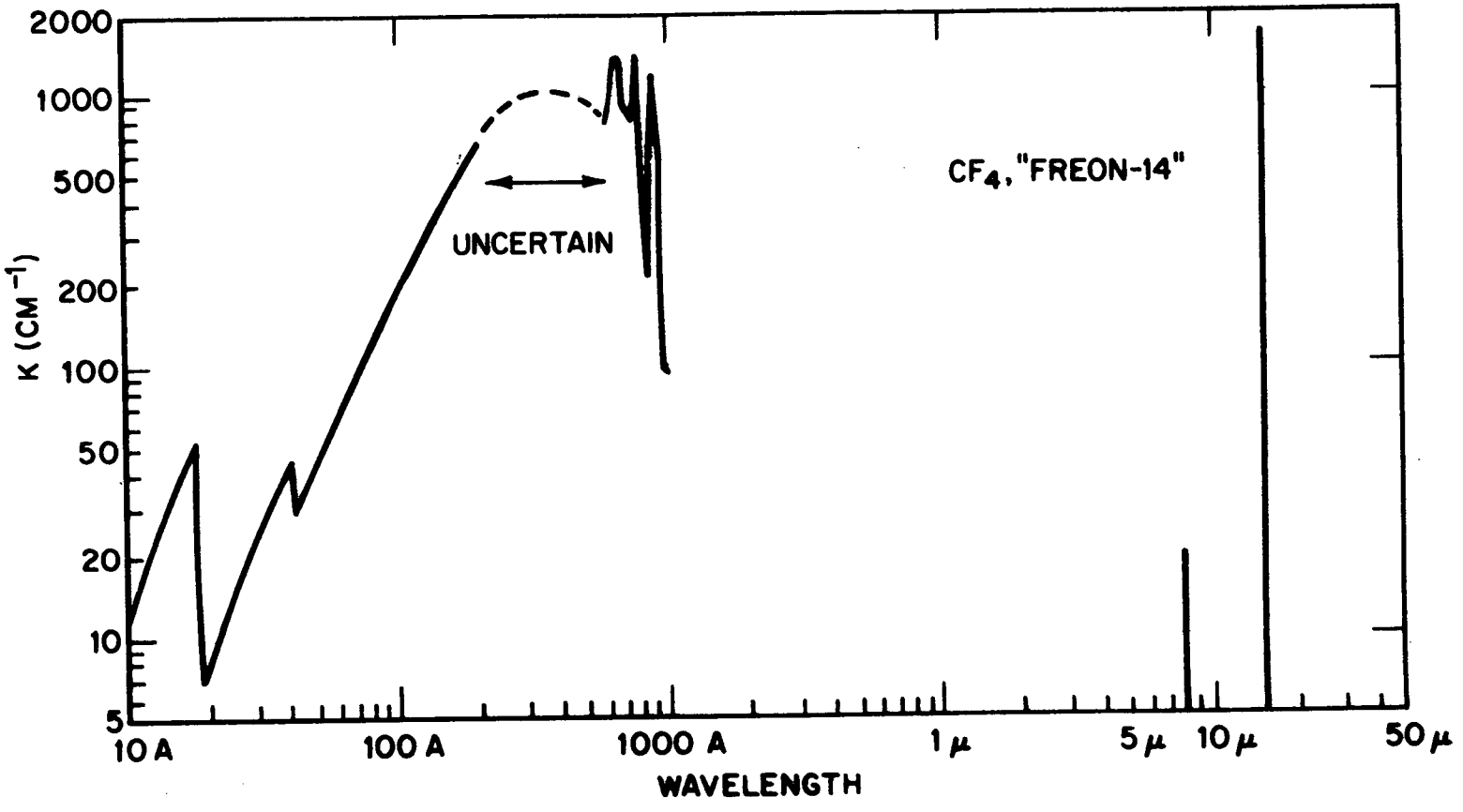

Figure 1 Absorption Coefficient of CF_4

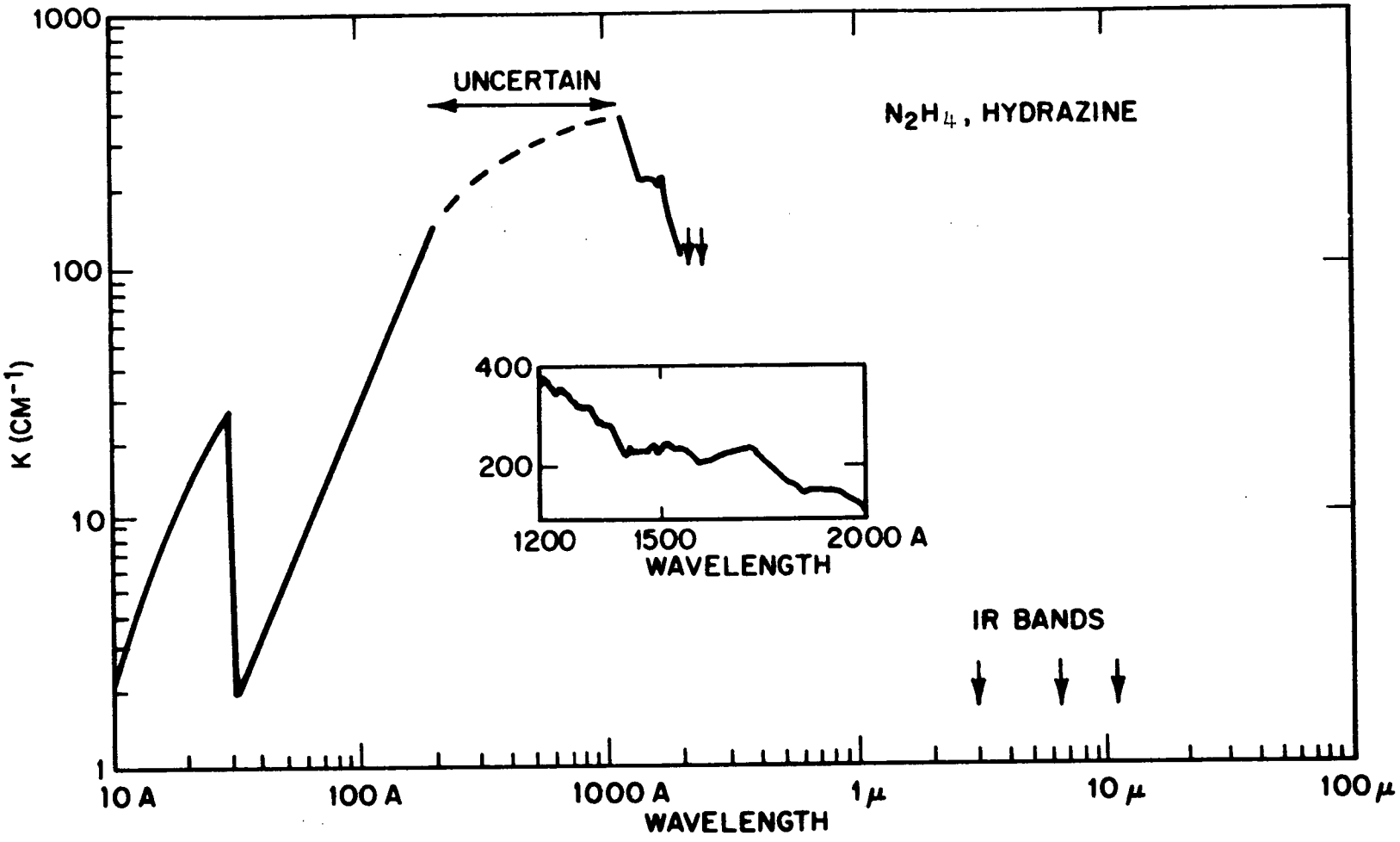

Figure 2 Absorption Coefficient of N_2H_4

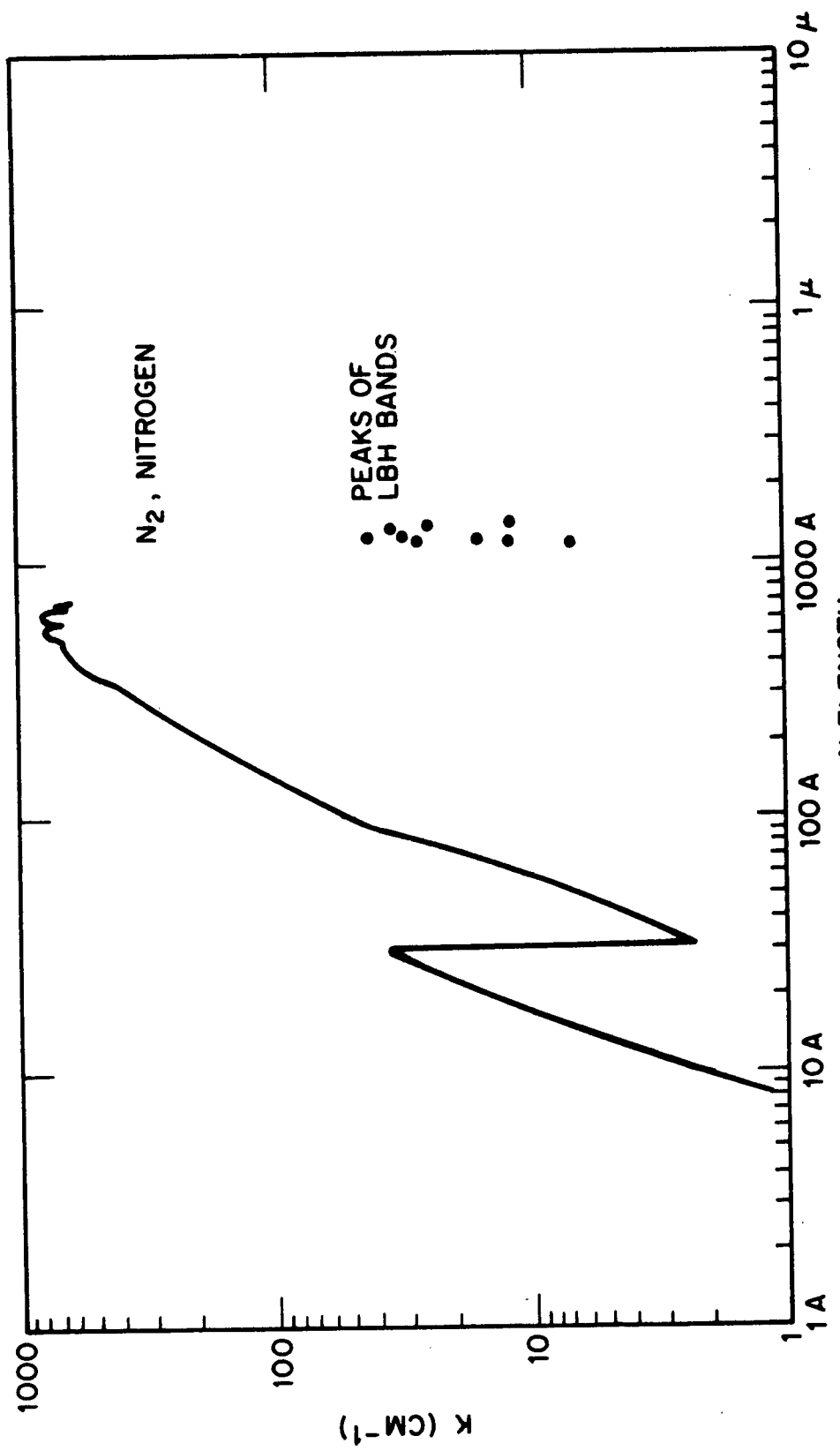

Figure 3 Absorption Coefficient of N_2

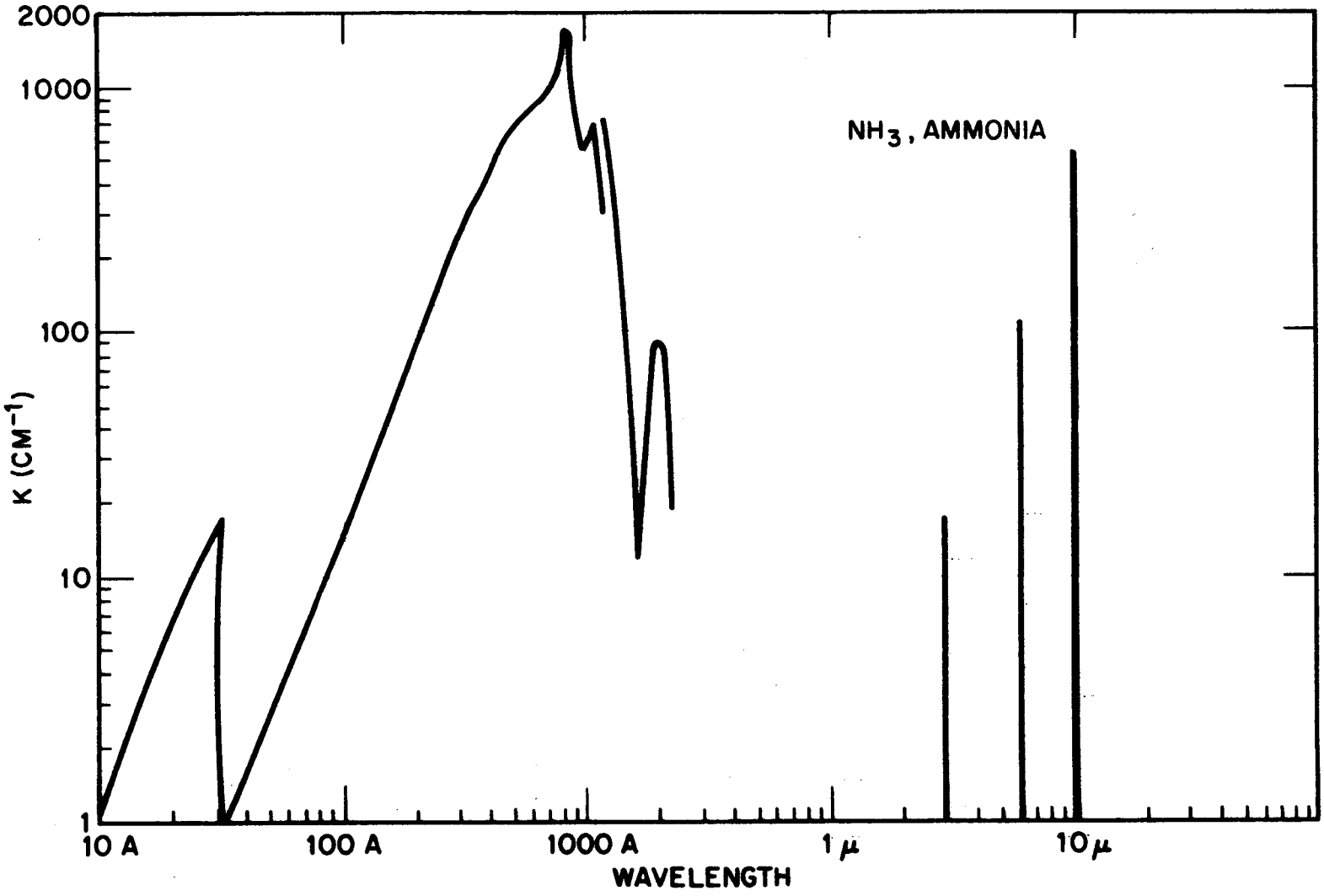

Figure 4 Absorption Coefficient of NH_3

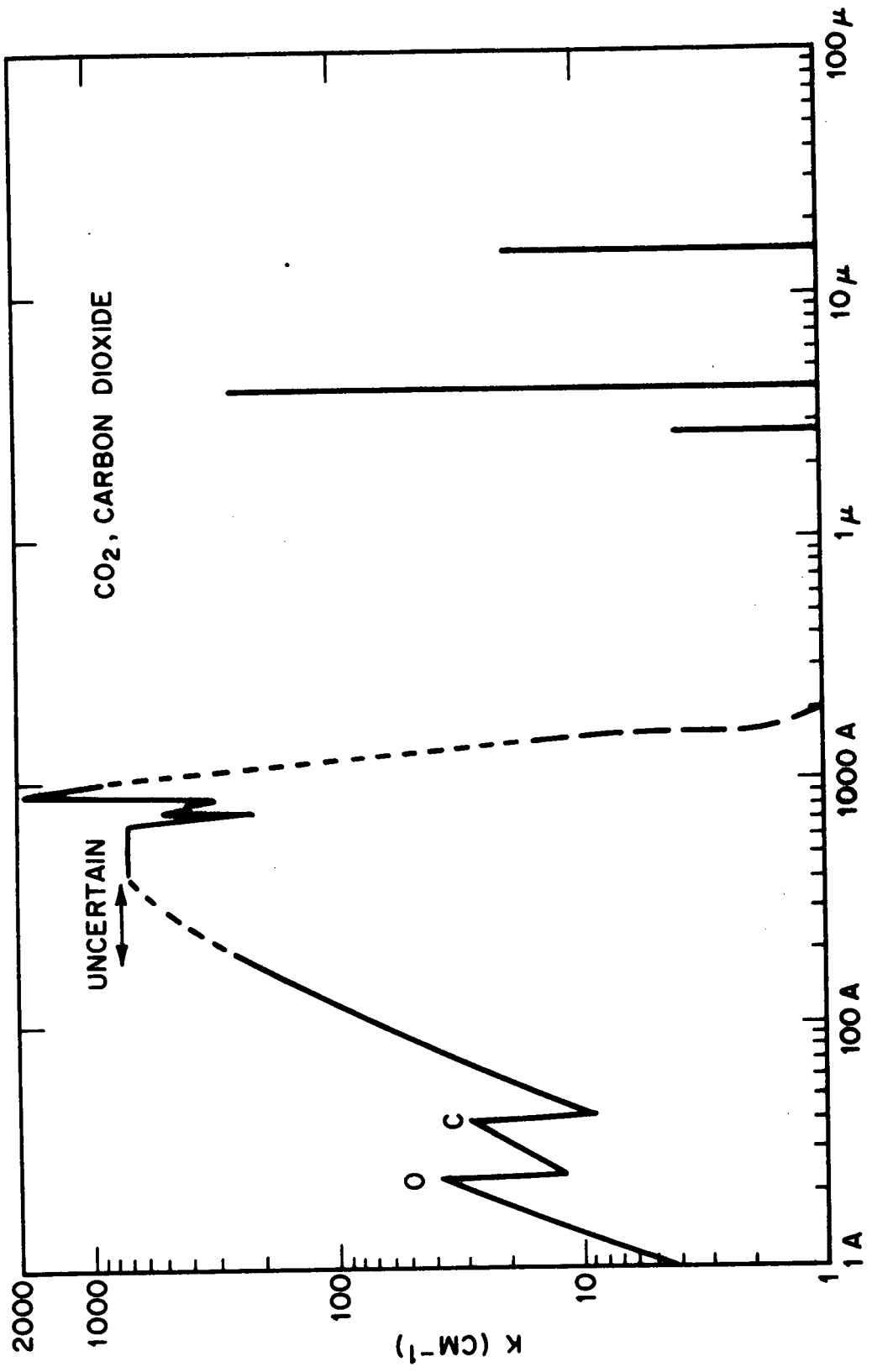

Figure 5 Absorption Coefficient of CO_2

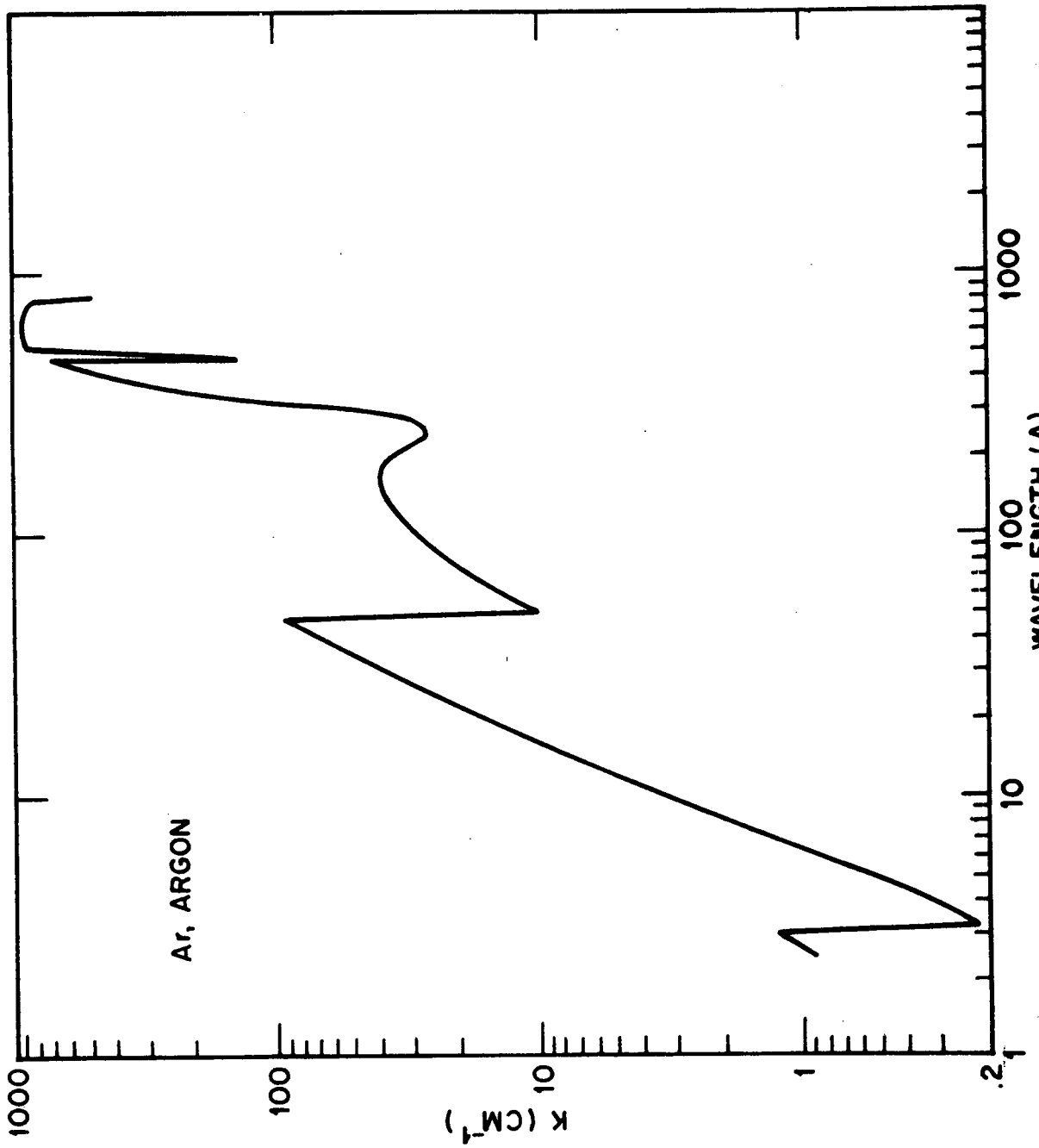

Figure 6 Absorption Coefficient of Ar

B

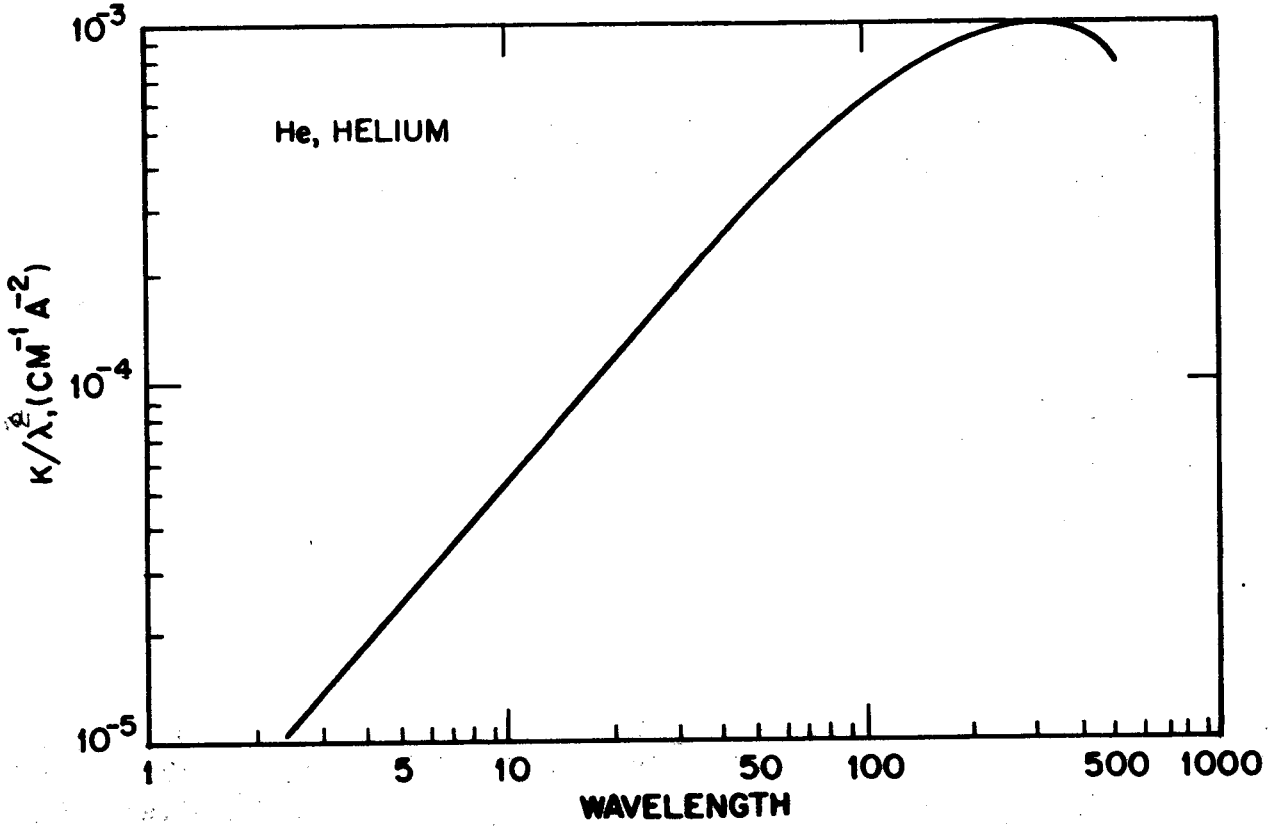

Figure 7 Absorption Coefficient Divided by Square of Wavelength for Helium (Extreme variation of K with wavelength makes these units preferable in this case)

Additional details on absorption coefficients for most of the gases studied are contained in Appendix A, along with reference citations for the original data.

2. Fluorescence

The plume or gas cloud may be both in the field of view of the experiment and illuminated by radiation from the sun or earth. Solar radiation dominates in the visible, uv, and near infrared. While at wavelengths greater than 5 microns the earth provides greatest irradiance at rocket or satellite altitudes.

Molecules in the gas cloud may absorb radiation in the visible or uv and re-emit in both visible and infrared. For example, freon, CF_4, absorbs vacuum uv radiation in a broad band near 900 Angstroms and emits fluorescent radiation at wavelengths < 3000Å.

In the infrared, scattering of the earth's or the payload's thermal radiation may interfere with instruments designed to detect such radiation.

The fluorescence spectra of the molecules considered in this study are discussed in Appendix B. The importance of CF_4 as a propellant and the lack of detailed fluorescence data on this molecule led to a requirement for experimental work which is described in Appendix C. This gives, for the first time, the fluorescence spectrum of CF_4 when excited by photons

of wavelength near 900Å. Some questions have been answered by the experimental investigations completed thus far on fluorescence of CF_4, but some new problems have arisen. Most important among these is the possibility that CF_4 may fluoresce when irradiated with photons of wavelength shorter than 600Å. Cook and Ching (ref. 1) did not use wavelengths shorter than 600Å and so could not provide information on either absorption or fluorescence in the region <600Å. The electron excitation experiments showed that low energy electrons excite the same fluorescence as that excited by 900Å photons. It also showed that electrons of energy greater than 22 eV excite, with high efficiency, fluorescence at 1600Å in addition to the large amounts of fluorescence between 1850 and 3000Å. Whether photons of wavelength less than 600Å also excite these fluorescent signals is not known. Experimental work at shorter wavelengths would resolve this question.

In addition to the detailed discussion of fluorescence in Appendix B, some examples are given here. The fluorescent spectrum of CF_4 is shown in Figure 8. The significant part of the spectrum lies between 2100 and 3100Å. Section IV gives estimates of the intensity of this spectrum in a sunlight illuminated gas plume.

The spectrum of sunlight illuminated hydrazine products was observed from Mariner 7 with a high resolution spectrometer. Figure 9 from ref. 2 gives this spectrum from 1200 to 4300Å. The martian atmosphere itself provides an example of a fluorescent spectrum of sunlight on CO_2 and Figures 10 and 11 from ref. 3 are examples.

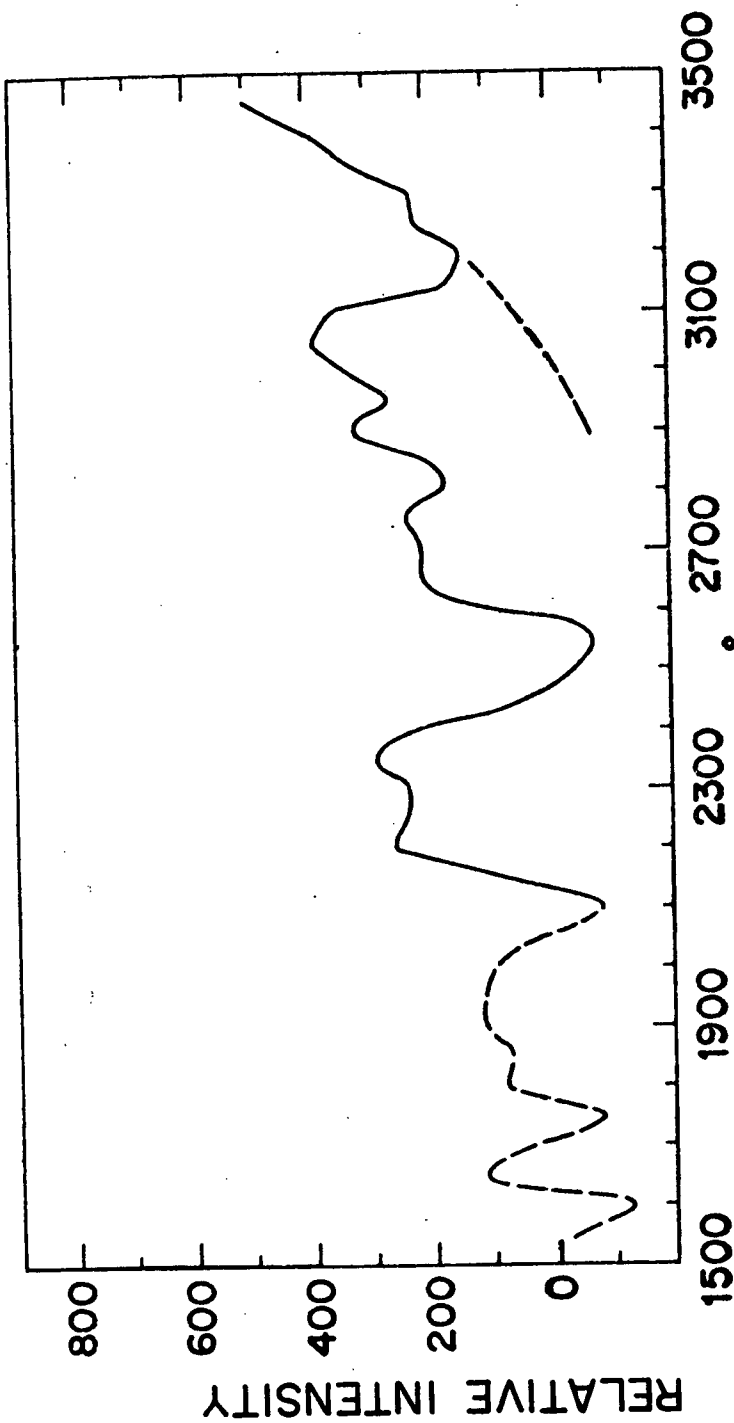

Figure 8 Fluorescence Spectrum of CF_4

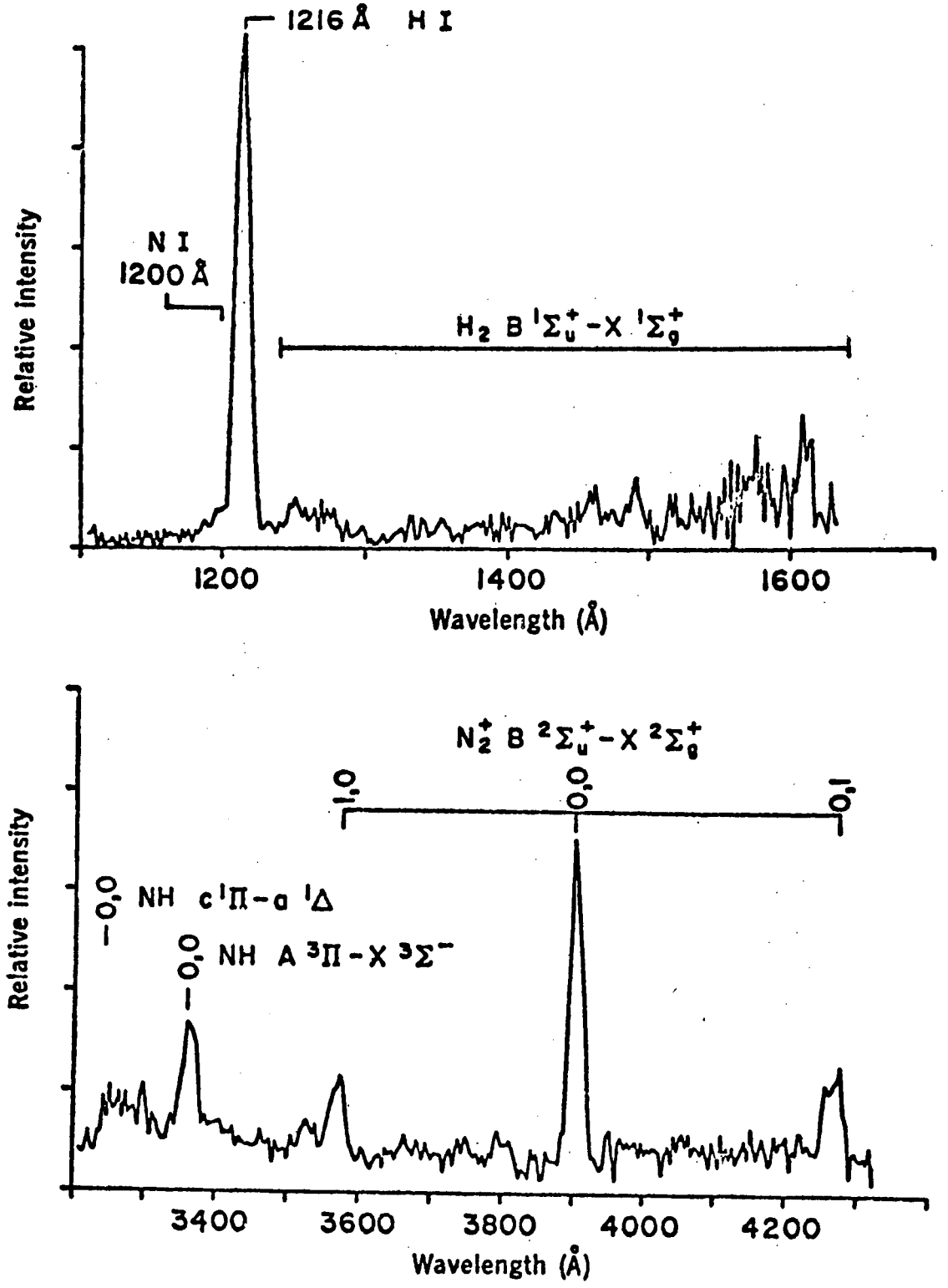

Figure 9 Fluorescence Spectrum of Hydrazine Products

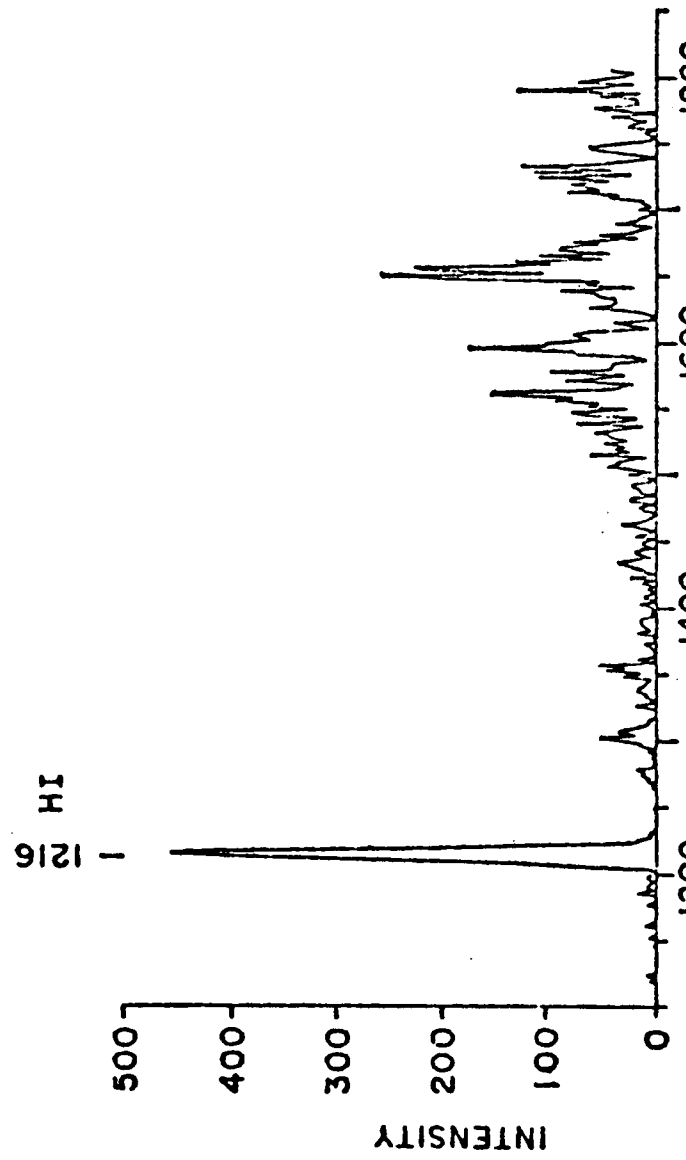

Figure 10 Fluorescence Spectrum of Mars

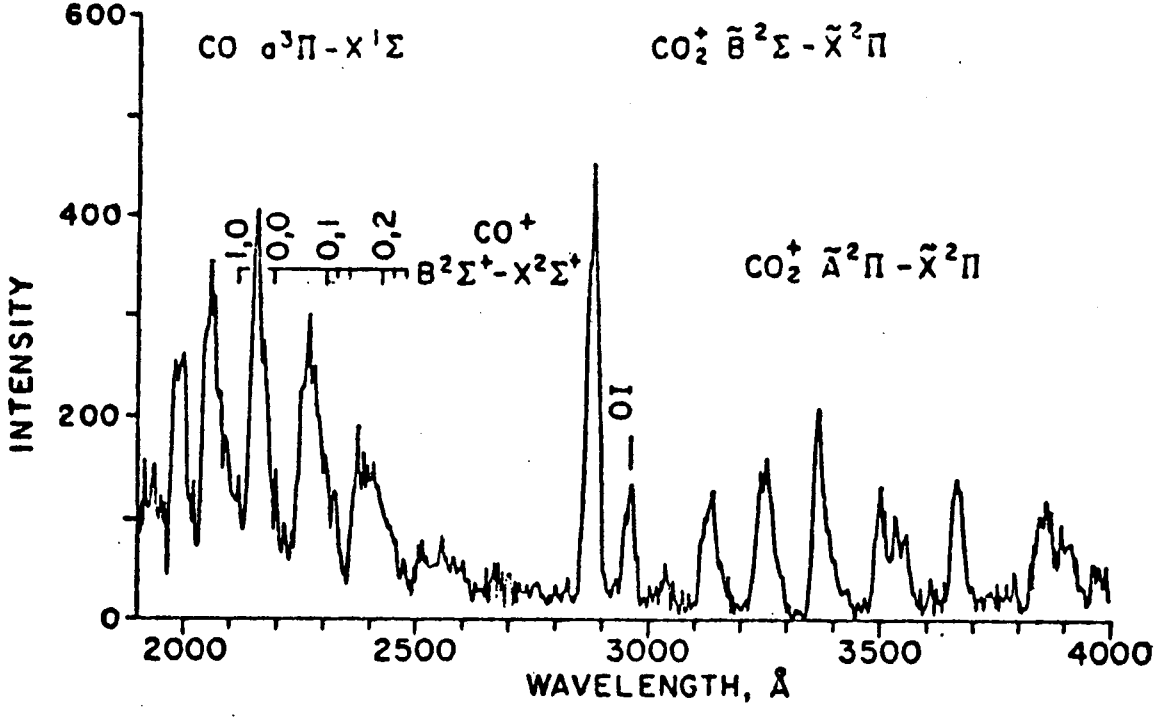

Figure 11 Fluorescence Spectrum of Mars

III. DENSITY DISTRIBUTION OF SPARCS PLUMES

An analysis of the exhaust plume density profiles of the SPARCS motors has been conducted for the following six possible operating conditions:

Combustion Chamber Pressure (psia)	Combustion Chamber Temperature (^{o}R)	$\%CF_4$	$\%N_2$
*25.0	526.0	100	0
25.0	526.0	90	10
25.0	526.0	75	25
*800.0	526.0	100	0
800.0	526.0	90	10
800.0	526.0	75	25

* Primary Operating Modes

SPARCS uses a 10:1 area ratio motor with a 15^{o} half angle and a throat diameter of .044 in. Figure 12 shows the motor arrangement, motor numbering system and the primary area of interest in determining the density profiles. The analysis was conducted for flight conditions corresponding to those of free space. The source flow plume and plume impingement computer programs were used to calculate the steady state continuum and free molecular flow field properties with payload shading being taken into account (refs. 4 and 5). The possibility of condensation in the exhaust plumes was examined by use of the multi-specie heterogeneous condensation computer program (ref. 6).

A value of the Knudson number (Kn) equaling .8 was used as the criterion for determining the point at which the flow became free molecular. In the free molecular region, it was assumed that the molecules traveled along straight lines at a constant temperature and velocity. The source flow

plume program calculated the plume density using the assumption that the density is inversely proportional to the streamtube cross-sectional area.

Vehicle shading effects were determined by using the source flow impingement program which considers the vehicle size and location relative to the motor nozzle. Vector relationships were then used to determine whether the flow streamline would intersect the body and be reflected out into space or whether the flow would miss the body and proceed into the region directly in front of the vehicle.

The extremely low temperatures and pressures which occur in the plume when it expands in deep space makes it necessary to ascertain whether condensation would take place in the flow and if so to determine how this would affect the plume density level. This calculation was performed by using the heterogeneous multi-specie condensation program which assumes one-dimensional flow and determines if condensation takes place. Equations describing nucleation were derived following the classical approach for each specie in the system, using the specie properties at the flow temperature and its partial pressure found by Dalton's law. The equations describing the droplet growth (taking place after nucleation has created a droplet of sufficient size) were derived by allowing molecules of any specie which has crossed its vapor pressure curve to stick onto droplets present in the system. Mass accumulation is accounted for through a mass growth equation. The relationship between flow and condensate is through the mixture density which is used in the continuity and momentum equations. Mixture density is a function of mass fraction of condensate and gas density. This relationship

allows the equation of state to be solved in terms of either gas density or mixture density. The energy exchange between the gas and condensate is accounted for in the flow energy equation through the condensate latent heat term and the thermal energy difference between condensate and flow. The computations showed that no condensation was predicted for any of the cases investigated. The P_c = 800 psia case with pure CF_4 did predict a small amount of nucleation beginning at a point 0.178 inches downstream of the nozzle throat but the droplets are predicted to never reach the critical drop radius. As a consequence, they evaporate as rapidly as they are formed. Also, after having performed these calculations, it can be stated that no condensation would be expected for a CF_4/N_2 mixture with a 526°R chamber temperature for any chamber pressure less than 800 psia.

Computations of CF_4 plume densities were made for the payload geometry shown in Fig. 12. There are three distinct nozzle locations; roll (1 and 3), yaw (4 and 6) and shaded yaw (2 and 5). The latter lie astern of a block containing two roll nozzles and their flow is shaded from the front of the payload. For each of the three nozzle types, plume densities are plotted in planes containing the rocket axis at angles, θ, listed in Table 1.

Figures 13-24 provide data for pure CF_4 flows, with chamber pressure 25 psi and temperature 525°R (Rankine) (292°K).

In order to assess the effects of possible changes in the SPARCS RCS system the following section is presented. Variations of the RCS

Table 1

Figure Numbers of Density Plots

	Angle Plane of Plot Makes with Axis of Nozzle 2				
	$\theta = 40^\circ$	70°	100°	130°	90°
Nozzle 6 Unshaded Yaw	Fig. 13	16	19	22	12a
Nozzle 5 Shaded Yaw	14	17	20	23	
Nozzle 3(up) Roll	15	18	21	24	

Densities are in units of slugs/ft^3, where 10^{-10} slug/ft^3 = 6.5 x 10^{11} molecules/cm^3 for CF_4.

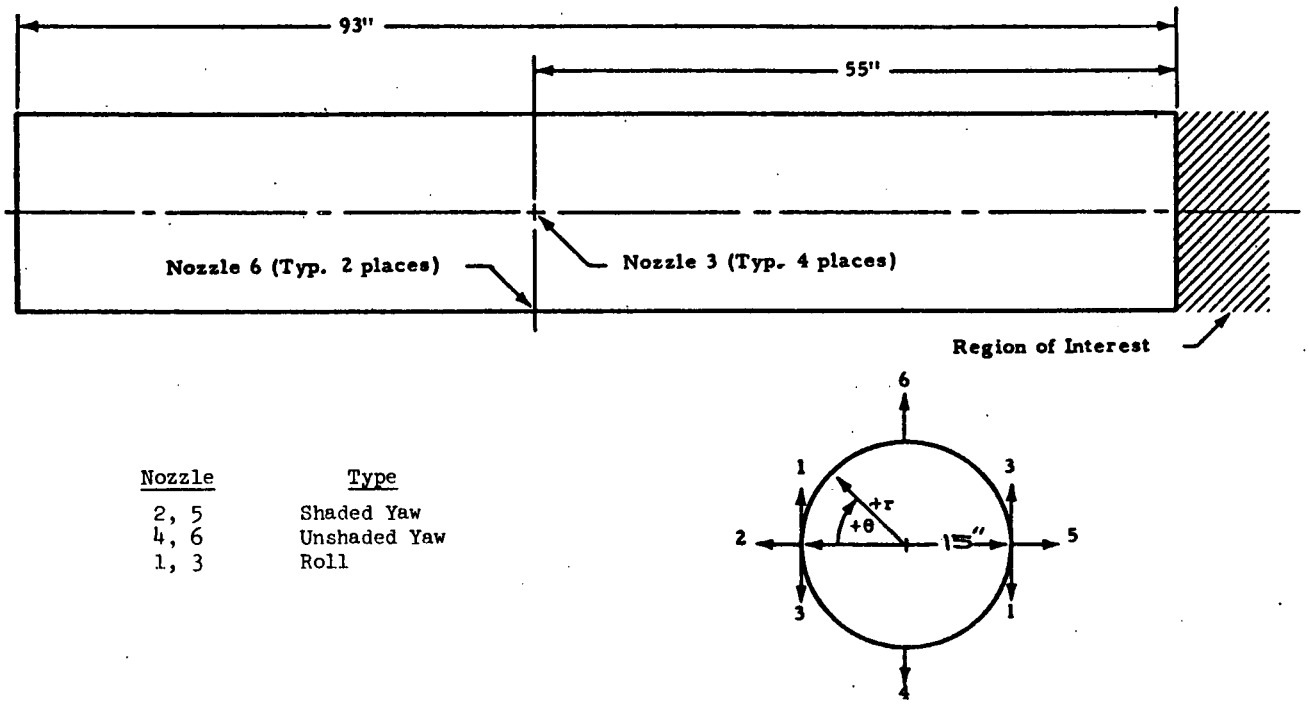

Fig. 12 Schematic showing positions of propulsion nozzles

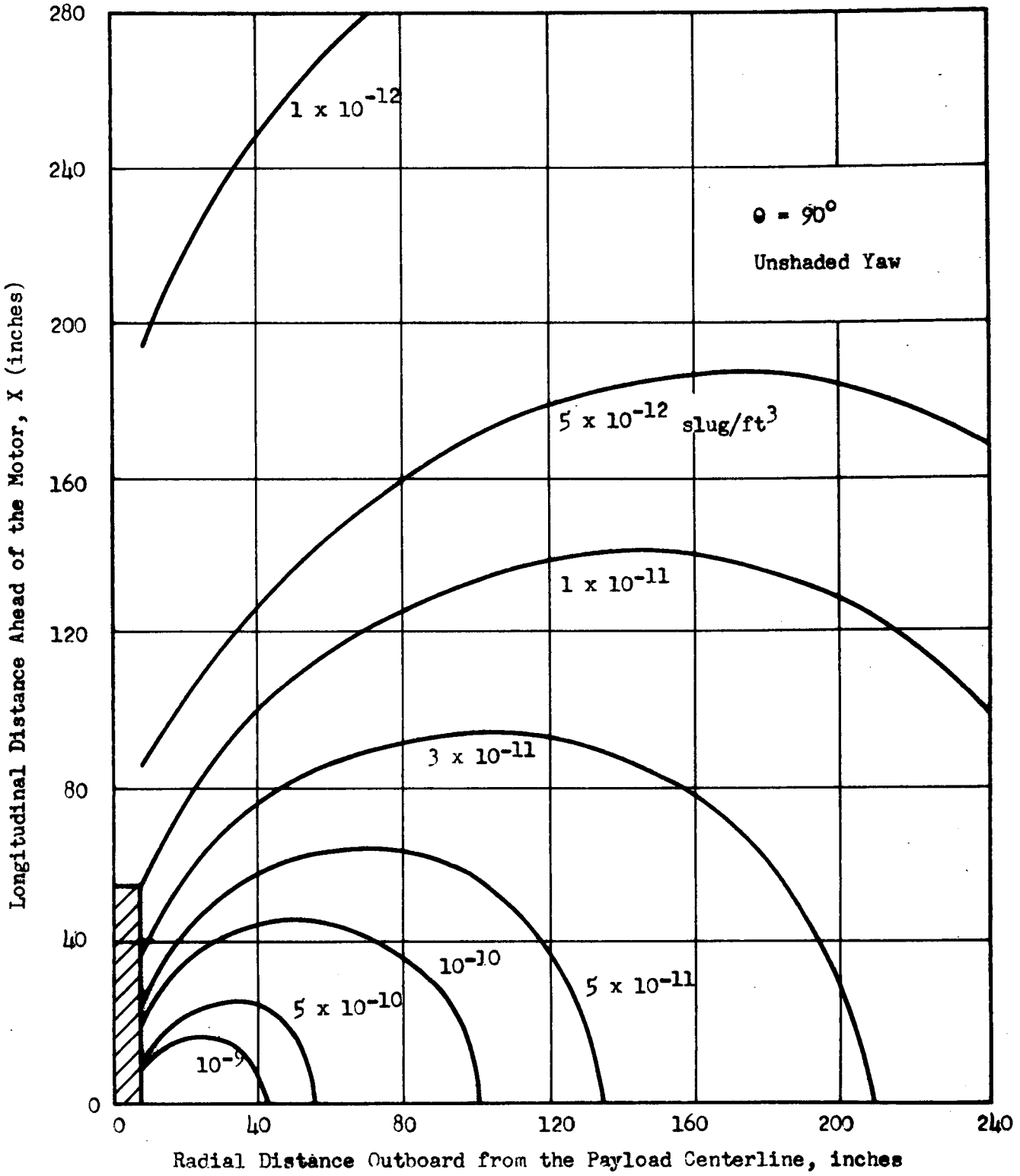

Fig. 12a SPARCS Reaction Control System Plume Density Contours as a Function of Axial and Radial Distance from the Surface of the Vehicle. (Unshaded Yaw, θ = 90 deg; P_c=25 psia; T_c= 525° R)

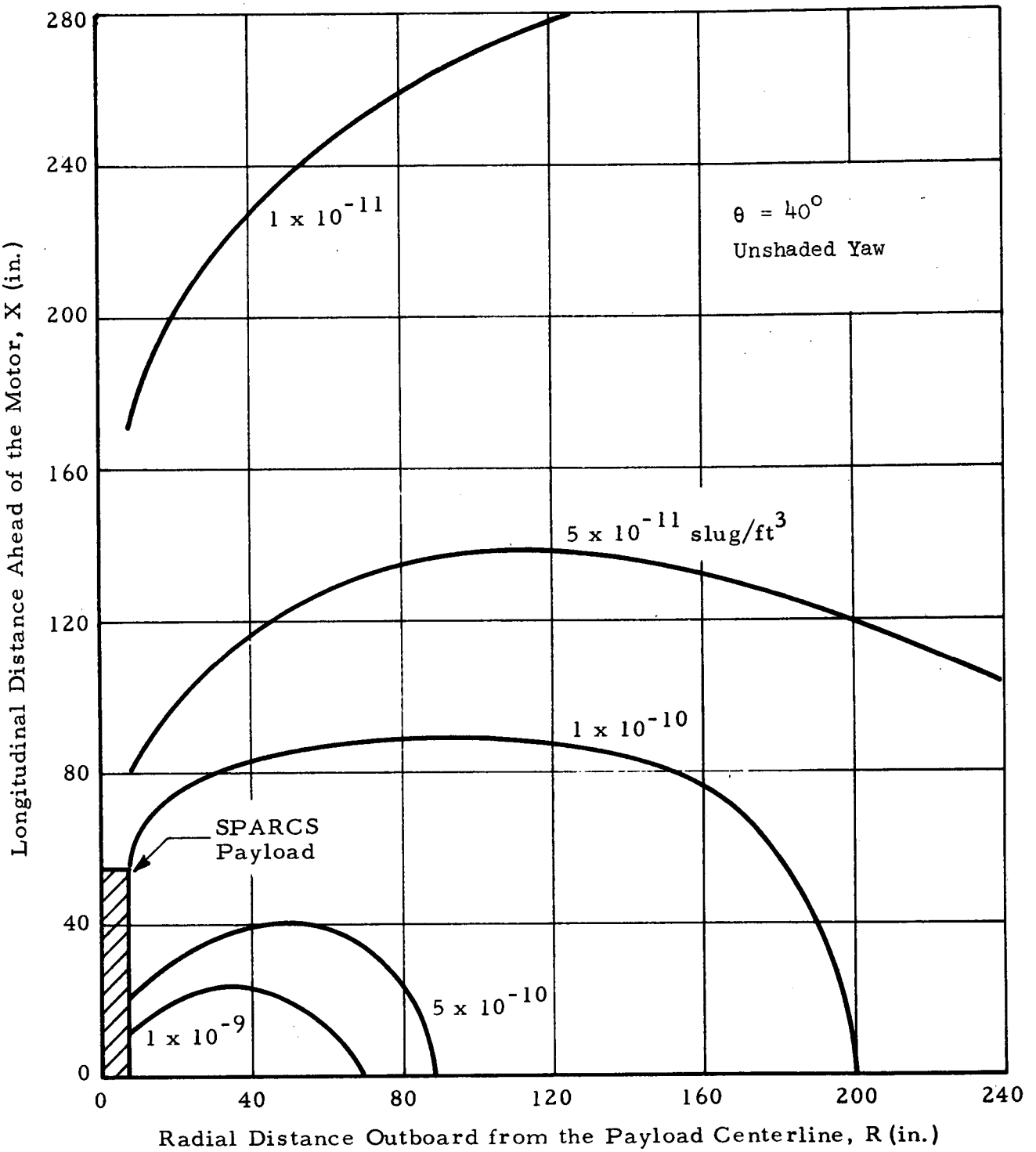

Fig. 13 SPARCS Reaction Control System Plume Density Contours as a Function of Axial and Radial Distance from the Surface of the Vehicle (Unshaded Yaw, θ = 40 deg; P_c = 25.0 psia; T_c = 525°R)

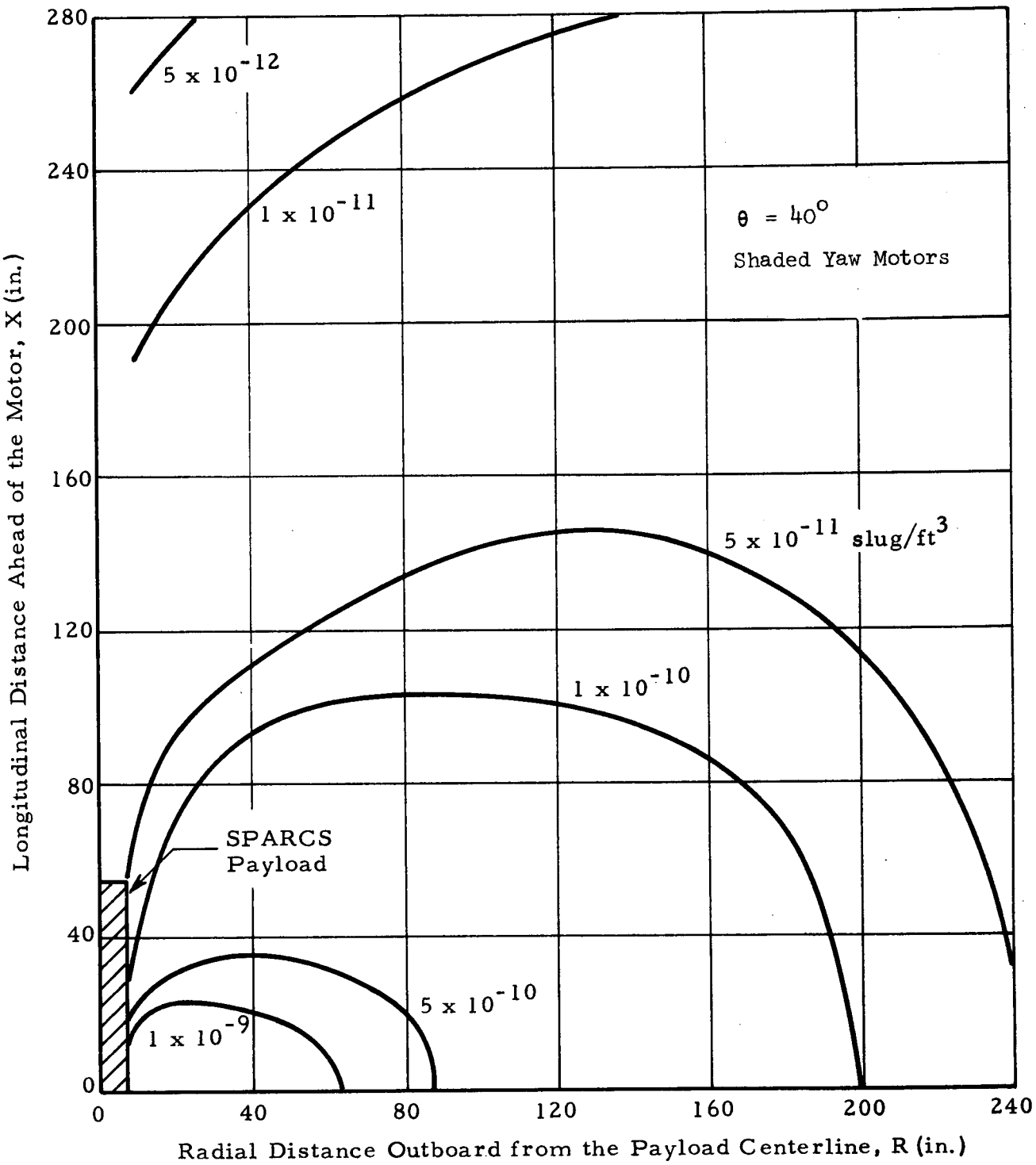

Fig. 14 SPARCS Reaction Control System Plume Density Contours as a Function of Axial and Radial Distance from the Surface of the Vehicle (Shaded Yaw Motors, θ = 40 deg; P_c = 25.0 psia; T_c = 525°R)

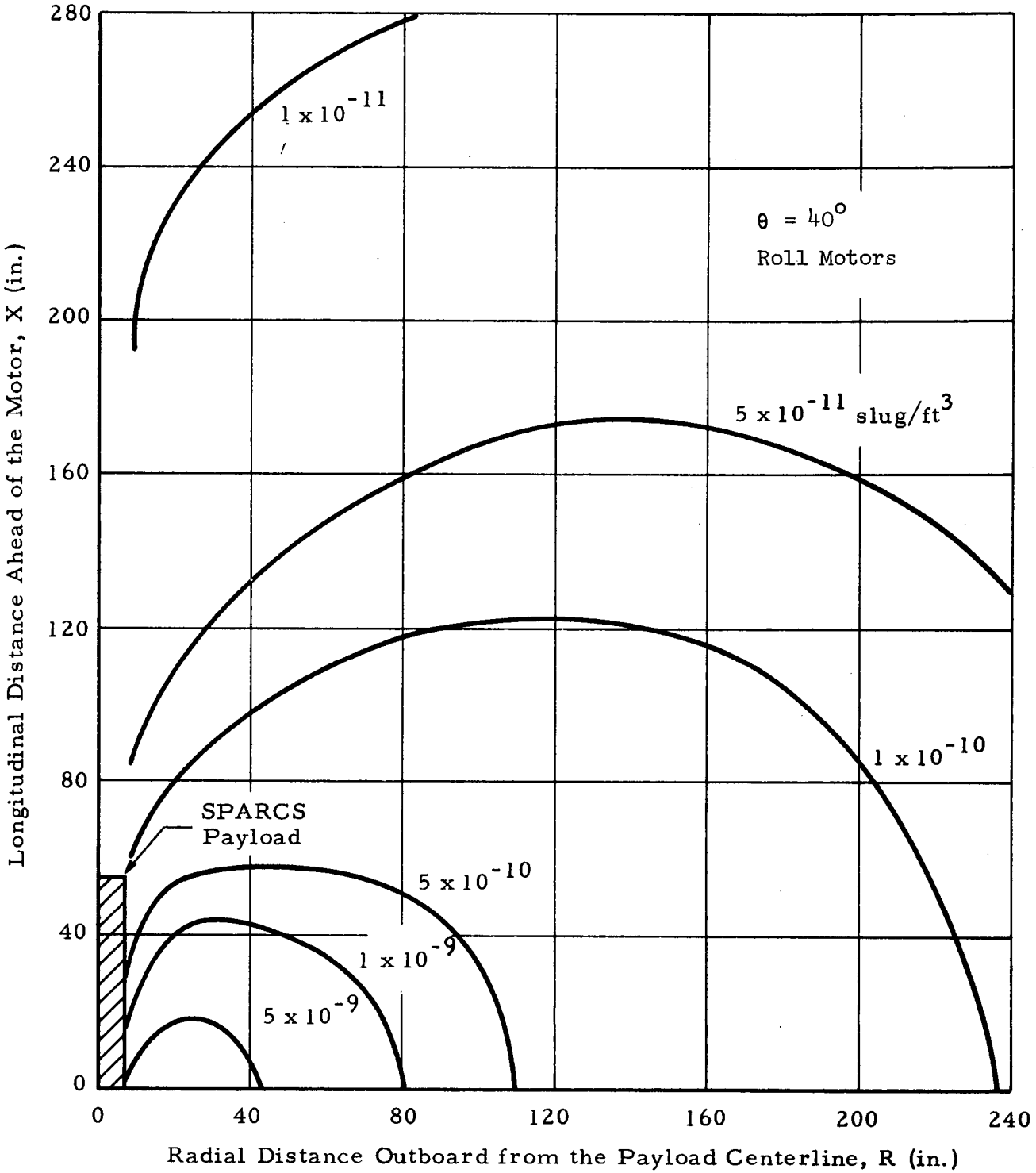

Fig. 15 SPARCS Reaction Control System Plume Density Contours as a Function of Axial and Radial Distance from the Surface of the Vehicle (Roll Motors, θ = 40 deg; P_c = 25.0 psia; T_c = 525°R)

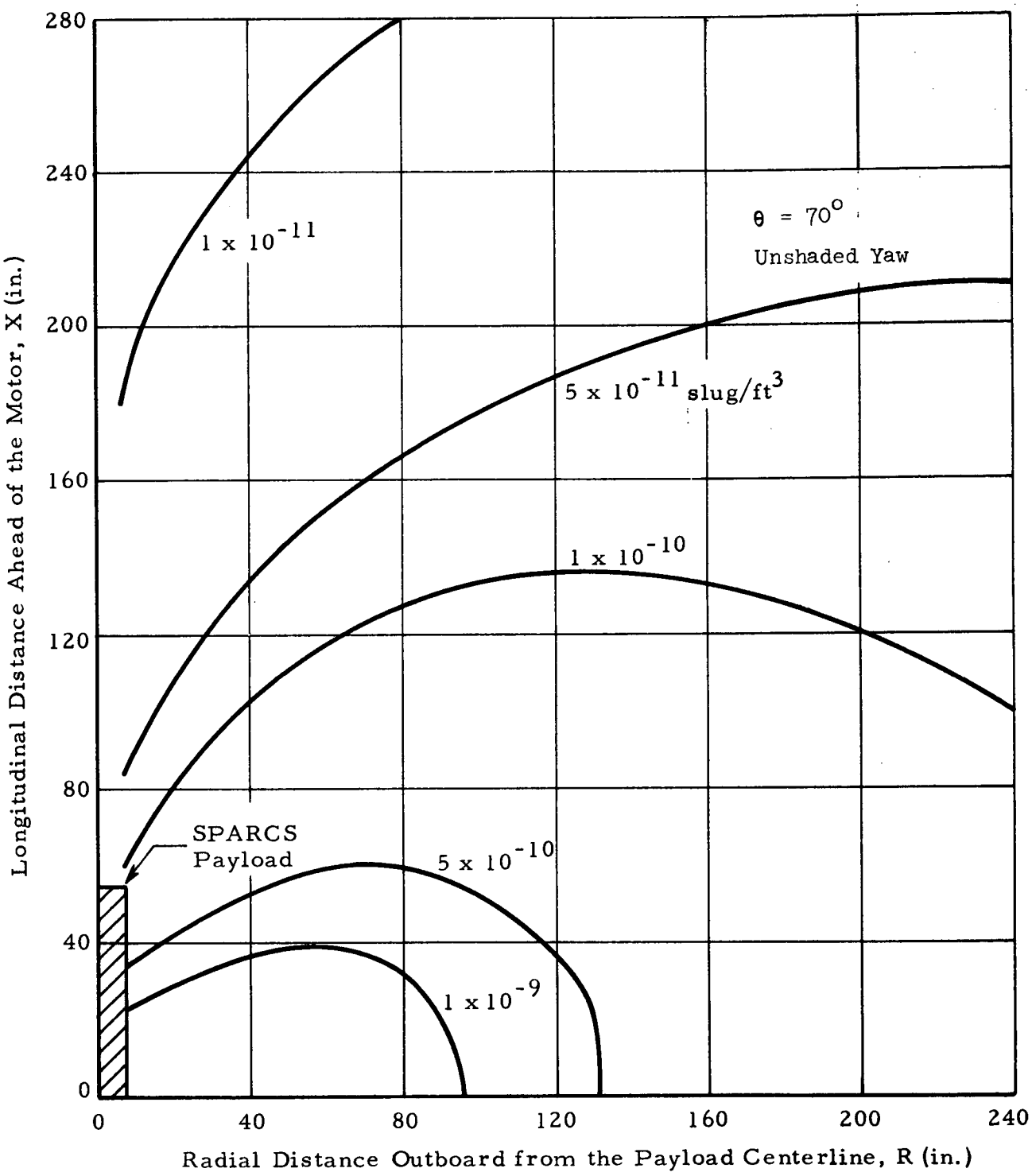

Fig. 16 SPARCS Reaction Control System Plume Density Contours as a Function of Axial and Radial Distance from the Surface of the Vehicle (Unshaded Yaw, θ = 70 deg; P_c = 25.0 psia; T_c = 525°R)

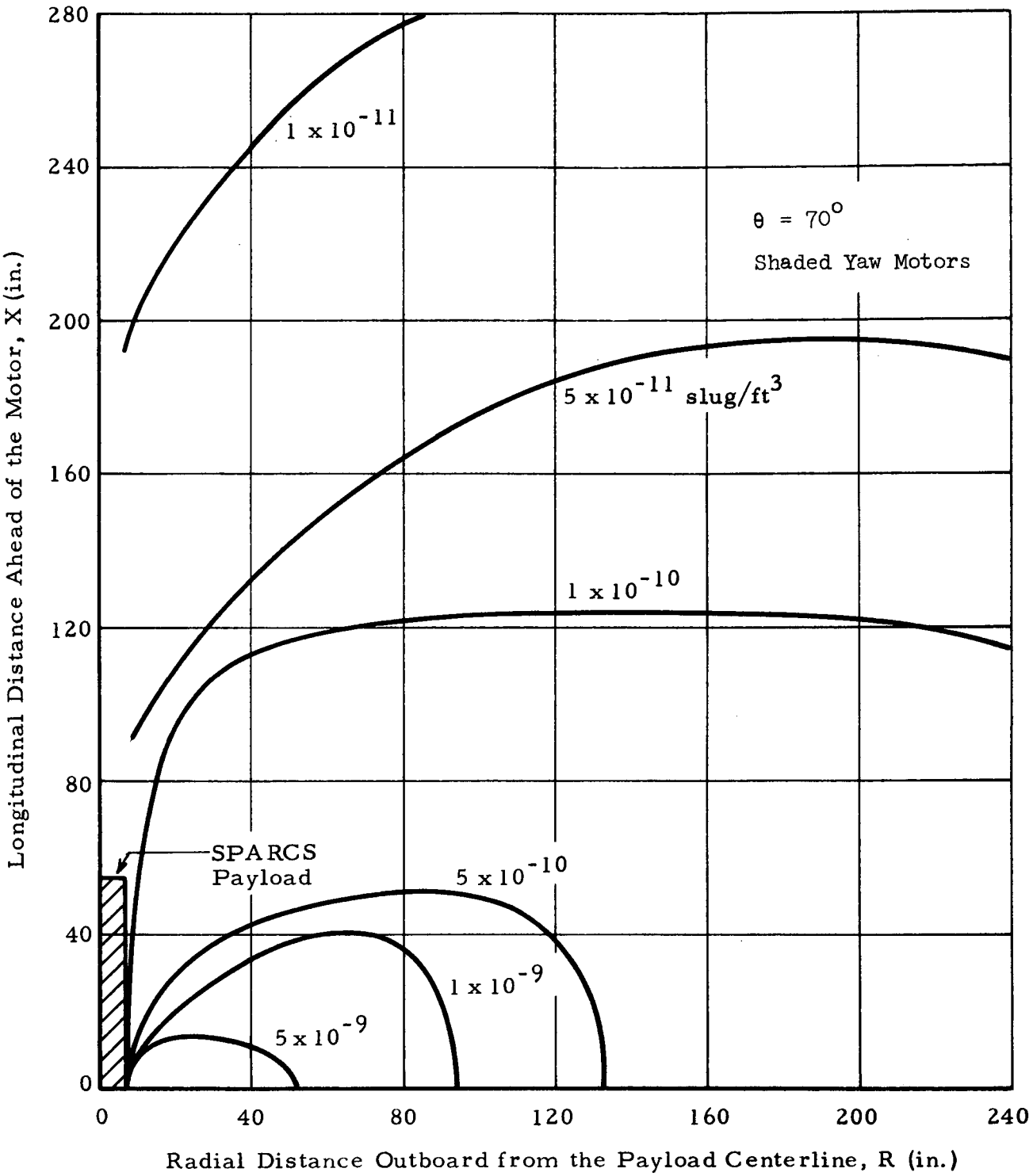

Fig. 17 SPARCS Reaction Control System Plume Density Contours as a Function of Axial and Radial Distance from the Surface of the Vehicle (Shaded Yaw Motors, θ = 70 deg; P_c = 25.0 psia; T_c = 525°R)

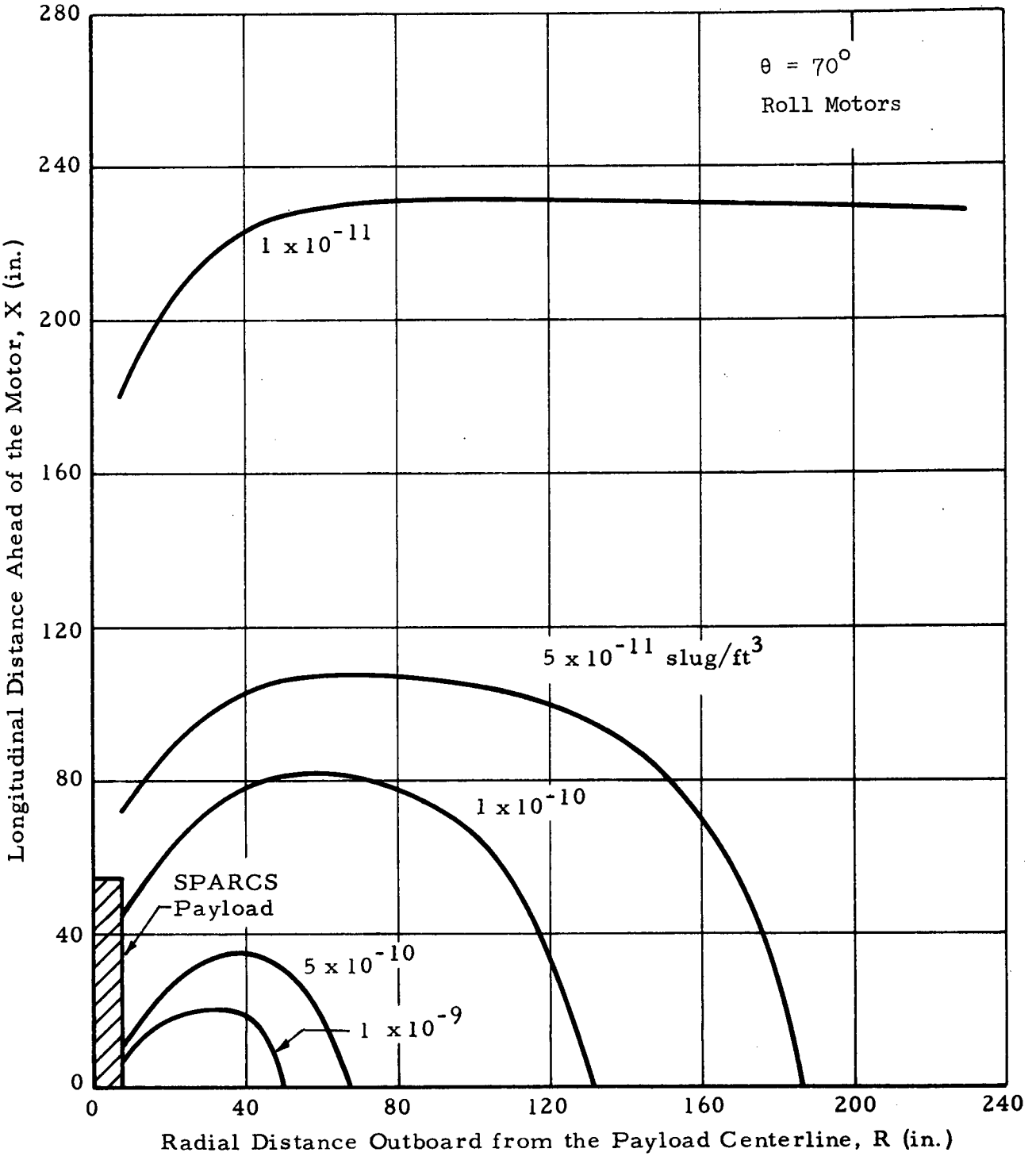

Fig. 18 SPARCS Reaction Control System Plume Density Contours as a Function of Axial and Radial Distance from the Surface of the Vehicle (Roll Motors, θ = 70 deg; P_c = 25.0 psia; T_c = 525°R)

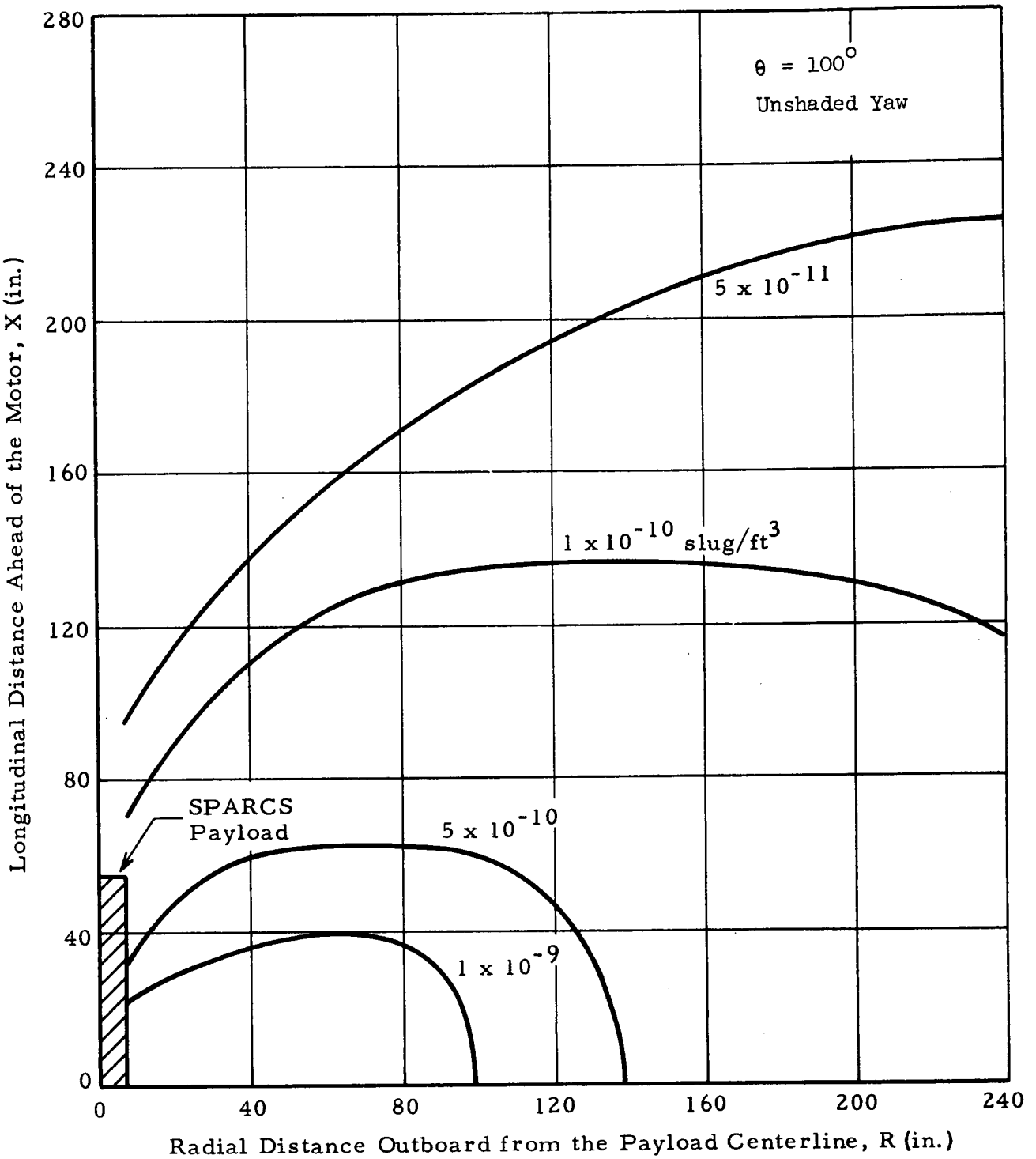

Fig. 19 SPARCS Reaction Control System Plume Density Contours as a Function of Axial and Radial Distance from the Surface of the Vehicle (Unshaded Yaw, θ = 100 deg; P_c = 25.0 psia; T_c = 525°R)

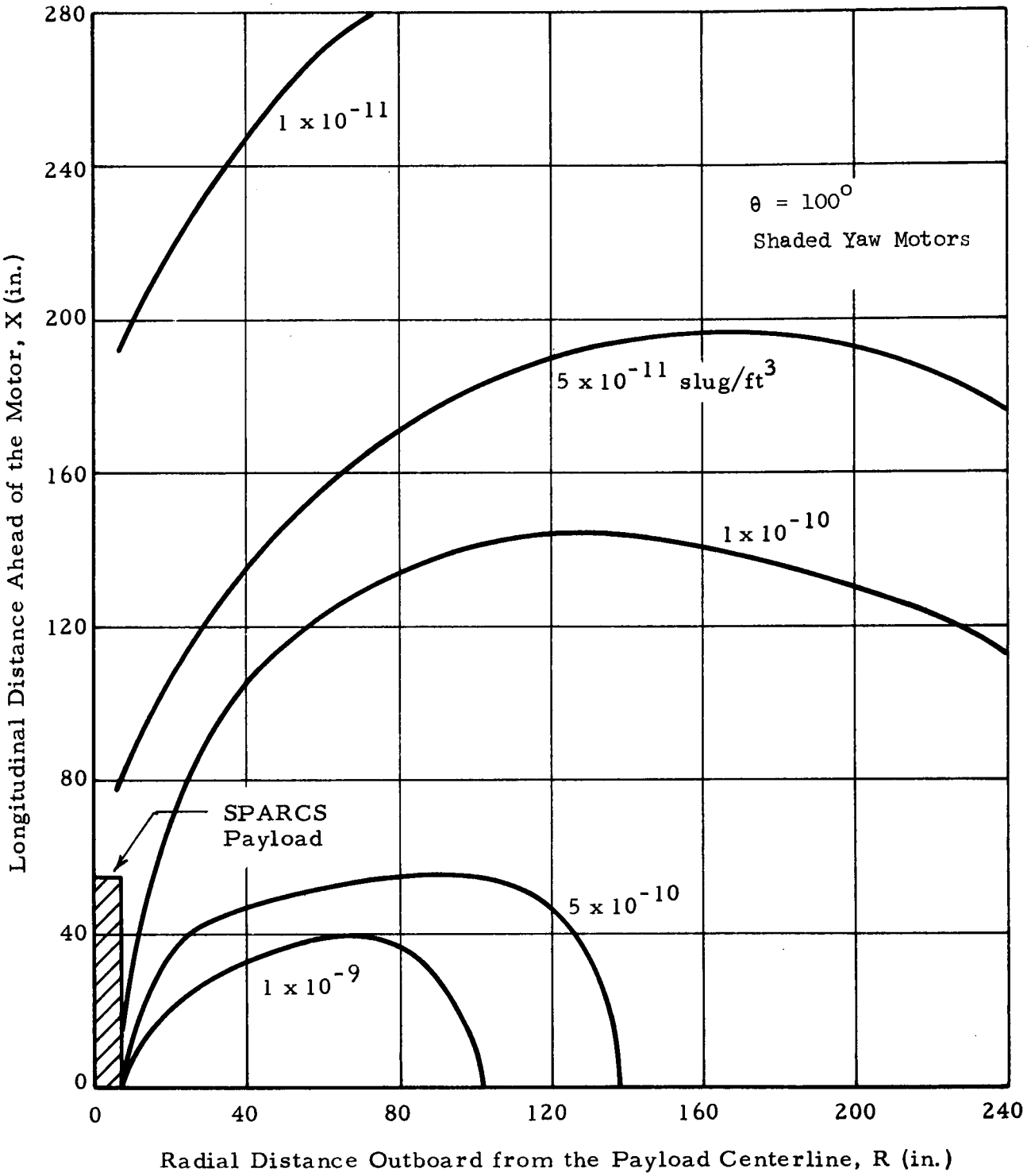

Fig. 20 SPARCS Reaction Control System Plume Density Contours as a Function of Axial and Radial Distance from the Surface of the Vehicle (Shaded Yaw Motors, θ = 100 deg; P_c = 25.0 psia; T_c = 525°R)

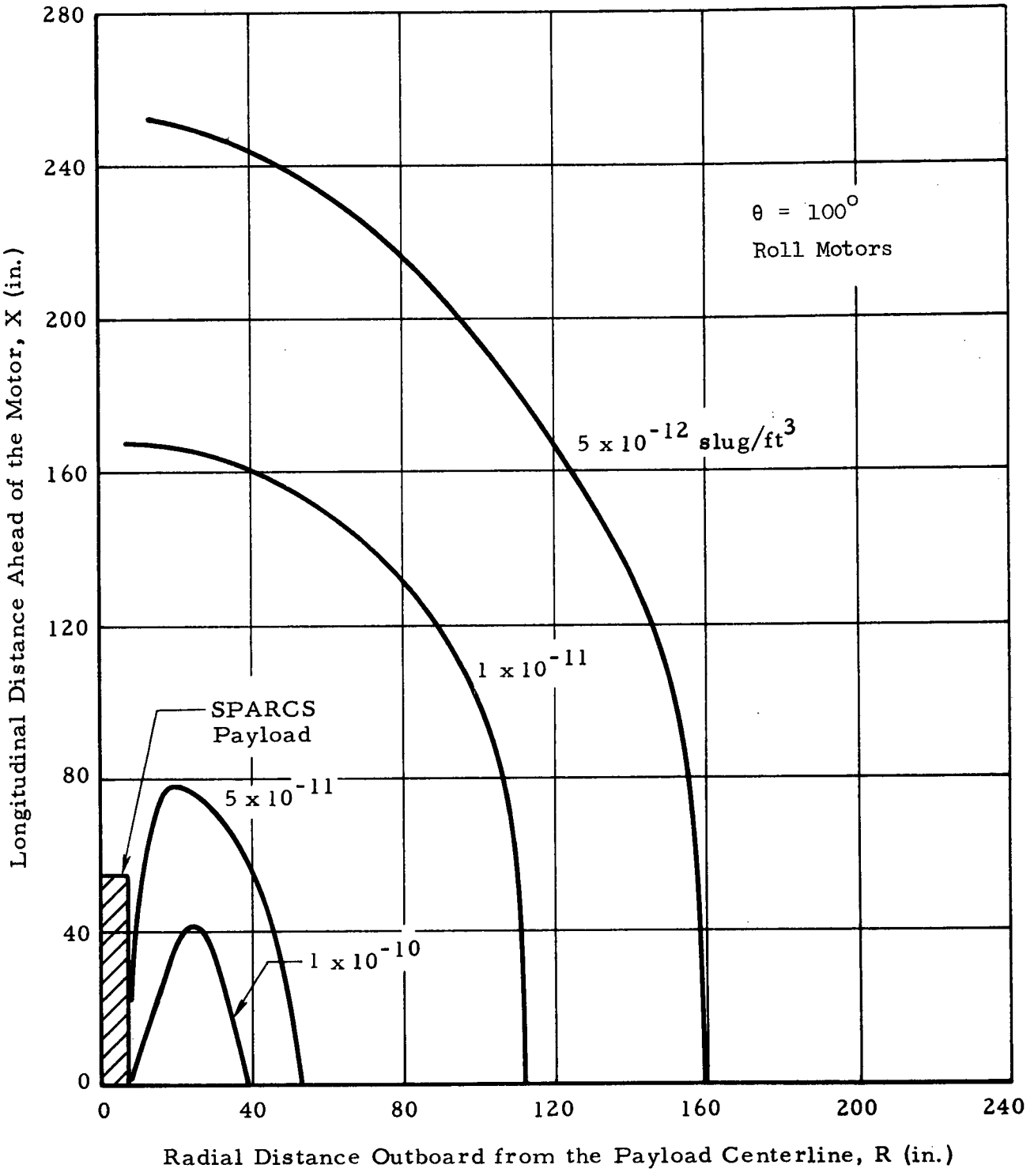

Fig. 21 SPARCS Reaction Control System Plume Density Contours as a Function of Axial and Radial Distance from the Surface of the Vehicle (Roll Motors, θ = 100 deg; P_c = 25.0 psia; T_c = 525°R)

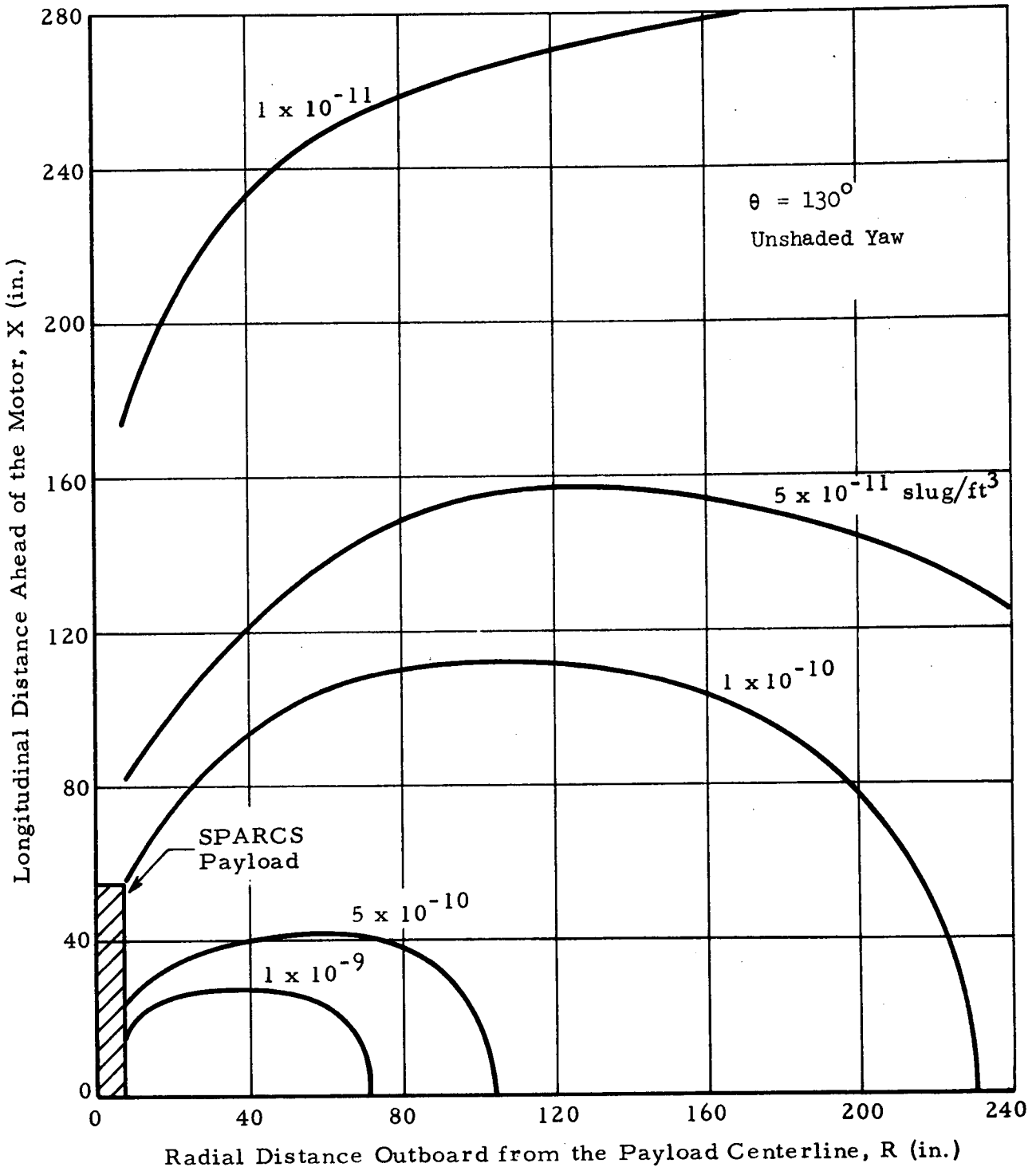

Fig. 22 SPARCS Reaction Control System Plume Density Contours as a Function of Axial and Radial Distance from the Surface of the Vehicle (Unshaded Yaw, θ =130 deg; P_c = 25.0 psia; T_c = 525°R)

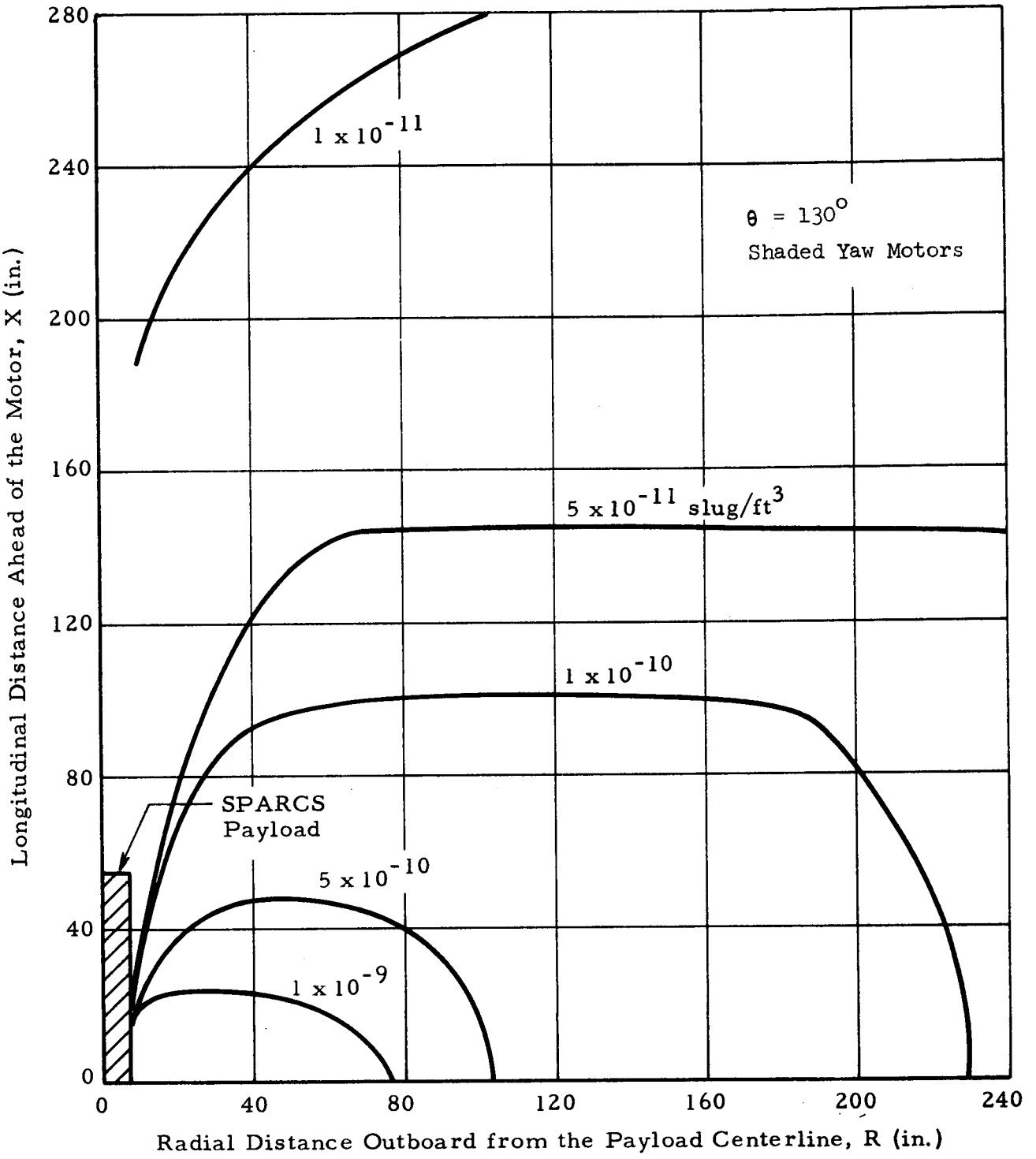

Fig. 23 SPARCS Reaction Control System Plume Density Contours as a Function of Axial and Radial Distance from the Surface of the Vehicle (Shaded Yaw Motors, θ = 130 deg; P_c = 25.0 psia; T_c = 525°R)

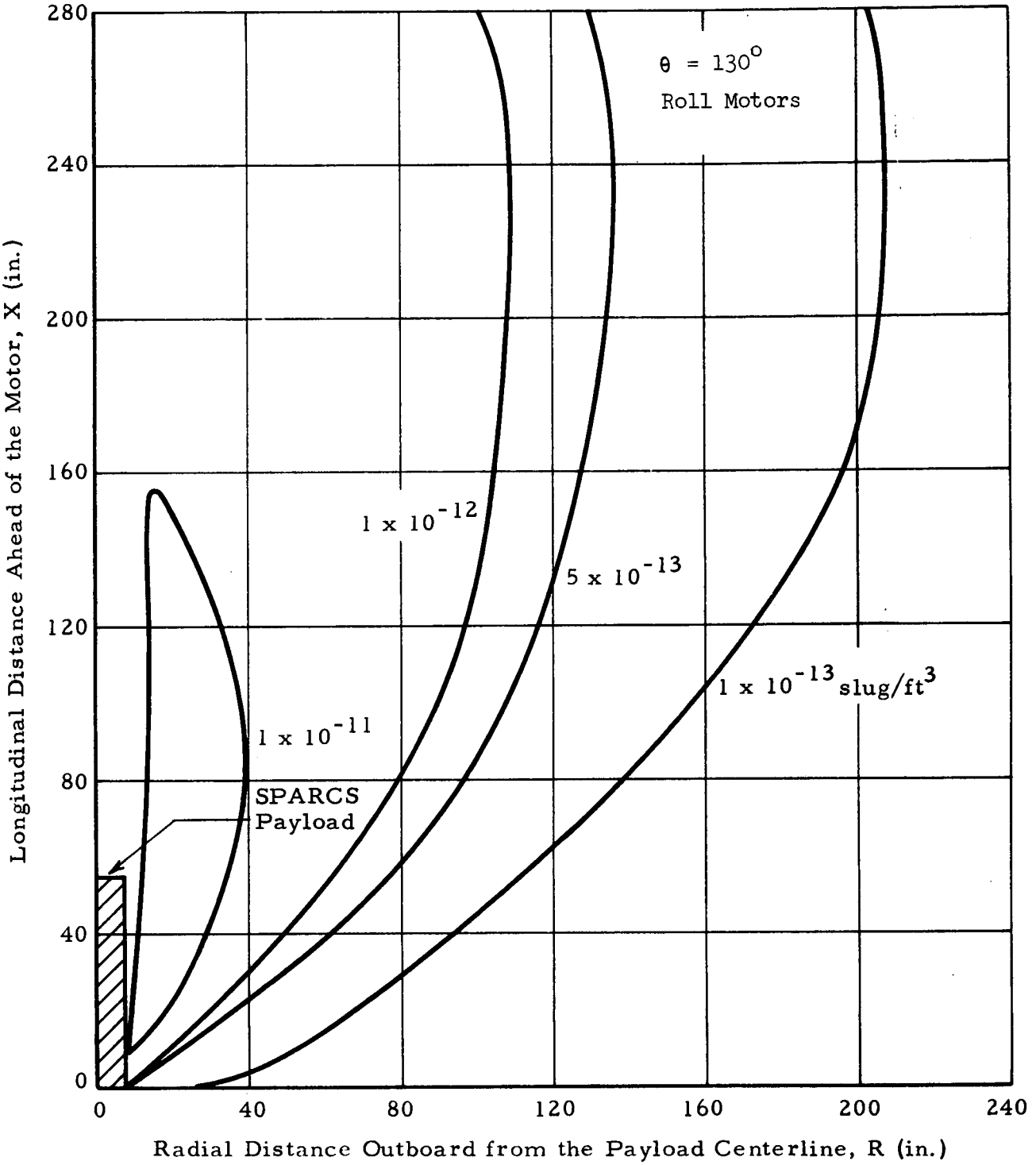

Fig. 24 SPARCS Reaction Control System Plume Density Contours as a Function of Axial and Radial Distance from the Surface of the Vehicle (Roll Motors, θ = 130 deg; P_c = 25.0 psia; T_c = 525°R)

system chamber pressure, working fluid molecular weight, nozzle size, thrust transients encountered during buildup or decay, throat radius of curvature variation and nozzle divergence angle variation will be described. This discussion is limited to non-condensing, non-reacting flows.

o Chamber Pressure Variation

When a rocket motor is fired in deep space the resulting exhaust plume is referred to as an underexpanded plume. When the flow comes out of the nozzle, it tries to expand sufficiently to match the ambient pressure which is essentially zero in deep space. As this expansion occurs the Mach number of the flow increases and the plume boundary grows larger. As shown in ref. 7, the relationship between the angle the plume boundary makes with the nozzle axis and the Mach number is:

$$\nu = \sqrt{\frac{\gamma+1}{\gamma-1}}\ \tan^{-1}\ \sqrt{\frac{\gamma-1}{\gamma+1}(M^2-1)}\ -\ \tan^{-1}\sqrt{M^2-1}$$

where ν is the plume expansion angle, M is the Mach number of the flow at the plume boundary and γ is the ratio of specific heats of the propellant. (See ref. 8 for γ data). As the Mach number approaches infinity the preceding equation becomes:

$$\nu_{max} = \left(\sqrt{\frac{\gamma+1}{\gamma-1}} - 1\right) \times 90^{o}$$

From this one can see that a finite maximum plume expansion angle will occur and it is dependent only on the ratio of specific heats of the flow. When the plume satisfies this condition, the effect of changing the RCS system chamber pressure will be to vary the propellant massflow rate and the RCS thrust in direct proportion to the pressure change. Thus, if the

chamber pressure is doubled the nozzle thrust and the propellant flowrate will double. The plume density contours will remain in the same form and location as before but the magnitude of the density associated with that contour would also double.

o Molecular Weight Variation

The effect of changing the propellant molecular weight will make itself felt by changing the γ of the exhaust flow. Thus, by going to a lower molecular weight gas or gas mixture with the resulting increased γ the plume boundary and internal contours will be compressed. The amount of compression of the internal contours requires a complex calculation that would have to be performed for each case of interest. Also increasing the γ will increase the propellant mass flow rate and the thrust of the RCS system as described by the following equations.

$$w = \frac{P_o A_t}{\sqrt{T_o}} \sqrt{\frac{\gamma}{R_u/(MW)} \left(\frac{2}{(\gamma+1)}\right)^{\frac{\gamma+1}{\gamma-1}}}$$

and for a perfect gas:

$$F = P_2 A_2 (1 + \gamma M_2^2) - P_1 A_1 (1 + \gamma M_1^2)$$

where

P_o = chamber pressure

A_t = nozzle throat area

T_o = chamber temperature

R_u = universal gas constant

F = RCS system thrust

$( )_1$ = nozzle throat conditions

$( )_2$ = nozzle exit conditions

o Nozzle Size Variation

Varying the size of an axisymmetric nozzle while maintaining the same contour variation will change the system mass flow and thrust by $(\frac{r_{\text{throat new}}}{r_{\text{throat old}}})^2$ where r is the nozzle throat radius. The shape of the plume contours will remain the same, however, the location of the contours will be adjusted according to the above ratio to the first power.

o Thrust Buildup or Thrust Decay

During the transients corresponding to thrust buildup or decay the following phenomena will occur. Once supersonic flow is achieved, the plume density contours will establish themselves at the same location they would have at full thrust, however, the density levels would be decreased corresponding to the percent of full thrust propellant mass flow at the time being considered. Pump fed liquid engines can experience an "overshoot" in propellant flow rate and thrust during the startup transient, but the pressure fed SPARCS system will not encounter this.

o Throat Radius of Curvature and Nozzle Divergence Angle Variation

Throat radius variation and nozzle divergence angle variation can make itself felt in two ways. One, if the radius of curvature is large compared to the throat radius and the nozzle divergence angle is small the nozzle boundary layer can build up sufficiently to effectively change the nozzle contours. The effect would be to concentrate more of the

exhaust mass near the motor centerline and shift the lines of constant properties downstream as the effective M_{exit} is decreased. The thrust level will drop slightly because the internal friction losses are increased.

Next, if the throat radius of curvature is small and the nozzle divergence angle is large, then the flow will try to expand to follow the rapidly enlarging nozzle contour and may separate from the wall. The magnitude of these values is empirically determined and is dependent on the type of propellants being used, the level of P_c and T_c, and the actual size of the nozzle. When separation occurs, the flow is governed by a pseudo nozzle contour which it follows and becomes analytically unpredictable. Thus, using too big or too small throat radius of curvature is to be avoided.

o Exhaust Plume Shielding

If it is determined that the exhaust plume interference effects on the SPARCS solar sensors seriously degrades the system's performance, the plume can be totally shielded from the area ahead of the payload. The dimension of the shields required for the yaw and roll motors are shown in Figure 25. The shields can be within a fraction of an inch of the nozzles. Their dimensions are not critical.

Column densities of CF_4 plumes in the region ahead of the payload were obtained by calculating the integral of the density along lines parallel to the vehicle axis at a number of points. The results are given in Table 2, in units of slugs/ft^2 (10^{-12} slugs/ft^2 = 1.075 x 10^{11} molecules/cm^2 for CF_4). Figure 26 gives approximate contours of equal

D

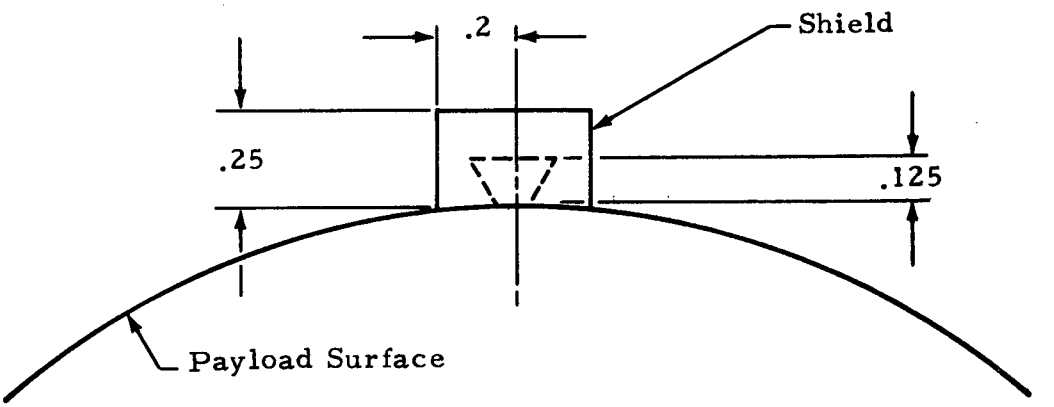

Yaw Motor Shield

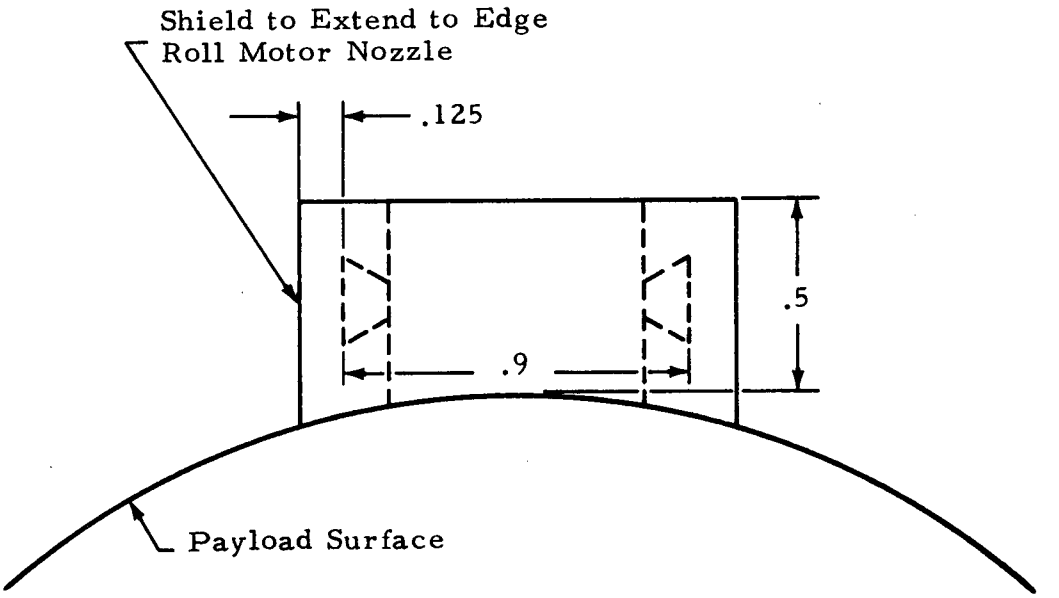

Roll Motor Shield

Figure 25 Suggested Shield Sizes to Prevent Plumes from Reaching Front of Payload.

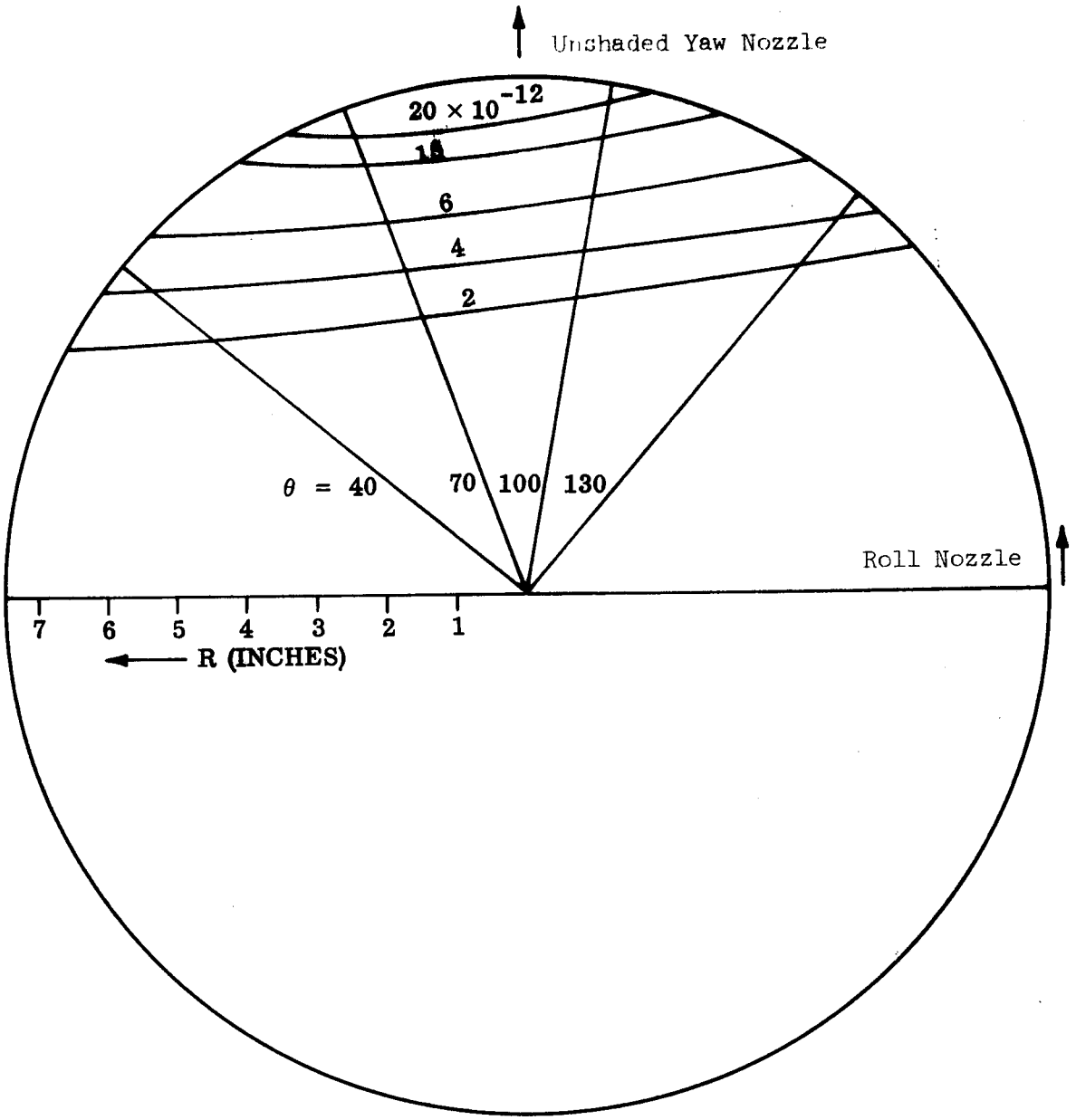

Figure 26 Contours of integrated column density ahead of payload for one roll motor and one unshaded yaw motor (Densities in slugs/ft^2).

column density for the sum of one roll motor and one unshaded yaw motor firing simultaneously, where the orientation of the motor plumes is shown by the arrows. The shaded yaw motors do not contribute to these integrals.

Table 2

Column Densities Ahead of Payload

Angle	Type of Motor	R inches	$\int$ pdx Slugs/ft^2
40°	Roll Motor	7.124	4.61×10^{-12}
40°		5.625	2.35×10^{-12}
70°		7.124	2.56×10^{-11}
70°		5.625	6.98×10^{-12}
100°		7.124	1.29×10^{-11}
100°		5.625	5.92×10^{-12}
130°		7.124	4.31×10^{-12}
130°		5.625	1.96×10^{-12}
70°	Unshaded Yaw	7.124	1.15×10^{-12}
100°	Unshaded Yaw	7.124	5.79×10^{-12}

IV. ABSORPTION AND FLUORESCENCE OF CF_4 PLUMES

The optical effects of the CF_4 plumes from SPARCS can be computed by combining the density data of Section III with the absorption and fluorescence data given in Section II and Appendices A, B and C. Some sample calculations are given here.

Absorption of radiation by CF_4 ahead of the payload is a maximum at 780Å where the absorption coefficient K = 1550 $cm^{-1}atm^{-1}$ (Fig. 27, Appendix A). This corresponds to an absorption cross section $\sigma = 5.76 \times 10^{-17} cm^2$.

The column density, n_c, of CF_4 for P_c = 25 psi ahead of the payload is about 27 x 10^{-12} slugs/ft^2 or 2.7 x 10^{12} molecules/cm^2, (Figure 26) near the edge of the payload where the gas density is highest. It follows that the transmission, $I/I_o = \exp[-n_c\sigma] = 0.99985$. where I_o is the incident light flux at 780Å and I is the flux reaching the top of the payload. This is essentially unity and absorption loss is thus negligible ahead of the payload, for even this extreme case. For the early portion of the flight when de-spin is occurring and the nozzle chamber pressure P_c = 800 psi, scaling up the density by a factor of 32, the light transmission is 0.995, and absorption is still negligible.

Fluorescence of CF_4 plumes when irradiated by sunlight can be computed using the density and fluorescence efficiency data. Consider the plume gases ahead of the payload. The fluorescent signal from this gas is $g.\int \rho d\,x\,/\Delta\lambda$. Here g = 2.6 x 10^{-7} photons/sec. molecule is the fluorescent g factor from Table 4 Appendix B; the density integral is at most 2.7 x 10^{12} molecules/cm^2 over those portions of the near the contours of greatest density in Figure 26; the wavelength interval over which CF_4 fluoresces, $\Delta\lambda$ = 1000Å as found in Figure 8 and the experiment report in Appendix C. Thus the fluorescent signal is 700 photons/sec. cm^2·Å emitted in all directions, or, dividing by 4π, 55.5 photons/sec. cm^2·Å steradian in the wavelength interval between 2100 to 3100Å.

The importance of this fluorescent signal can only be assessed by comparing it with signals from astronomical targets for present or future Freon controlled payloads. The uv spectrum of the planet Mars was

observed reported by Barth et. al. (ref. 3) and a copy of this data is shown in Figure 11. The ordinate is in units of Raylights per angstrom and a typical emission feature produces about 200 R/A or 16×10^6 photons/sec. $cm^2 \cdot A$. A Freon controlled instrument near Mars would thus not be troubled by the CF_4 fluorescent signal computed above. On the other hand if Mars were observed from near the earth's orbit the situation is different. In this case the rocket borne telescope would see the entire planet but at a distance of at least 0.5 AU. The planetary signal at the rocket would be:

$$S = I \cdot a \cdot \Omega$$

Here $I = \frac{16}{4\pi} \times 10^6$ photons/sec. $cm^2 \cdot \text{Å} \cdot$ steradian
the emission of a typical spectral feature

$a \cong 0.75 \times 10^{18}$ cm^2 = area of Martian disc

$\Omega = 1.8 \times 10^{-23}$ steradian = solid angle subtended by telescope with 1000 cm^2 entrance aperture at 0.5 astronomical unit.

Thus $S = 210$ photons/sec $\cdot A$ in a typical band.

The fluorescent signal due to excitation of CF_4 by sunlight is

$$S_F = I_F \cdot b \cdot \Omega$$

Here $I_F = 55.5$ photons/sec $\cdot$ cm^2 $\cdot A \cdot$ steradian emitted by portions of the CF_4 plumes

$b \cong 100$ cm^2 = approximate area of top of payload where density of CF_4 is appreciable (see Figure 26)

$\Omega = 10^{-2}$ steradian = solid angle subtended by 1000 cm^2 telescope 10 feet (304 cm) from the source

The result is $S_F \cong 55$ photons/sec·A. Thus in this case the CF_4 fluorescence is comparable to the planetary signal.

APPENDIX A

Detailed Absorption Coefficient Data

Freon, CF_4

Figure 1 summarizes the absorption coefficient data for freon. In the ten to two hundred Å spectral region, the absorption coefficient data was obtained from Henke et al. (Ref. 9). The ordinate for this graph is in units of cm^{-1} atm^{-1}. Between 600Å and about 1000Å the absorption coefficient includes both continuum and discrete bands whose structure is indicated crudely in Figure 1 and shown in more detail in Figure 27 from data of Cook and Ching (Ref. 1). Between 950Å and about six microns the gas is essentially transparent. Beyond seven microns there are a number of infrared absorption bands. Figure 1 shows the location of these bands. Figure 28 displays the absorption structure of the 7.9, and 16 micron bands. These were obtained from Edgell and Moynihan (Ref. 10).

No absorption coefficient data is available between 200 and 600Å. Figure 1 shows a possible curve for this region, which may be in error by more than a factor of two.

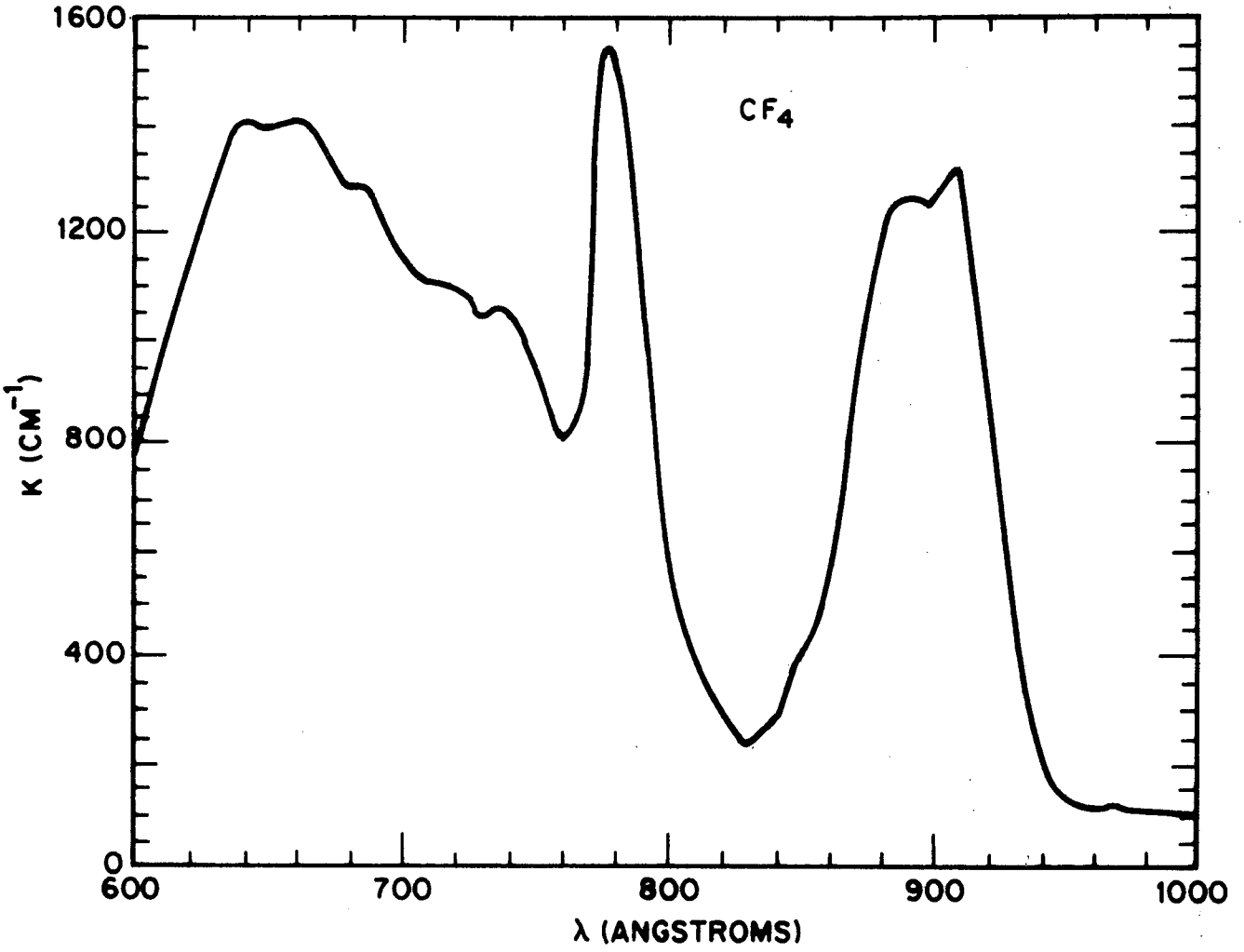

Figure 27 UV Absorption of CF_4

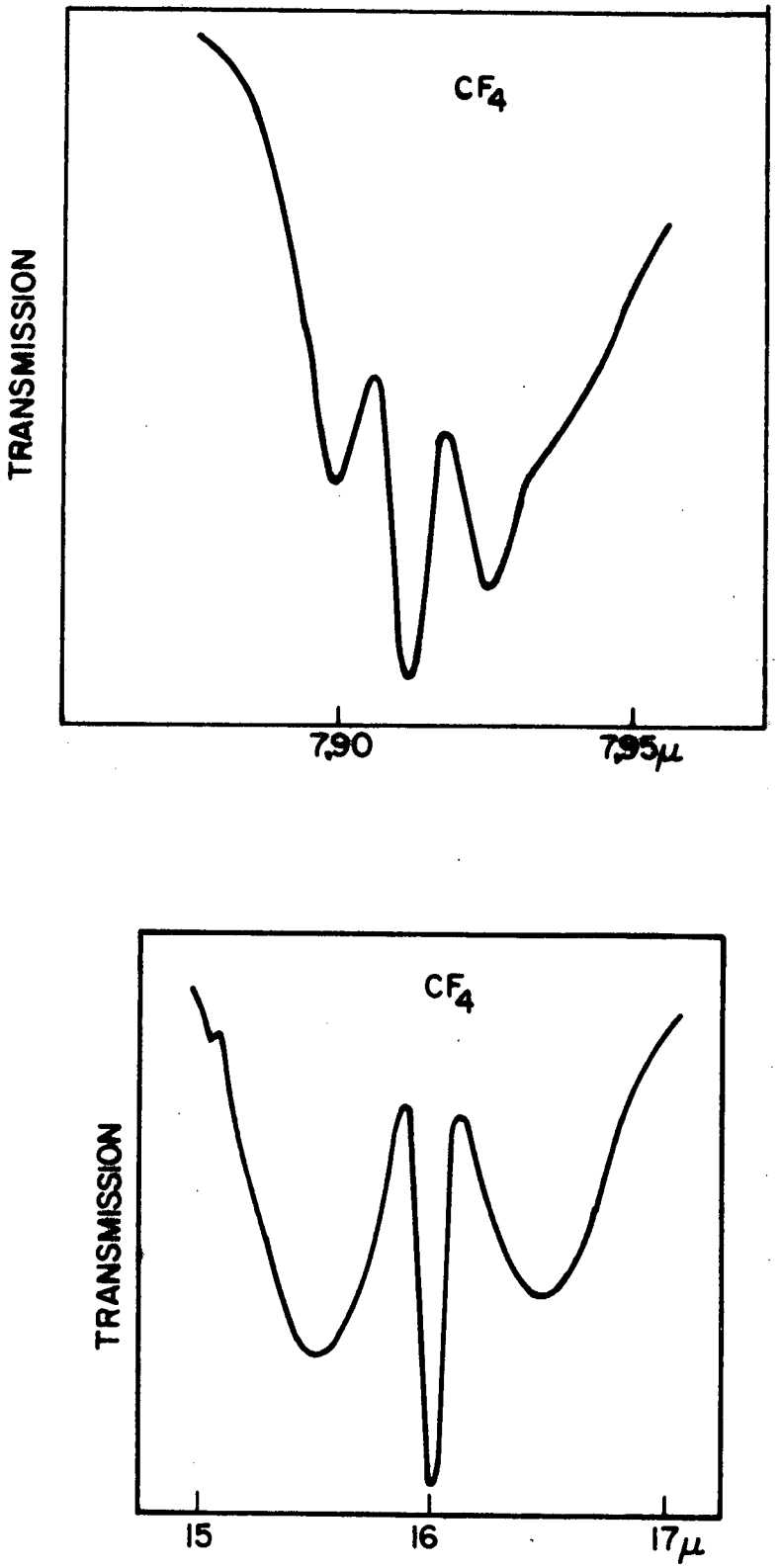

Figure 28 Infrared absorption of CF_4 bands at 7.9 and 16 microns.

Hydrazine, N_2H_4

The absorption of the hydrazine molecule is summarized in Figure 2. Data for the 10Å to 200Å interval were obtained from Henke (Ref. 9). From 200 to 1200Å no data are available and a tentative absorption coefficient curve is sketched in. Between 1200 and 2000Å absorption coefficient measurements were made by Schurgers and Welge (Ref. 11). Their data are shown in the inset in Figure 2. There is additional UV absorption of hydrazine with intensity maxima at 2326, 2320, 2276, 2215, 2225Å with continuous absorption beginning at wavelengths shorter than 2200Å. This was reported by Imanishi (Ref. 12). Infrared absorption of hydrazine has been studied by Giguere and Liu (Ref. 13). Their results are shown in Figure 29, where prominent bands are observed at 3 microns, 6.2 microns and a broad band centered at 10.4 microns. Absorption coefficients are provided at the peaks of the strong bands. At 3 microns $K = 0.27\ cm^{-1}$, at 6.2 microns $K = 0.3\ cm^{-1}$, and at the peak of the 10.4 micron band $K = 1.15\ cm^{-1}$. These values of the peak absorption coefficient apply only to the pressure and temperature at which the data were taken and do not represent the values attainable under the conditions of lower temperature and pressure.

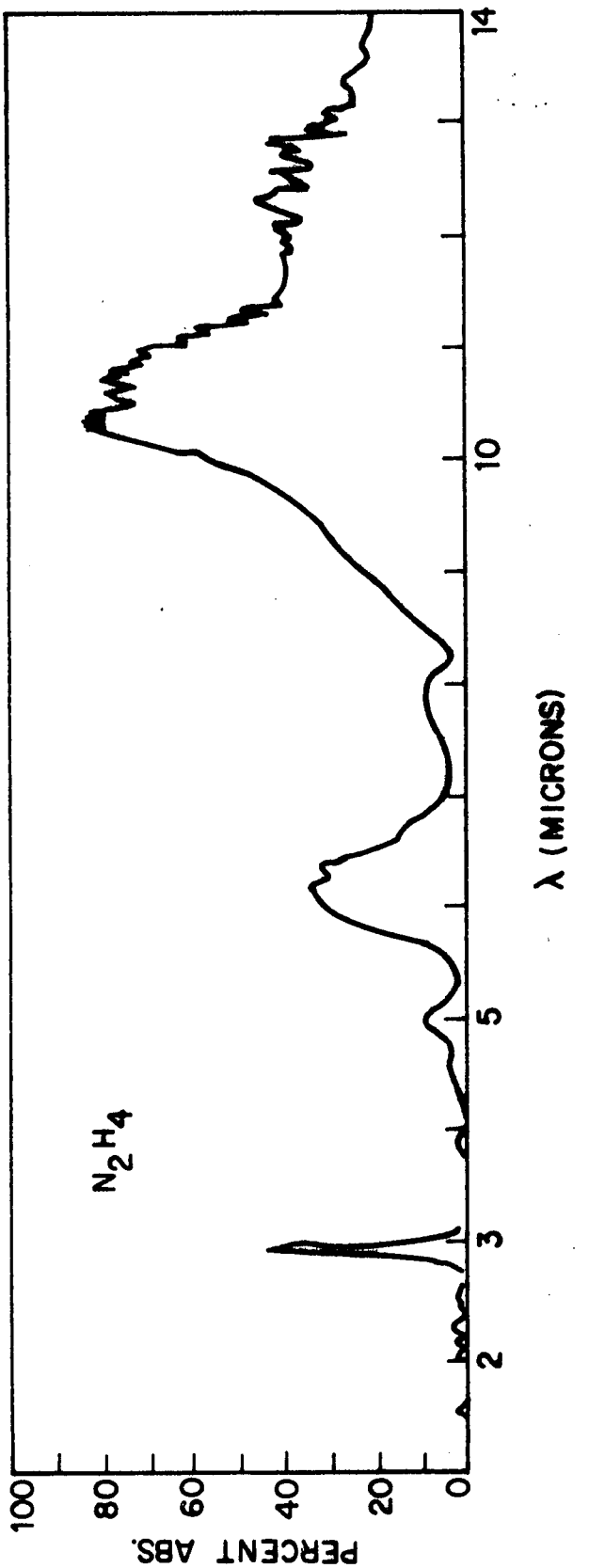

Figure 29 Infrared Bands of Hydrazine

Nitrogen, N_2

The absorption spectrum of nitrogen has been studied by a number of investigators. In the x-ray region, Figure 3 shows the characteristic K-edge of nitrogen of 30Å. At longer wavelengths the absorption coefficient rises to a peak near 800Å. Figure 3 does not attempt to show the detail of the highly structured absorption bands of N_2 in the vacuum UV. This is shown in Figures 30, 31 and 32 from Cook and Ching, (Ref. 14). At wavelengths above 980Å the absorption essentially vanishes except for the weak Lyman-Birge-Hopfield bands in the 1200 to 1900Å region and the Vegard-Kaplan bands at slightly longer UV wavelengths. In the visible and infrared there is no absorption.

Additional information of the UV absorption of nitrogen is provided by Huffman, Tanaka and Larrabee (Ref. 15) for the 580 to 1000Å region. Absorption of the nitrogen Lyman-Birge-Hopfield bands was measured by Ching, Cook, and Becker (Ref. 16). Their results for integrated intensities are given below. An estimate of peak absorption coefficient at strong lines in each of the bands was made by assuming each band consists of 20 lines with Doppler contour. Dividing the integrated band intensity by 20 Doppler widths yields the peak absorption coefficients given in the table and indicated in Figure 3.

Lyman-Birge-Hopfield System

v'v"	Band Strength cm^{-2} atm^{-1}	Wavelength Angstroms	20 $\Delta\nu_D$	Peak Absorption Coeff. (cm^{-1} atm^{-1})
0-0	32	1450.12	2.64	12
1-0	71	1415.92	2.71	26
2-0	98	1383.82	2.77	35
3-0	112	1353.65	2.83	40
4-0	120	1325.26	2.89	42
5-0	93	1298.5	2.95	32
6-0	83	1273.24	3.01	28
7-0	48	1249.3	3.07	16
8-0	36	1226.6	3.12	12
9-0	22	1205.3	3.18	7

v' and v" are vibrational quantum numbers of upper and lower state.

$\Delta\nu_D$ = Doppler width of typical line.

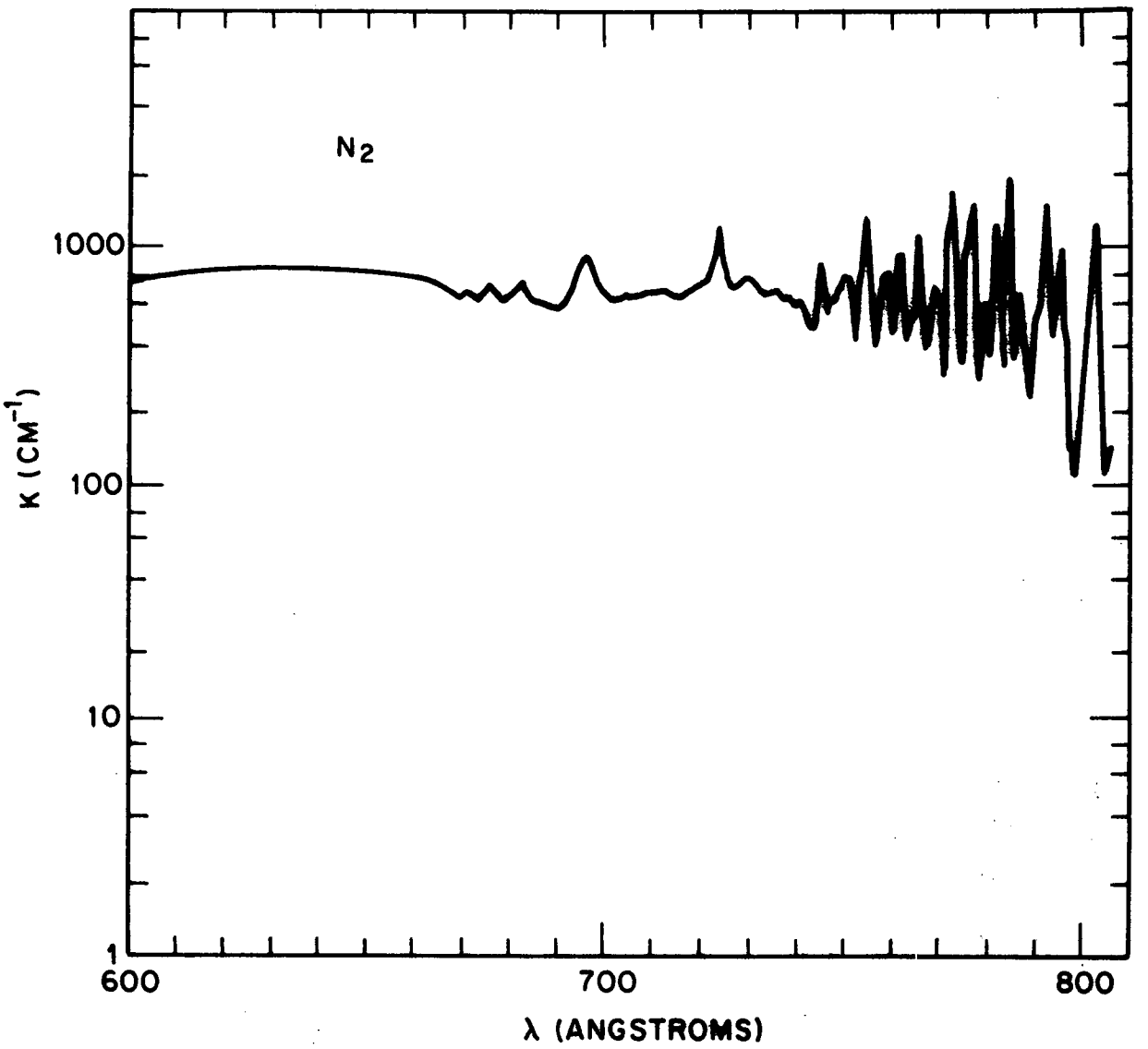

Figure 30 UV absorption coefficient of nitrogen.

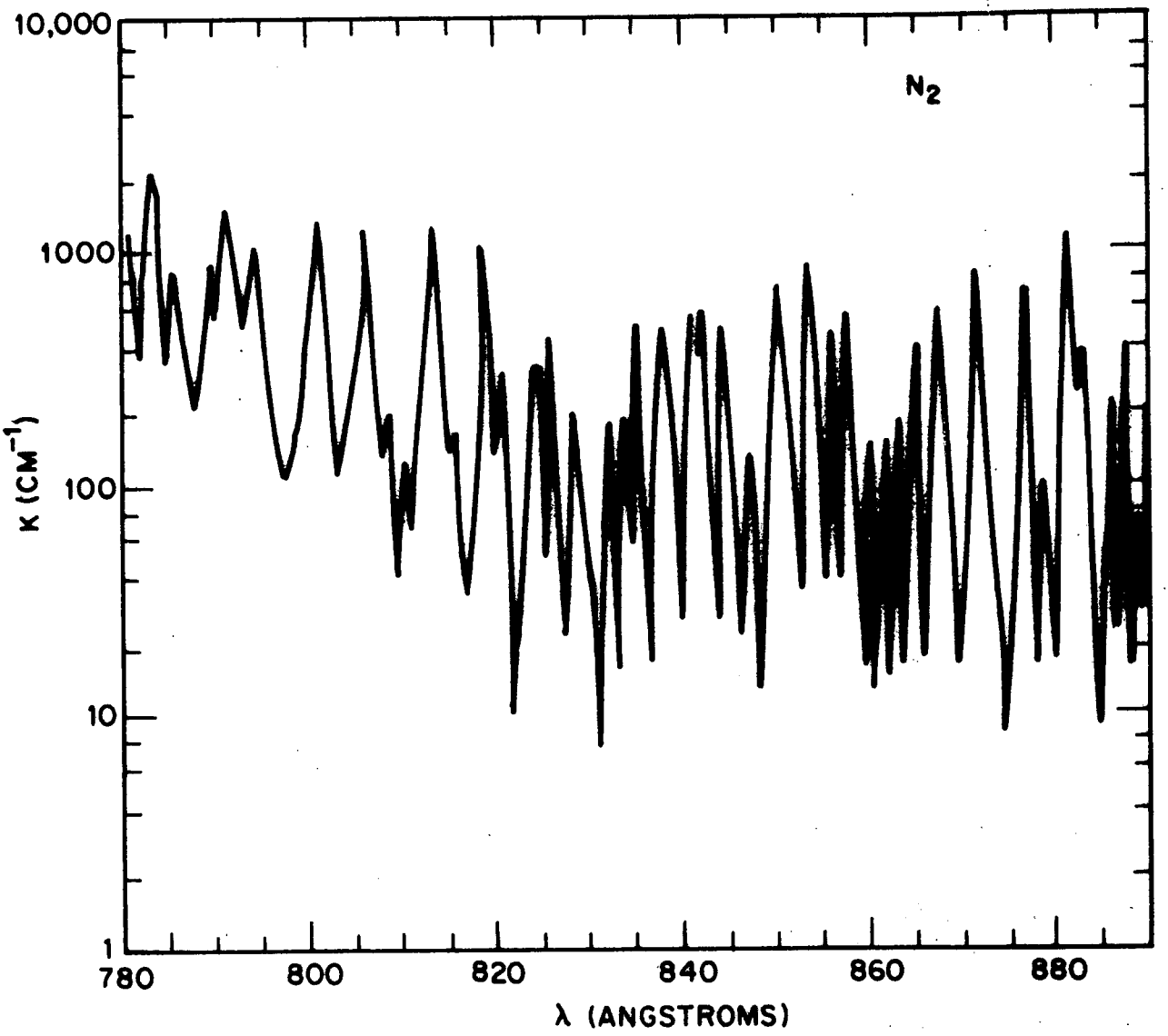

Figure 31 UV absorption coefficient of nitrogen.

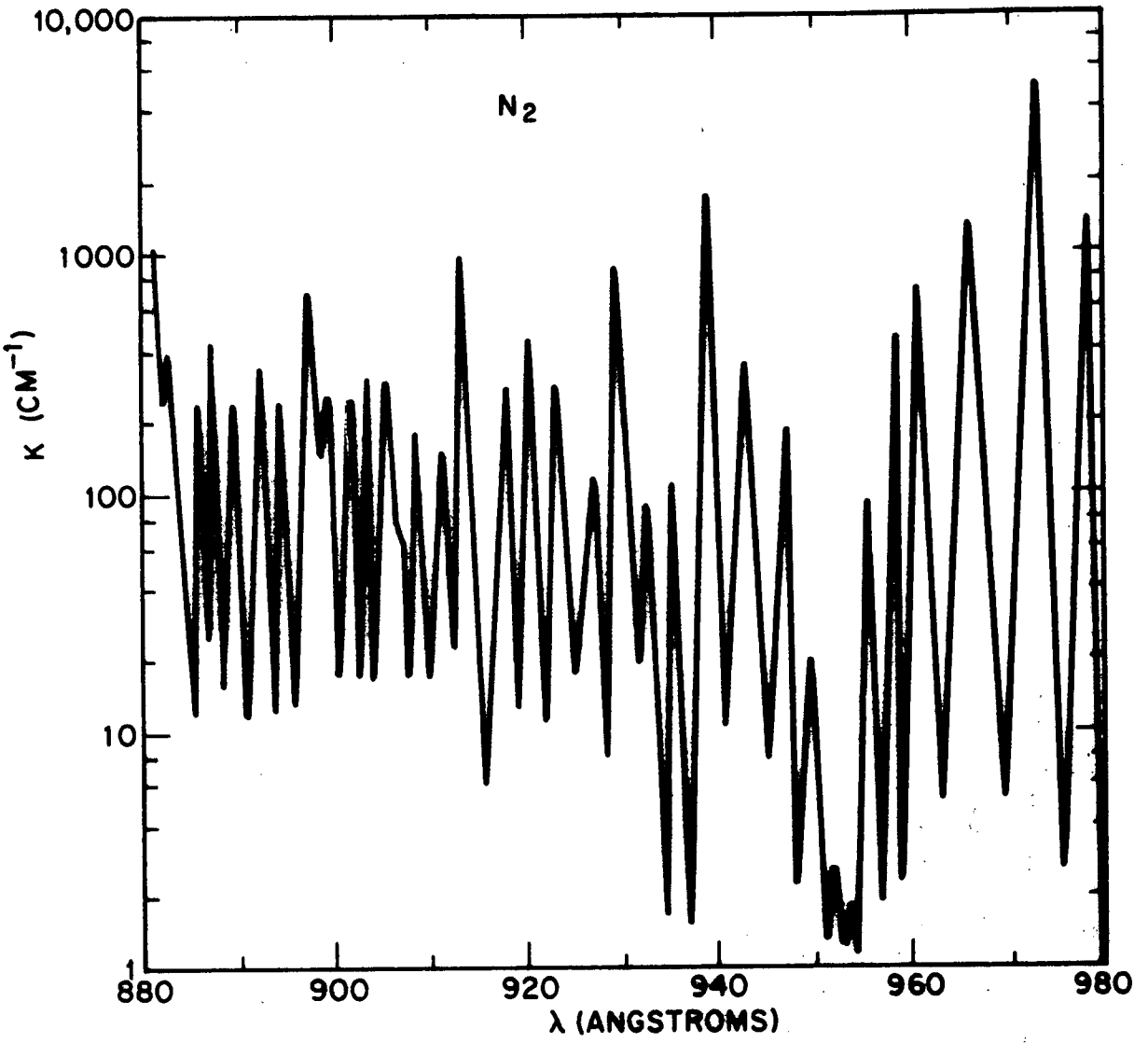

Figure 32 UV absorption coefficient of nitrogen.

Ammonia, NH_3

The absorption of ammonia is given in Figure 4. X-ray data comes from Henke (Ref. 9). In the vacuum UV region data was obtained from Cook and Ching (Ref. 14) and Watanabe (Ref. 17). The x-ray data shows the characteristic K-edge of nitrogen at 30Å. At longer wavelengths it rises to a peak at about 800Å. Detail in this spectral region is provided by Figure 33, adapted from Nicolet (Ref. 18). The UV absorption bands of ammonia in the 1100Å to 2200Å region are given in Figure 34, (Watanabe Ref. 17).

There are three important infrared bands of ammonia; at 3, 6, and 10 microns. Relative strength of these bands is indicated in Figure 4 and some of the detailed structure is shown in Figure 35 from Ref. 22. There is apparently no absorption by ammonia between 2200Å and 3 microns.

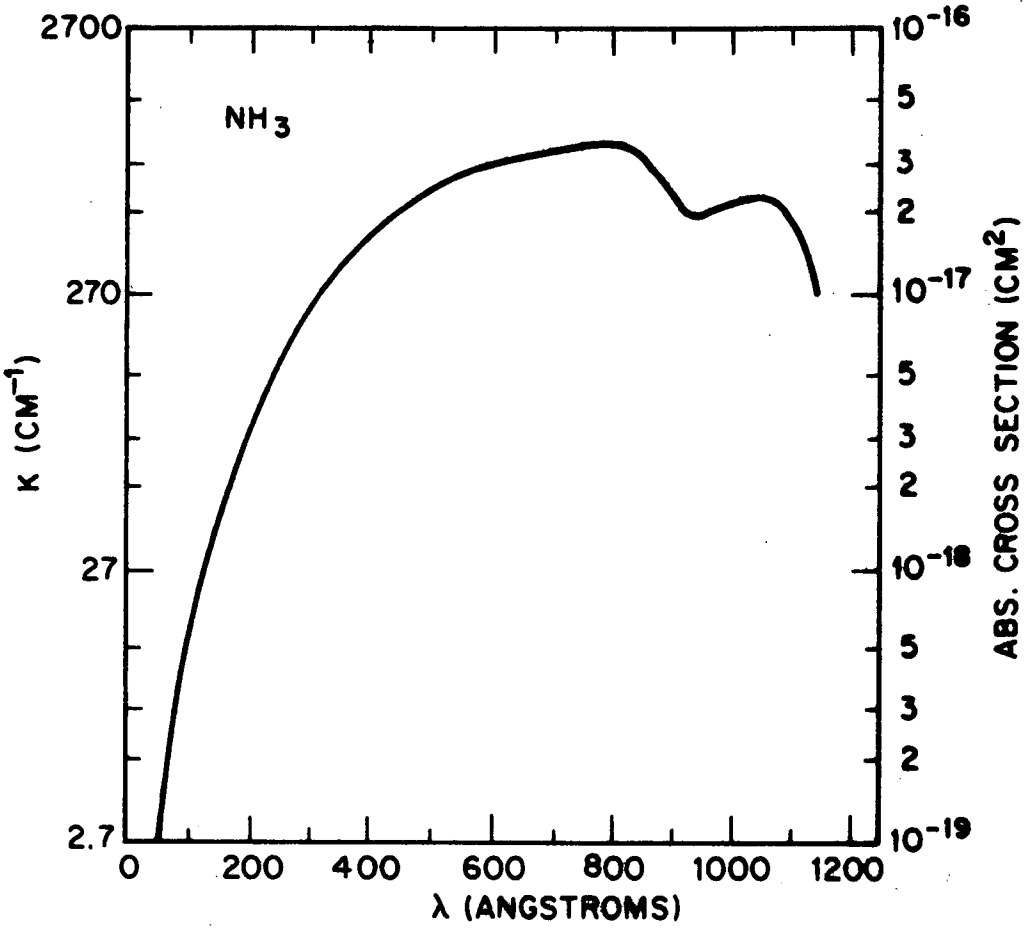

Figure 33 UV absorption coefficient of ammonia.

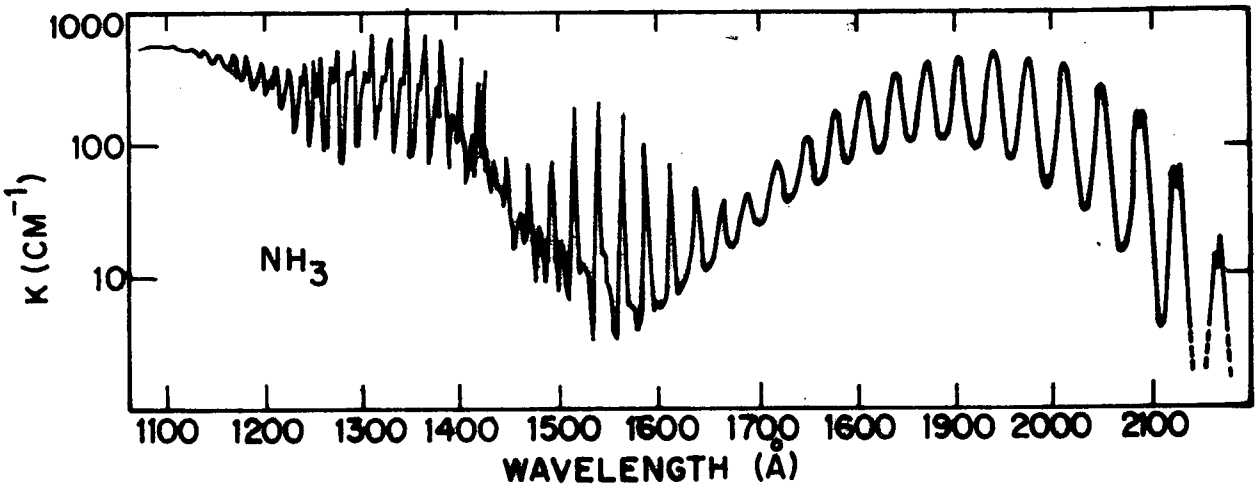

Figure 34 UV Band Structure of Ammonia

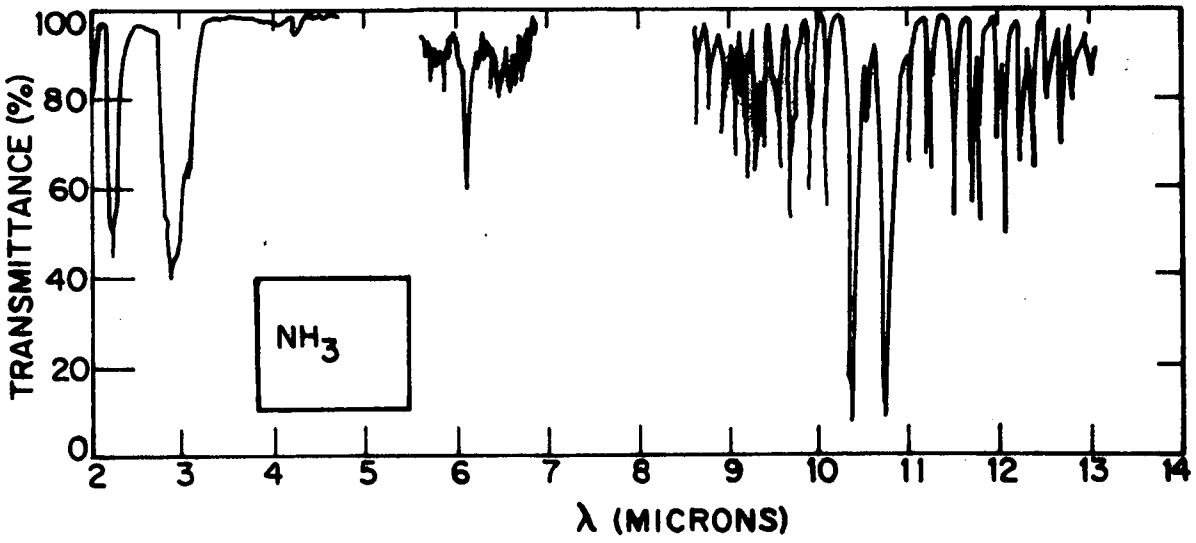

Figure 35 Infrared Bands of Ammonia

Carbon Dioxide, CO_2

The absorption spectrum of CO_2 is represented in Figure 5. Below 100Å it is dominated by continuous absorption interrupted by the K-edges of the carbon and oxygen atoms at 43.7Å and 23.3Å, respectively. Between 200 and 400Å no data is available and a tentative sketch is provided. In the vacuum UV Figure 5 only crudely indicates the complexity of the continuous and band spectra. The continuous absorption from 400 to 600Å observed by Sun and Weissler (Ref. 19) is plotted in Figure 36, along with the beginning of the band spectrum near 700Å from Cook and Ching (Ref. 14). Figure 37 continues the data of Cook and Ching to 1000Å. In this figure the solid line represents the total absorption and the dashed curves are the proposed heights of the continuua underlying the band spectrum between 700 and 850Å. Figures 38 and 39 from Inn, Watanabe and Zelikoff (Ref. 20) show details of the spectrum between 1050Å and 1800Å. The weak absorption from 1800 to 2200Å is shown in Figure 40 from Ogawa (Ref. 21). From 2200Å to the near infrared carbon dioxide is transparent.

The prominent infrared absorption bands are illustrated in Figure 41 from Pierson, Fletcher and Gantz (Ref. 22). The shorter wavelength bands are shown as they appear at a pressure of 900 torr (mm Hg), while the broad 15 micron band is plotted as it appears at 70 torr. Figure 42 gives a detailed transmission curve for the CO_2 4.26 micron band which appears as a single line in the low resolution data of Figure 41. Figure 42 is from Barrow (Ref. 23).

The integrated intensities of the absorption bands of carbon dioxide in the infrared are derived from Penner (Ref. 24) and listed below.

Wavelength Microns	Integrated Intensity cm^{-2} atm^{-1}
1.96	0.426
2.0	1.01
2.06	0.272
2.69	42.3
2.77	28.5
4.26	2706.
15.0	171.
4.81	0.1
5.17	0.08

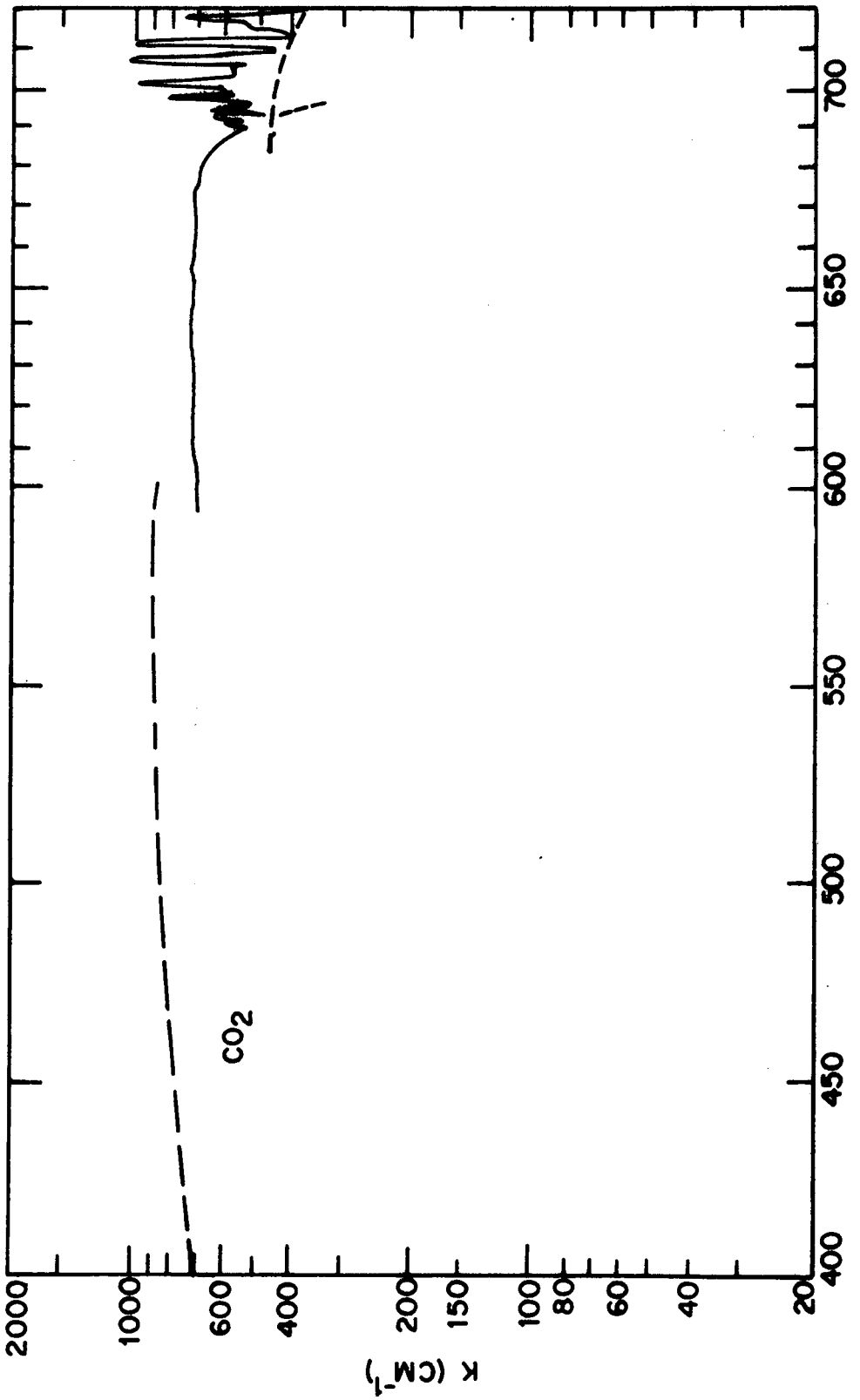

Figure 36 UV Absorption Coeffient of CO_2

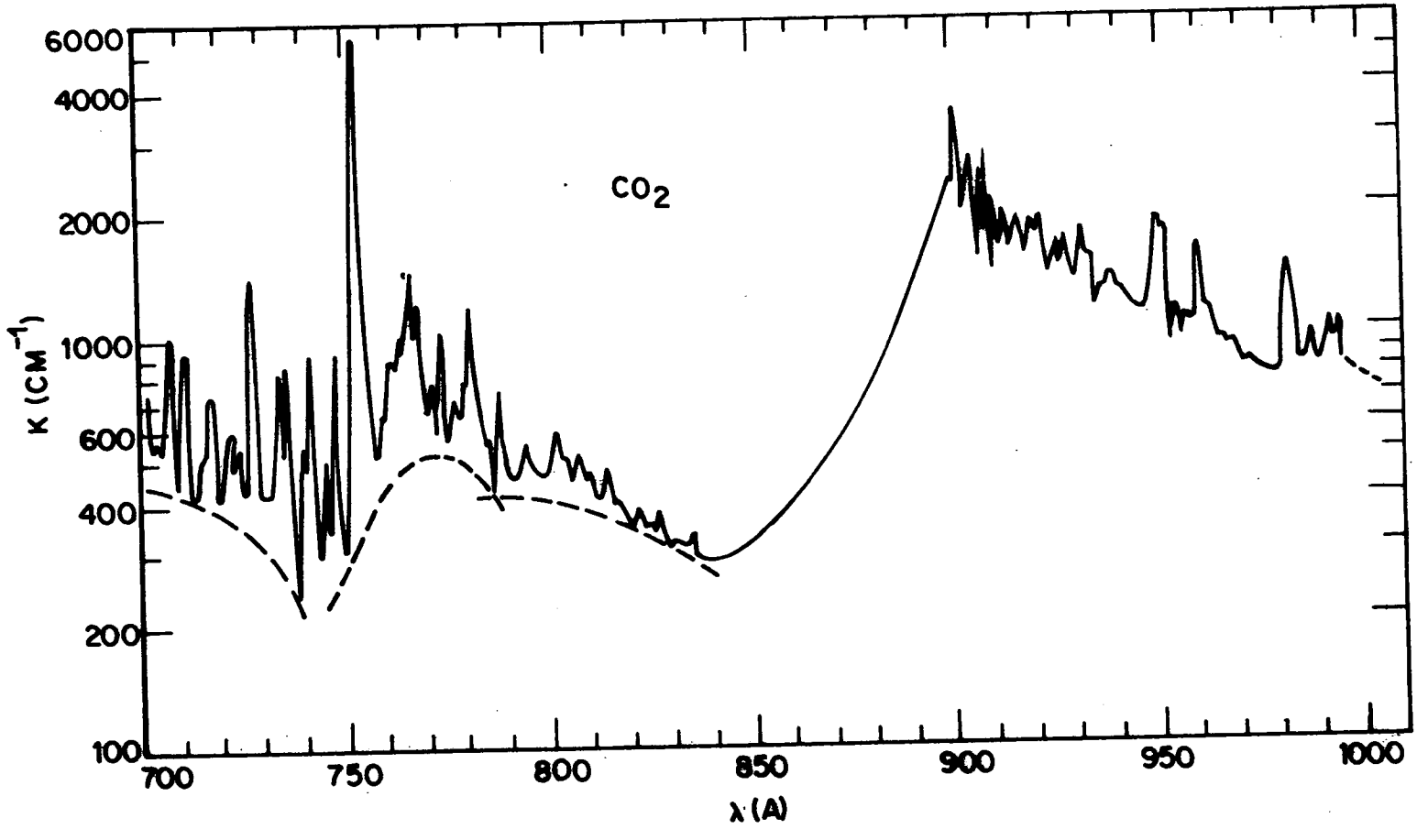

Figure 37 UV absorption coefficient of CO_2

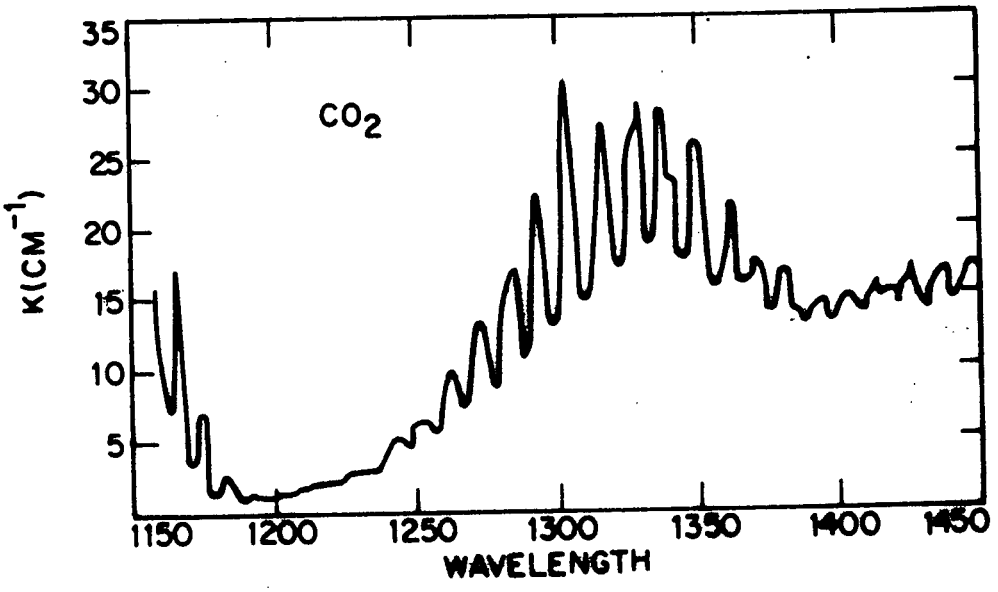

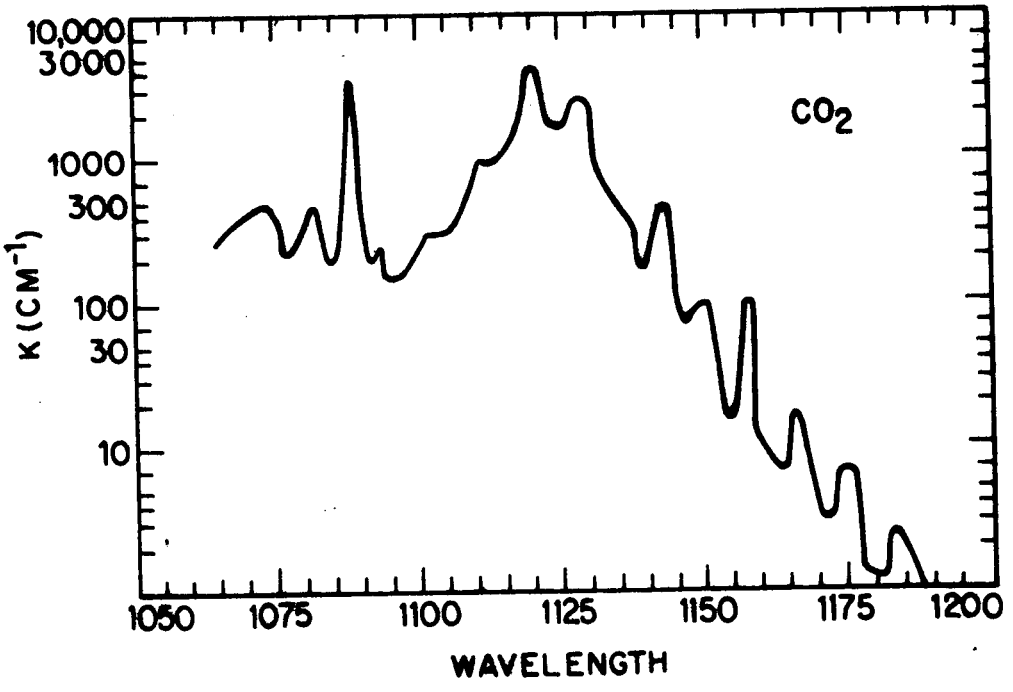

Figure 38 UV absorption coefficient of CO_2

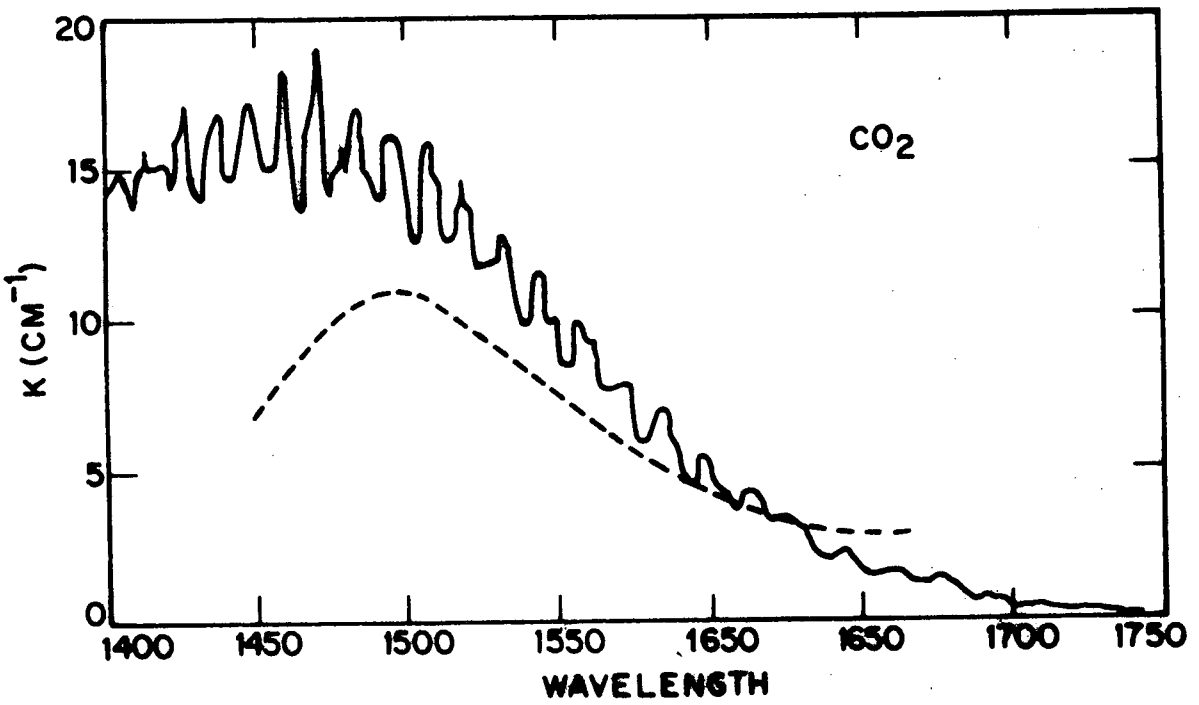

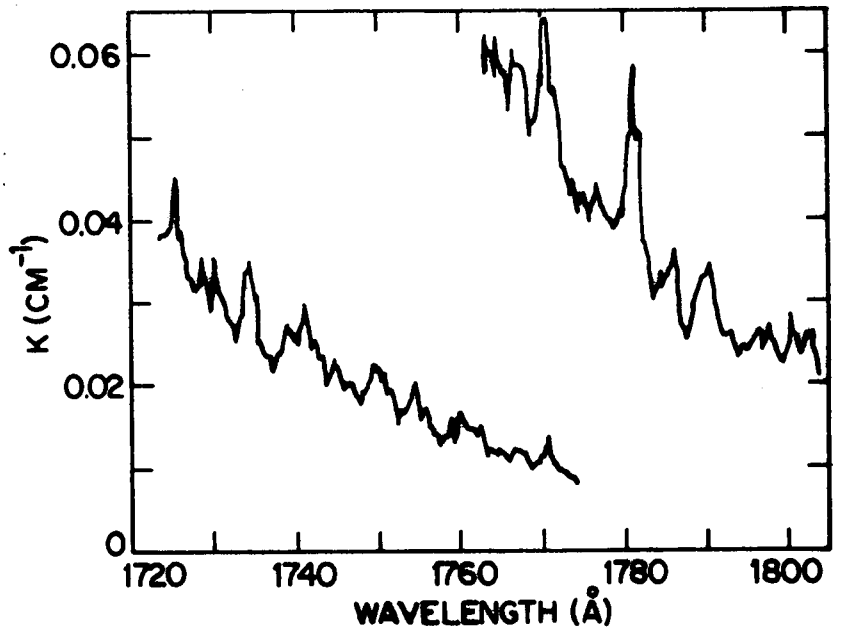

Figure 39 UV absorption coefficient of CO_2

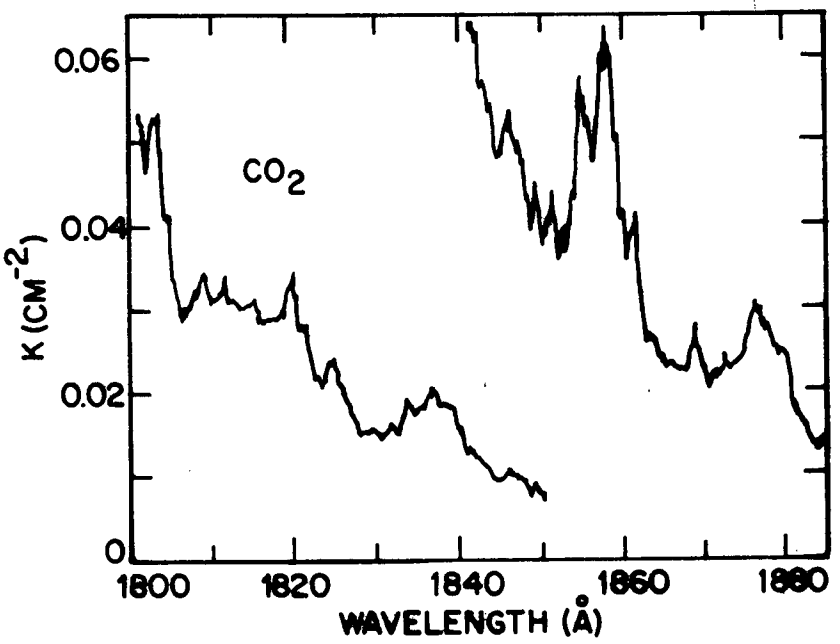

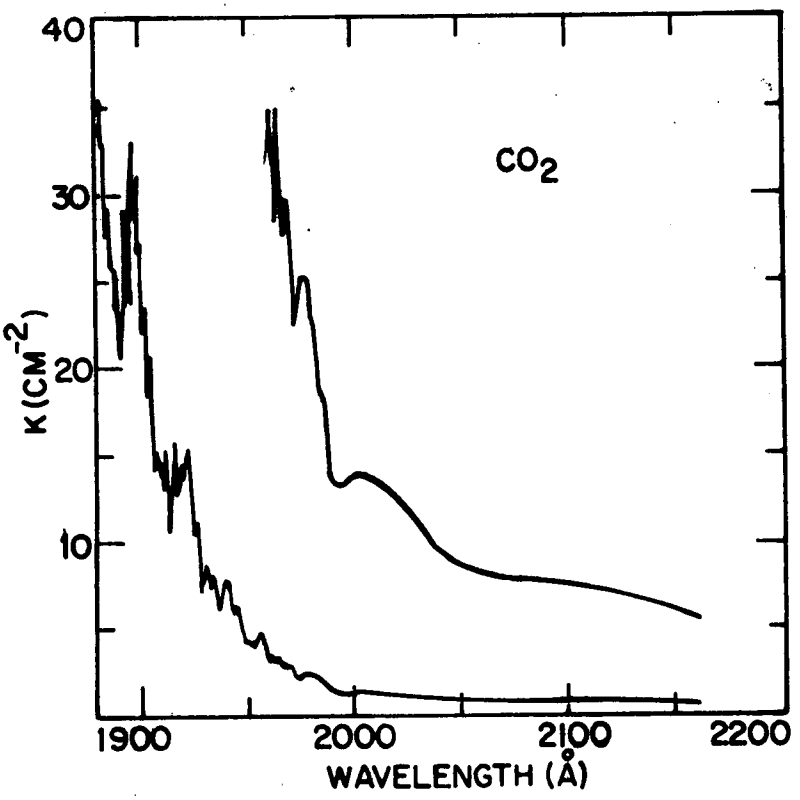

Figure 40 UV absorption coefficient of CO_2

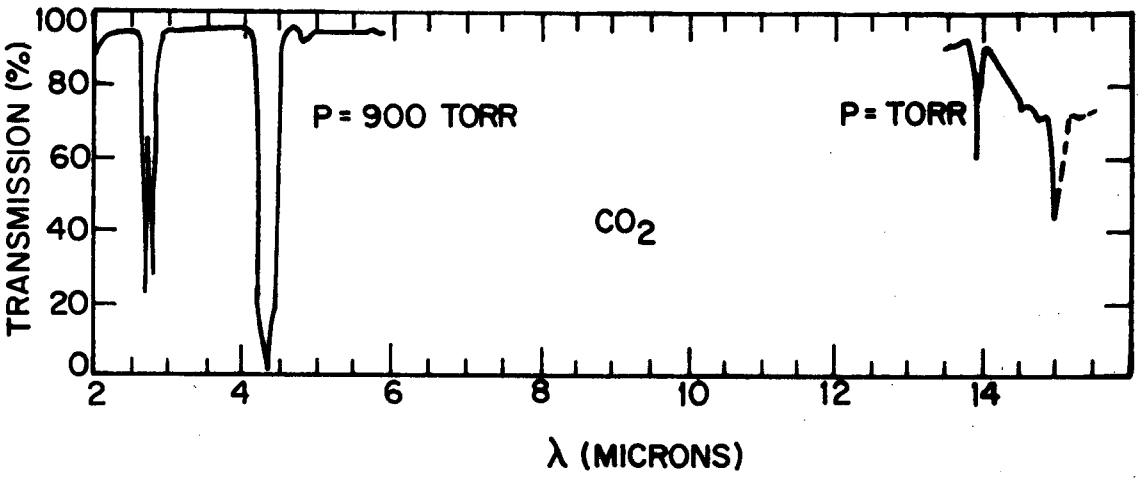

Figure 41 Infrared bands of carbon dioxide

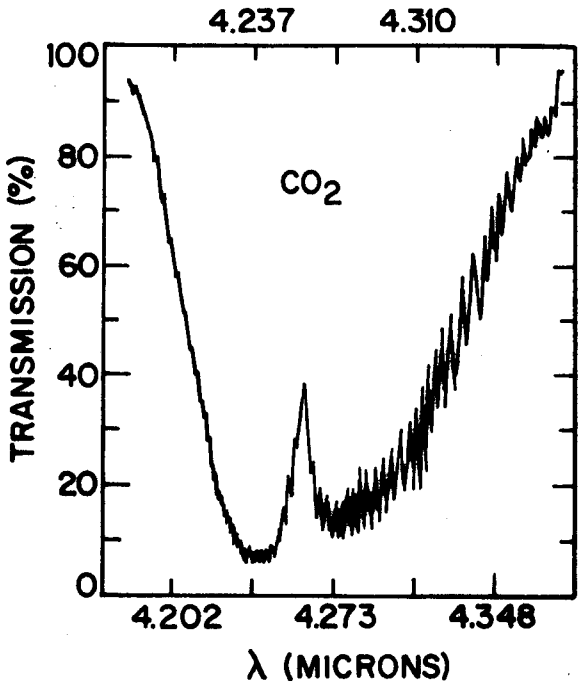

Figure 42 Transmission in 4.26 micron band of CO_2

Argon

The absorption of the monotomic gas, argon, while lacking the intricate structure of molecular bands, possesses considerable structure due to the presence of atomic lines in the vacuum UV. The data of Henke (Ref. 9) in Figure 6 shows the K- and L-edges at 3.87Å and 38Å. The region between 38Å and 600Å is covered by data from Hudson and Kieffer's (Ref. 25) compilation. Figure 43 gives Cook and Ching's results for the 600 to 800Å spectral region showing the sharp change in absorption at the ionization limit 787Å, (Ref. 14). Detailed structure at wavelengths just short of the ionization limit is shown in Figure 44, from Huffman, Tanaka and Larrabee (Ref. 26). These broad lines are due to transitions to states lying above the ionization limit of the atom. These states then decay quickly without radiation to an argon ion and a free electron.

A list of the wavelengths and oscillator strengths of the absorption lines of the argon atom is given below, using data of Wiese, Smith and Miles (Ref. 27).

Wavelength	f-Value
876.06A	0.093
866.80	0.106
1066.66	0.061
1048.22	0.254
879.95	0.0268
869.75	0.0119

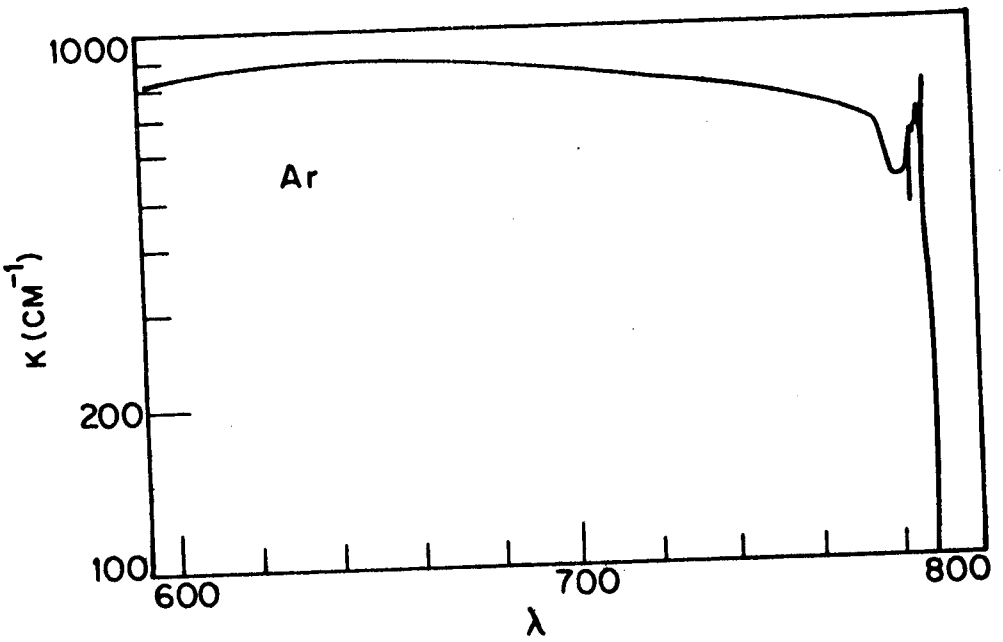

Figure 43 Absorption coefficient of Argon

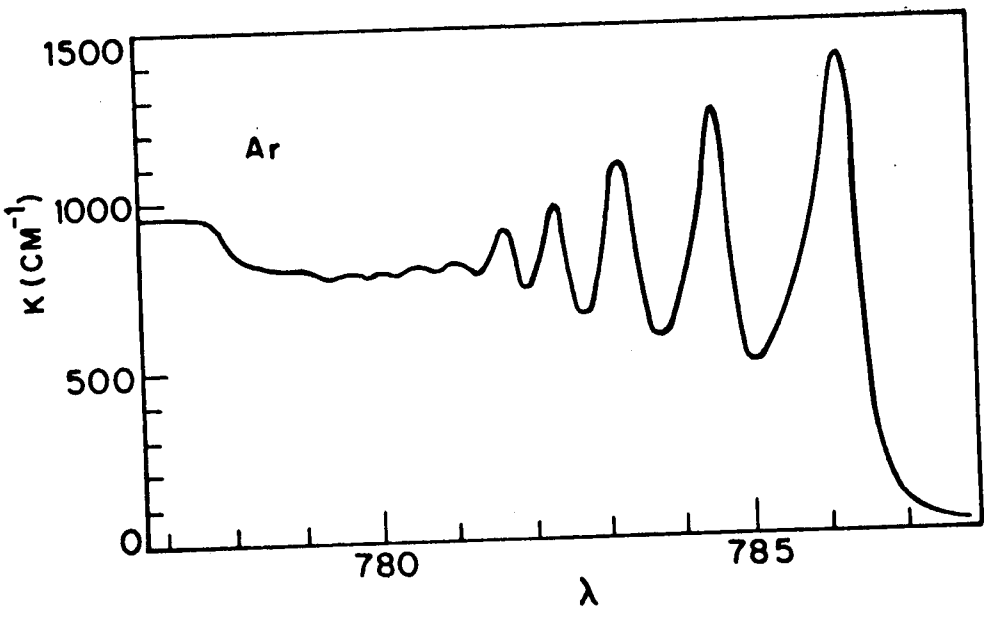

Figure 44 Absorption coefficient of Argon; detail near limit

Helium

Absorption in helium is confined to wavelengths below the photo-ionization limit at 504Å, except for the resonance lines at wavelengths up to 584Å. Because of the extreme variation in absorption coefficient between 1Å and 504Å, Figure 8 contains a plot of K/λ^2 vs. λ. Data were obtained from Henke (Ref. 9) and Samson (Ref. 28).

Wavelengths and oscillator strengths for the prominent resonance absorption lines of the helium atom are listed below, as obtained from Weise, et. al., (Ref. 29).

Wavelength	f-Value
584.334	0.2762
537.030	0.0734
522.213	0.0302
515.617	0.0153
512.098	0.00848
509.998	0.00593
508.643	0.00399
507.718	0.00275

etc. to the ionization limit

APPENDIX B

Fluorescence Mechanisms and Data

The molecules in the SPARCS propellant plumes will be exposed to sunlight and earthshine causing them to emit fluorescent radiation which may degrade onboard optical experiments, especially broad band detectors focusing on weak stellar light sources. The fluorescence is generally distributed among discrete molecular band systems, atomic lines, and continua. The bulk of the UV and visible fluorescence of CO_2 for example is contained in five emission band systems. These are the A → X and B → X systems of CO_2^+ in the visible and near UV, the a → x and A → X systems of CO and the B → X system of CO^+ in the far UV and VUV. The CO_2 fluorescence comes from excited states produced by photo-ionization and photo-dissociation.

Six important fluorescence mechanisms are listed below. M refers to a propellant gas molecule and z and y refer to photo-dissociation products. An asterisk on a symbol indicates that the corresponding molecule, ion, or atom is in an excited state. The mechanisms are

(2) $h\nu + M \rightarrow M^* \rightarrow M + h\nu'$ — resonance fluorescence

(3) $h\nu + M \rightarrow M^{*+} + e \rightarrow M^+ + h\nu' + e$ — photo ionization fluorescence

(4) $h\nu + M \rightarrow M\,(zy^*)^* \rightarrow z + y^* \rightarrow z + y + h\nu'$ — photo dissociation fluorescence

(5) $h\nu + z \rightarrow z^* \rightarrow z + h\nu'$

(6) $h\nu + M^+ \rightarrow M^{*+} \rightarrow M^+ + h\nu'$

(7) $h\nu + z^+ \rightarrow z^{*+} \rightarrow z^{*+} + h\nu'$

(5), (6), (7) — resonance fluorescence of fragments, ions, and ionized fragments

For each of these six mechanisms it is convenient to define a quantity

g_i for each band system or line such that the intensity I of fluorescent radiation incident on a detector viewing along a cm^2 column containing a number N of molecules is given by

(8) $4\pi I = g_i N$

The subscript indicates which of the six production mechanisms above is responsible for the fluorescence. The units of N are molecules cm^{-2} and, following the usual conventions, those of I are photons sec^{-1} cm^{-2} $sterad^{-1}$ for UV and visible light or watts cm^{-2} $sterad^{-1}$ for IR light. The units of g_i then are photons sec^{-1} $molecules^{-1}$ for UV and visible light and watts $molecule^{-1}$ for IR light. For example, the resonance fluorescence g_i factor for the CO_2 band system near 15.4μ is 1.8×10^{-22} watts $molecule^{-1}$ so that for $N = 10^{12}$ molecules cm^{-2} the intensity in this band is given by

$$I = \left(\frac{1}{4\pi}\right) g_1 N = 1.45 \times 10^{-11} \text{ watts cm}^{-2} \text{ sterad}^{-1}$$

The initial step in mechanisms (2) through (7) is a photon absorption process thus g is given by

(9) $$g_1 = \int d\lambda\ \sigma_i(\lambda)\pi F_\lambda \simeq \frac{\pi e^2}{mc}\ f_i\ \pi F_\lambda$$

Here πF_λ is the total irradiance (due to earth and sun) in units of photons sec^{-1} cm^{-2} $Hertz^{-1}$ for UV and visible radiation and watts cm^{-2} $Hertz^{-1}$ for IR radiation and where $\sigma_i(\lambda)$ is the cross section in units cm^{-2} for a photon of wavelength λ to induce reaction i. πF_λ may be written as the sum of the irradiance due to earth πF_λ^e and sun πF_λ^s and g then may be rewritten as the sum $g = g^s + g^e$

with

$$g^s = \int d\lambda\ \sigma(\lambda)\ \pi F_\lambda^s$$

and

$$g^e = \int d\lambda \ \sigma(\lambda) \ \pi F_\lambda^e$$

in this paper πF_λ^s always refers to the solar flux evaluated at the earth's distance from the sun, one astronomical unit. Hence numerical values of g^s stated anywhere in this paper apply to space vehicles very near the earth's orbit and must be corrected by the factor r^{-2} with r the distance from space vehicle to sun measured in astronomical units if the vehicle is located elsewhere in the solar system. The g^e found in this text may similarly be corrected for distance from the earth. Let d designate the distance of the space vehicle from the center of the earth in units of earth radii then g^e is given as a function of d by

$$g^e(d) = g^e(1) \left(\frac{d - \sqrt{d^2 - 1}}{d} \right)$$

Numerical values of g^e listed anywhere in this text refer to d = 1.

The approximate form of equation 9

$$g_i \simeq \frac{\pi e^2}{mc} \ f_i \ \pi F_\lambda$$

applies when πF_λ is reasonably constant over regions for which $\sigma_i(\lambda) = 0$. This is always the case for the resonance fluorescence process (2). f_i is the oscillator strength for the initial upwards electronic radiative transition. Resonance fluorescence g_1 factors are given in Table 3 for the important IR bands of all the propellant gases. The oscillator strength data were taken from the compilation of Penner (Ref. 24). The g factors are given for the case where the molecules are illuminated by both the earth and the sun and for the case where they are illuminated by just the earth

Table 3 IR Resonance Fluorescence G Factors of Propellant Gas Molecules

Molecule	Wavelength	Figure in text Illustrating Band Structure	g Factors in watts molecule^{-1}	
			(g^e+g^s) Molecule Illuminated by Earth and Sun (Daytime)	g^e Molecule Illuminated by Earth Alone (Nighttime)
CO_2	1.96μ	Fig. None	$.71 \times 10^{-25}$	$.135 \times 10^{-30}$
CO_2	2.01μ	Fig. None	$.164 \times 10^{-24}$	$.55 \times 10^{-30}$
CO_2	2.06μ	Fig. None	$.424 \times 10^{-25}$	$.252 \times 10^{-30}$
CO_2	2.69μ	Fig. 41	$.456 \times 10^{-23}$	$.535 \times 10^{-26}$
CO_2	2.77μ	Fig. 41	$.294 \times 10^{-23}$	$.564 \times 10^{-26}$
CO_2	4.26μ	Fig. 42	$.136 \times 10^{-21}$	$.5 \times 10^{-26}$
CO_2	4.77μ	Fig. 41	$.148 \times 10^{-25}$	$.86 \times 10^{-26}$
CO_2	5.26μ	Fig. 41	$.565 \times 10^{-26}$	$.267 \times 10^{-26}$
CO_2	15.4μ	Fig. 41	$.182 \times 10^{-21}$	$.181 \times 10^{-21}$
CF_4	15.8μ	Fig. 28	$.508 \times 10^{-20}$	$.506 \times 10^{-20}$
CF_4	7.89μ	Fig. 28	$.177 \times 10^{-22}$	$.169 \times 10^{-22}$
NH_3	2.90μ	Fig. 35	$.126 \times 10^{-23}$	$.501 \times 10^{-26}$
NH_3	3.60μ	Fig. 35	$.184 \times 10^{-23}$	$.121 \times 10^{-25}$
NH_3	6.14μ	Fig. 35	$.553 \times 10^{-23}$	$.254 \times 10^{-23}$
NH_3	10.52μ	Fig. 35	$.122 \times 10^{-20}$	$.122 \times 10^{-20}$

(night time). Earth shine provides the most illumination for wavelengths longward of about 5μ while sun shine is dominant for wavelengths shortward of 5μ. The solar flux was assumed to be that of a 6000°K black body, properly diluted to account for its $(1/r)^2$ decrease in intensity on arrival at the earth and the earth shine was taken from The Satellite Environment Handbook (Ref. 30). N_2H_4 has not been included in Table 3 since it is dissociated by propellant motor operation into 25% NH_3, 46% H_2 and 29% N_2 (Pearce et al., (Ref. 2).

Next consider process (3). A well known example is

(10) $h\nu + N_2(X^1\Sigma_g) \rightarrow N_2^+ (B^2 \Sigma_v^+) + e$

followed by

$$N_2^+ (B^2 \Sigma_v^+) \rightarrow N_2^+ (X^2 \Sigma_g^+) + h\nu'$$

which leads to fluorescence at 3914Å, 4234Å, and 3584Å, corresponding to the (0-0), 0-1) and (1-0) bands of the N_2^+ B → X system. The g_2 factor for this process is (Ref. 31)

$$g_2(N_2^+, B \rightarrow X) \cong 1.0 \times 10^{-8} \text{ sec}^{-1} \text{ molecule}^{-1}$$

so the intensity in photons sec^{-1} cm^{-2} sterad^{-1} in the B - X system of N_2^+ for $N = 10^{12}$ cm^{-2} is

$$I(N_2^+ B \rightarrow X) = \frac{1}{4\pi} g_2(N_2^+, B\text{-}X)\, N = .8 \times 10^3 \text{ photons sec}^{-1} \text{ cm}^{-2} \text{ sterad}^{-1}$$

The CO A-X Cameron bands provide an example of mechanism 3. These bands are a prominent feature in the Martian dayglow. Barth (Ref. 3) reports a cm^2 column excitation rate of 20 kR* which represents a large

* 1 kR = kiloRayleigh = 10^9 photons $\text{cm}^{-2}\text{sec}^{-1}$ when referring to column excitation rates; an equivalent definition is 1 kR = 10^9 photons cm^{-2} sec^{-1} $(\text{sterad}/4\pi)^{-1}$ when referring to the apparent brightness of an extended source.

fraction of the solar flux incident on the Martian atmosphere that is energetic enough ($\lambda \leq 1028$Å) to dissociate CO_2 into $CO(a^3\pi)$. From these data one may estimate an upper limit on $g_3(CO, a\text{-}x)$ if one assumes the entire Martian CO a-x dayglow (Barth et al., ref. 3) is due to the process

(11) $$h\nu + CO_2 \rightarrow O + CO(a^3\pi)$$

the result is

(12) $$g_3(CO,a\text{-}x) \leq 5 \times 10^{-7} \text{ sec}^{-1}$$

so for $N = 10^{12}$ CO_2 molecules in a cm^2 column along the detector viewing direction the fluorescent intensity in the CO a-x band system is

(13) $$4\pi I(CO,a\text{-}x) \leq g_3(CO,a\text{-}x)\ N = 5 \times 10^5 \text{ photons.cm}^{-2}.\ \text{sec}^{-1}$$

Some examples of processes (4) through (6) are as follows

(14) $$h\nu + H(^2S) \rightarrow H(^2P) \rightarrow h\nu' + H(^2S); \quad \lambda \simeq 1216\text{Å}.$$

The resonance scattering of solar Ly-α emission by hydrogen, a dissociation product of NH_3 and N_2H_4

(15) $$h\nu + N_2^+ (X^2\Sigma_g^+) \rightarrow N_2^+ (B^2\Sigma_u^+) \rightarrow h\nu' + N_2^+ (X^2\Sigma_g^+), \ \lambda \simeq 3914\text{Å}.$$

The resonance fluorescence of sunlight by N_2^+

(16) $$h\nu + CO^+ (X^2\Sigma^+) \rightarrow CO^+ (B^2\Sigma^+) \rightarrow h\nu' + CO^+(X^2\Sigma^+), \ \lambda \simeq 1150\text{Å}.$$

The resonance fluorescence of sunlight by CO^+, an ionized fragment of CO_2.

The population of fragments, ions and fragment ions produced from parent gas clouds via reactions (3) and (4) will initially increase linearly with

respect to time measured from the inception of a particular pulse cloud. If the g factor for resonance fluorescence of these products in a given band is much larger than for the excitation of these product bands via reactions (5) or (6) there will come a time τ_R when the radiation via resonance fluorescence of parent gas ions or dissociation fragments will equal that produced by photoionization or dissociation of the parent gas itself. Take the case of the N_2^+ B-X band system for example. Radiation is produced in this band system via mechanism (4) at the rate

$$4\pi I_3(N_2^+, \text{B-X}) = g_3(N_2^+, \text{B-X})N(N_2)$$

where $N(N_2)$ is the number of N_2 molecules in a line of sight cm^2 column and it is produced via mechanism (6) at the rate

$$4\pi I_5(N_2^+, \text{B-X}) = g_5(N_2^+, \text{B-X})N(N_2^+)$$

but in the absence of any recombination mechanism $N(N_2^+)$ is related to $N(N_2)$ by

$$N(N_2^+) \cong t\ r\ N(N_2)$$

where $r \cong 3 \times 10^{-7}$ sec^{-1} deduced from the data reported by Hinteregger et al. (ref. 32) is the probability sec^{-1} that an N_2 molecule will be ionized when exposed to solar radiation and where t is the time elapsed from cloud inception. The time τ_R when the N_2^+ B-X radiation $4\pi I_5$ produced by resonance fluoresence of sunlight by N_2^+ is equal to that produced by photoionization of N_2 to the $N_2^+(B)$, $4\pi I_3$, is given by

$$g_3(N_2^+, \text{B-X})\ \tau_R\ r\ N(N_2) = g_5(N_2^+, \text{B-X})\ N(N_2)$$

or

$$\tau_R = g_5(N_2^+, B\text{-}X)/r\ g_3(N_2^+, B\text{-}X)$$

and $g_3(N_2^+, B\text{-}X) = .05\ sec^{-1}$ (Hunten, 1971) so that

$$\tau_R = .67\ sec$$

so in deep space where the propellant gas cloud moves along with the vehicle mechanism (5) will be important.

Not surprisingly, the bulk of the sunlit UV and visible fluorescence data obtained to date pertains to gases that comprise planetary atmospheres. Thus, N_2, H and He have been studied in the context of the earth's dayglow (Hunten, ref. 31). Observations of the Martian dayglow (Barth et al., ref. 3) have led to correlated laboratory studies of CO_2 fluorescence, figures(45-49). The spectrum of a simulated Jovian atmosphere was obtained on the Mariner 6 and 7 mission by viewing the 'sunlit dissociation products' of N_2H_4 in deep space (Pearce et al., ref. 2). The N_2H_4 dissociated into 25% NH_3, 46% H_2, and 29% N_2. The spectrum is shown in figure (9). It gives more of a qualitative than quantitative picture of the fluorescence of dissociated N_2H_4 in sunlight since it is not clear how much of the spectrum comes from mechanisms (3) and (4) as opposed to mechanisms (5) through (7) hence the nature of the spectrum might change considerably over a given time interval. It is evident too that the operation of a hypothetical pointing control motor on board Mariners 6 and 7 utilizing N_2H_4 as a propellant gas during the recording of the Martian dayglow spectra may have confused the

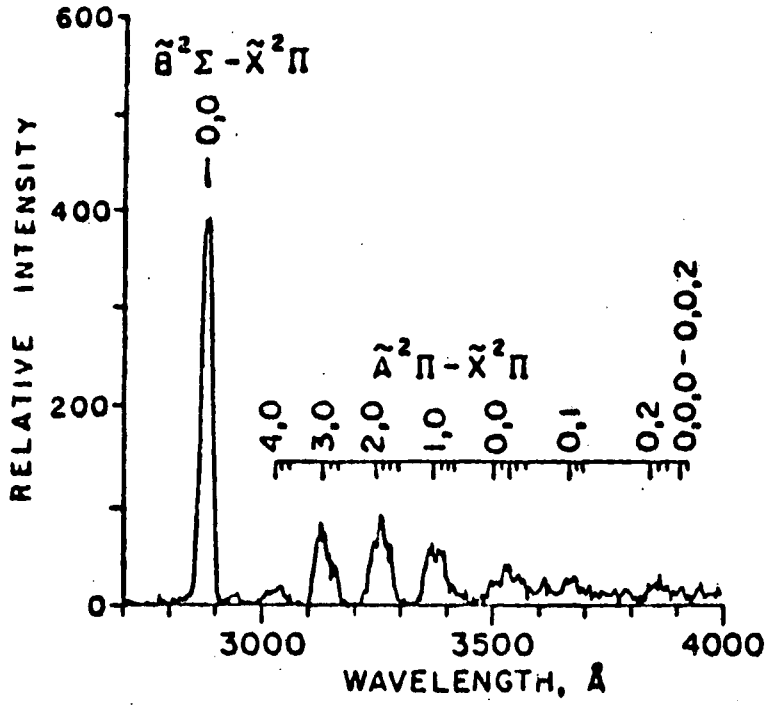

Figure 45 Photoionization Excitation Spectrun of CO_2 - Produced in Laboratory with 584 A Photons

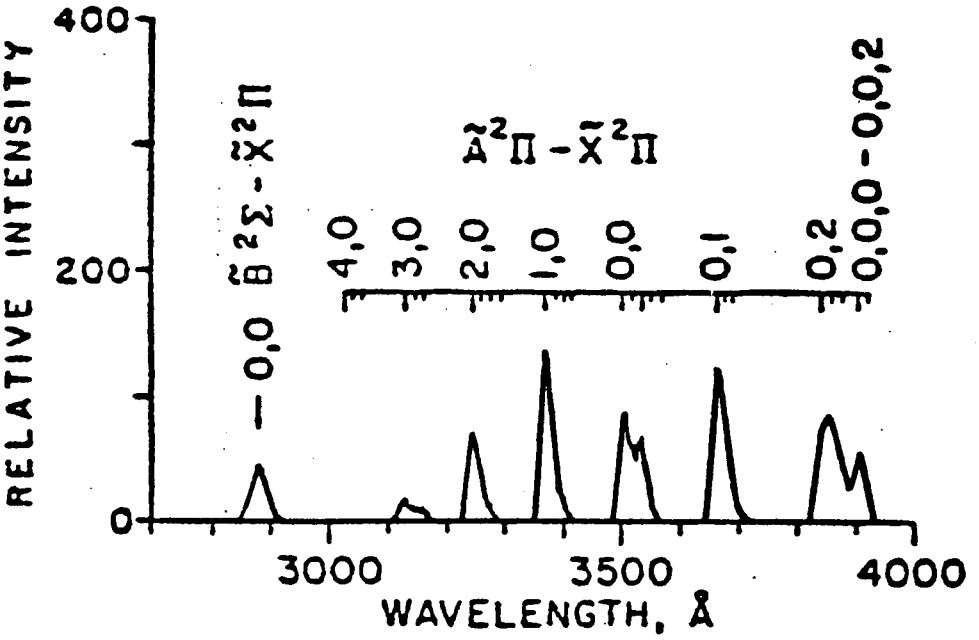

Figure 46 Theoretical Fluorescent Scattering Spectrum for CO_2^+

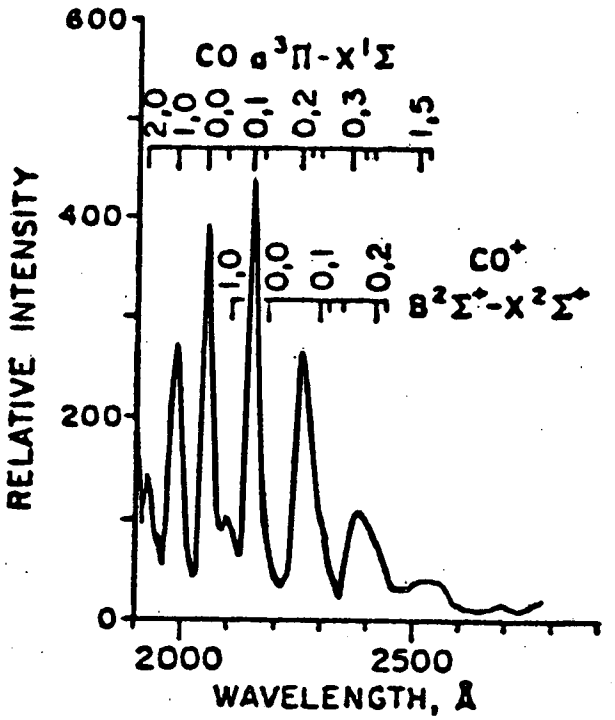

Figure 47 Excitation Spectrum of CO_2 - Produced with 20 ev Electrons

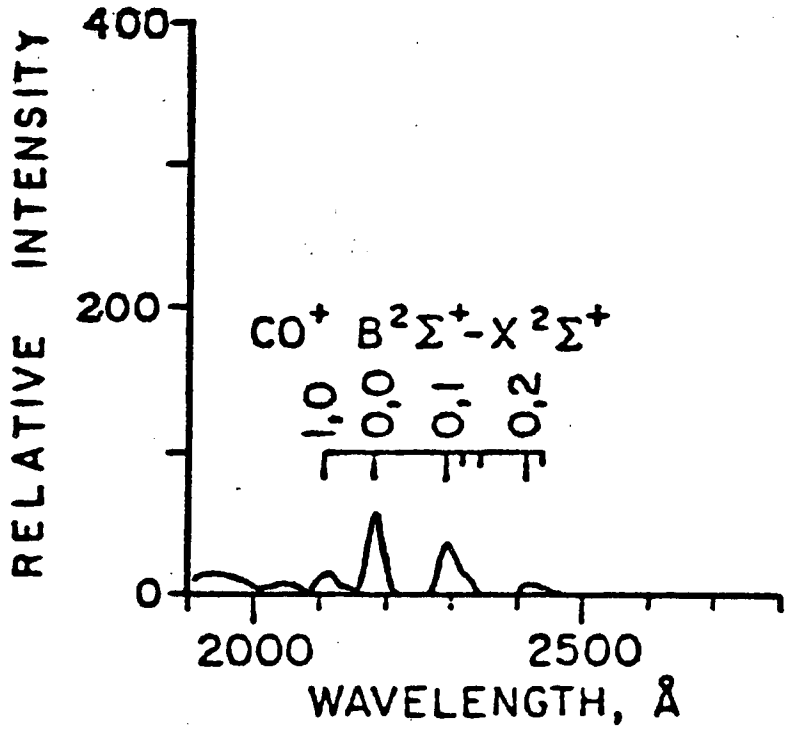

Figure 48 Excitation Spectrum of CO_2 - Produced with 50 ev Electrons

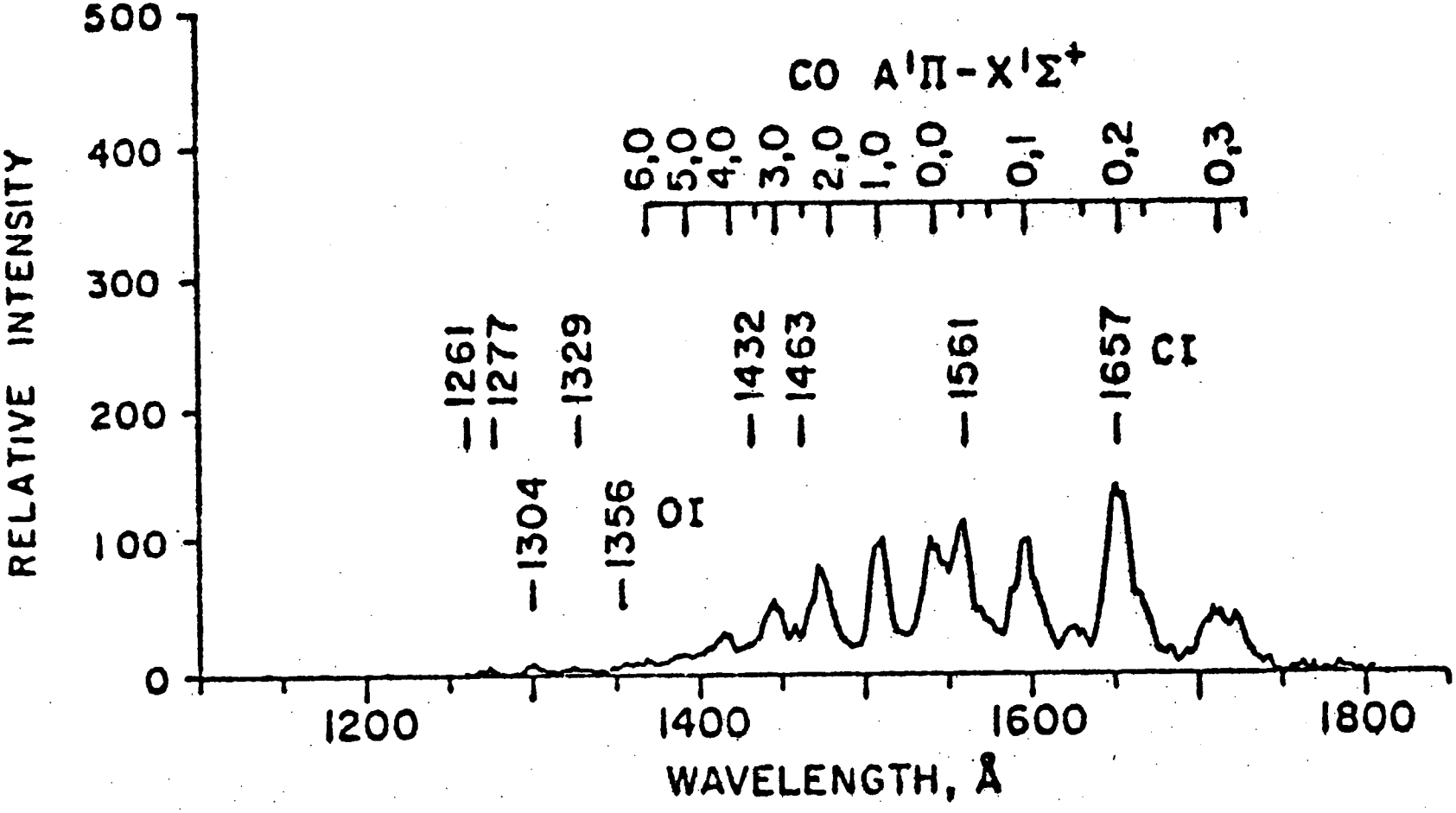

Figure 49 Excitation Spectrum of CO_2 - Produced with 20 ev Electrons

interpretation of these spectra. If the number of N_2^+ ions in a cm^2 column along the detector line of sight were 10^8 (not unreasonable in deep space), then the intensity at 3914Å due to resonance scattering by N_2^+ would be comparable to the CO_2^+ A-X emission at this wavelength and if this were not corrected for it would lead to the erroneous conclusion that appreciable nitrogen exists in the Martian atmosphere.

Some information on sunlit UV and visible fluorescence of the gases N_2, He, H, CO_2, NH_3, and H_2 has been obtained by the study of planetary atmospheres, parallel laboratory studies, and the study of simulated atmospheres. CF_4, one of the most important gases in the SPARCS program, is not an important constituent of any known planetary atmosphere and its fluorescent properties were relatively unknown until now. Studies by Cook and Ching (ref. 1) showed that it does fluoresce when illuminated by light of wavelength near 910Å.

The resultant radiation is shortward of 3000Å and its spectrum is given in fig. (8). Similar studies to obtain more accurate g factors for the other gases would be useful not only from the point of view of the SPARCS project, but also from that of the physics of planetary atmospheres as pointed out above. Table 4 lists all the known UV and visible fluorescent band systems or lines of propellant gas molecules that may be important. The g factors are given or estimated when possible. They are evaluated at the distance of the earth from the sun, but may be corrected by the factor r^2 as described above for other positions in the solar system. Earthshine does not contribute to the g factors for UV and visible radiation. A description of the

Table 4 The Fluorescent Properties of the Parent Propellant Gas Molecules

Fluorescing Gas Molecule	Process	Band System Or Line	λ Wavelength of Exciting Radiation	λ' Wavelength of Fluorescing Radiation	Representative Fluorescent Spectrum	g Factor Units=Photons sec^{-1} $molecule^{-1}$
CF_4	Photo-dissociation	CF_3	860Å ≤ λ ≤ 940Å	2100 < λ < 3100	Fig. 8	≤ 2.6×10^{-7}
CO_2	Photo-dissociation	CO, $a^3\Pi \rightarrow X'\Sigma$	λ ≤ 1028Å	1700Å ≤ λ' ≤ 2500Å	Fig. 10, 47	≤ 5×10^{-7}
CO_2	"	CO, $A'\Pi - X'\Sigma$	λ ≤ 920Å	1300A ≤ λ' ≤ 1750Å	Fig. 10, 49	≤ $.5 \times 10^{-7}$
CO_2	Photo-ionization	CO_2^+, $\tilde{A}^2\Pi - \tilde{X}^2\Pi$	λ ≤ 716Å	3000Å ≤ λ' ≤ 4000Å	Fig. 11, 45	≃ 1.7×10^{-7}
CO_2	"	CO_2^+, $\tilde{B}^2\Sigma - \tilde{X}^{2\Pi}$	λ ≤ 686Å	λ' ≃ 2865Å	Fig. 11, 45	≃ $.9 \times 10^{-7}$
CO_2	Photo-dissociation	O, $^5S \rightarrow {}^3P$	λ ≤ 850Å	≃ 1356Å	Fig. 10, 49	10^{-9}
CO_2	"	O, $^3S \rightarrow {}^3P$	λ ≤ 830Å	≃ 1304Å	Fig. 10, 49	?
CO_2	"	O, $^1S \rightarrow {}^3P$	λ ≤ 1290Å	≃ 2972Å	Fig. 10, 45	10^{-8}
CO_2	"	C, $^3P \rightarrow {}^3P$	λ ≤ 626Å	1261Å	Fig. 10, 49	?
CO_2	"	C, $^3P \rightarrow {}^3P^o$	λ ≤ 631Å	1277Å	Fig. 10, 49	?
CO_2	"	C, $^3P \rightarrow {}^3P^o$	λ ≤ 645Å	1329Å	"	?
CO_2	"	C, $^5P \rightarrow {}^5S^o$	λ ≤ 545Å	1432Å	"	?
CO_2	"	C, $^1F \rightarrow {}^1D$	λ ≤ 630Å	1463Å	"	?
CO_2	"	C, $^3D \rightarrow {}^3P$	λ ≤ 690Å	1561Å	"	?
CO_2	"	C, $^3P \rightarrow {}^3P^o$	λ ≤ 710Å	1657Å	"	10^{-7}
NH_3	"	NH_2, $\tilde{A}^2A_1 \rightarrow \tilde{X}^2B_1$	1000Å ≤ λ ≤ 1640Å	4000Å-6000Å		≤ 2.1×10^{-8}
NH_3	"	NH, $C'\Pi \rightarrow a'\Delta$	λ ≤ 1325Å	≃ 3255Å	Fig. 9	≃ 2×10^{-8}

Table 4 (Continued)

Fluorescing Gas Molecule	Process	Band System Or Line	λ Wavelength of Exciting Radiation	λ' Wavelength of Fluorescing Radiation	Representative Fluorescent Spectrum	g Factor Units = Photons sec^{-1} $molecule^{-1}$
NH_3	Photo-dissociation	$NH, A^3\Pi \rightarrow X^3\Sigma$	$\lambda \leq 1020Å$	$\simeq 3340Å$	Fig. 9	$3 \times 10^{-8} - 15 \times 10^{-8}$
NH_3	"	$NH, b'\Sigma^+ \rightarrow a'\Delta$	$\lambda \leq 1875Å$	$\simeq 11,550Å$		?
NH_3	"	$NH, d'\Sigma^+ \rightarrow b'\Sigma^+$	$\lambda \leq 870Å$	$\simeq 1625Å$		?
NH_3	"	$NH, d'\Sigma^+ \rightarrow c'$	$\lambda \leq 870Å$	$\simeq 2525Å$		?
NH_3	"	$H, {}^2P \rightarrow {}^2S$	$\lambda \leq 850Å$	$1216Å$	Fig. 9	?
NH_3	"	$H, {}^2P \rightarrow {}^2S$	$\lambda \leq 750Å$	$1026Å$		?
NH_3	"	$N, {}^4P \rightarrow {}^4S$	$\lambda \leq 690Å$	$1200Å$	Fig. 9	?
H_2	Resonance fluorescence	H_2,	$950Å \leq \lambda \leq 9050Å$	$950Å - 1650Å$	Fig. 9	?
H_2	Photo-dissociation	$H, {}^2P - {}^2S$		$1216Å$	Fig. 9	4.5×10^{-8}
N_2	Photo-ionization	$N_2^+, A^2\Pi - X^2\Sigma$	$\lambda \leq 745Å$	$3914Å$	Fig. 9	10^{-8}
N_2	"	$N_2^+, B^2\Sigma - X^2\Sigma$	$\lambda \leq 665Å$	$11,300Å$		2.8×10^{-8}
He	Resonance fluorescence	He, $^1P - {}^1S$	$584Å$	$584Å$		2×10^{-5}
He	"	He, $^1P - {}^1S$	$537Å$	$537Å$		5×10^{-7}

estimation procedure and pertinent references are given below for each g factor along with comment when possible on its accuracy. Table 5 lists the g factors of important propellant gas fragments, ions and ionized fragments.

The g factors listed in Table 4 and 5 are for the most part rough estimates (usually accurate within a factor of 2 or better) or upper limits. One may use these to estimate the fluorescent background that a given propellant gas may create in an interesting wavelength region.

The most important fluorescent radiation from CF_4 comes from photodissociation products. This is the case for CO_2 also. The Martian dayglow data shows that the metastable system $A^3\pi - X^1\Sigma$ of CO produced by solar photodissociation of CO_2 accounts for about 70% of the <u>entire</u> solar-induced fluorescent spectrum of CO_2. One would never predict this on the basis of Cook and Ching's (ref. 14) CO_2 fluorescent data because the quenching of the photodissociation-produced metastable CO ($A^3\pi$) state masked the production of this important CO_2 fluorescent radiation.

A description of the estimation procedure and the pertinent references by which the g factors listed in Table 4 were obtained are given here. Cook and Ching (ref. 1) report that radiation of wavelength $870\text{Å} \leq \lambda \leq 9500\text{Å}$ incident on CF_4 produces a fluorescent radiation of wavelength $\lambda' \leq 3000\text{Å}$. From their data and from the solar flux data of Hinteregger et al. (ref. 32) one may estimate an upper limit on the g factor for production of this fluorescent radiation. There may be some additional CF_4 fluorescence due to radiative

Table 5 The Resonance Fluorescence Properties of the Important Fragments, Ions and Ionized Fragments

Fragment, Ion or Ionized Fragment	Band System or Line	Wavelength	Oscillator Strength	g Factor in Units of Photons sec^{-1} $molecule^{-1}$	References
CO	$A'\Pi \rightarrow X'\Sigma$	1300Å-1750Å	.023	$.52 \times 10^{-7}$	f from Hesser, ref. 33
CO	$C'\Sigma - X'\Sigma$	1100Å	.131	$.25 \times 10^{-6}$	"
CO_2^+	$\tilde{A}^2\Pi - X^2\Pi$	3000Å-4000Å	.012	$.88 \times 10^{-2}$	"
CO_2^+	$B^2\Sigma - X^2\Pi$	2865Å	.011	$.615 \times 10^{-2}$	"
CO^+	$B^2\Sigma - X^2\Sigma$	2100Å-2600Å	.013	$.18 \times 10^{-5}$	"
NH_2	$\tilde{A}^2A_1 \rightarrow \tilde{X}^2B_1$	4000Å-9000Å		?	
NH	$A^3\Pi - X^3\Sigma$	3340Å		?	
NH	$c'\Pi - a'\Delta$	3255Å		?	
H	$^2P - ^2S$	1216Å		$.21 \times 10^{-2}$	g from Hunten, ref. 31
N_2^+	$A^2\Pi - X^2\Sigma$	11,300Å		$.42 \times 10^{-1}$	"
N_2^+	$B^2\Sigma - X^2\Sigma$	3914Å		$.50 \times 10^{-1}$	"

decay of relatively long lived metastable photodissociation products. This could not be observed in the experiment of Cook and Ching (ref. 1) since the metastable if present would be collisionally deactivated by the walls rather than radiate due to the relatively long lifetime of metastable against radiative decay. The results obtained for CO_2 by Cook and Ching (ref. 14) give no hint for example that the dominant fluorescent radiation of CO_2 is the CO $a^3\pi \rightarrow X'\Sigma$ Cameron band system, which originates from the photodissociation production of metastable $CO(a^3\pi)$. Cross sections $\sigma_B(\lambda)$ and $\sigma_A(\lambda)$ as a function of wavelength for the photoionization excitation of the $CO_2^+ \tilde{B}^2\Sigma_u^+$ and $\tilde{A}^2\pi_u$ states are given by Bahr et al. (ref. 34). g is given by (equation 9 in the text)

$$g = \int d\lambda\ \sigma(\lambda)\ \pi F_\lambda$$

so one may easily obtain g_B and g_A for the reactions

$$h\nu + CO_2 \rightarrow CO_2^+ (\tilde{B}^2\Sigma_u) + e$$

$$h\nu + CO_2 \rightarrow CO_2^+ (\tilde{A}^2\pi_u) + e$$

The g factors for the other important fluorescent photo reactions of CO_2 that are listed in Table 4 were estimated to within a factor of 2 by comparing the relative intensities of the corresponding fluorescent radiations in the Martian dayglow as reported by Barth et al. (ref. 3). The g factors for the photodissociation excitation of the $NH_2\tilde{A}^2A_1 \rightarrow \tilde{X}^2B_1$ and the NH $A^3\pi \rightarrow X^3\Sigma^-$ and $c'\pi \rightarrow a'\Delta$ band systems are estimated from the fluorescent yield data of Okabe and Lenzi (ref. 35) and Cook and Ching (ref. 14); the absorption data of Nicolet (ref. 18) and the solar flux data cited above. The g factors for the production of hydrogen Ly-α at

1216Å by photodissociation and of the N_2^+ A → X and B → X band systems are listed by Hunten (ref. 31). The g factor for the resonance scattering of 584Å sunlight by helium was deduced within a factor of 2 from 584Å dayglow measurements reported by Donahue and Kumer (ref. 36). The g factor for resonance scattering of 537Å sunlight by helium was obtained by adjusting the corresponding g factor of 584Å for the reduced solar flux at 537Å and for the smaller oscillator strength of the radiative transition associated with 537Å helium line.

APPENDIX C

Fluorescence Spectrum of CF_4

The fluorescence excited when CF_4 is irradiated by uv radiation of wavelength between 870 and 930Å was observed by Cook and Ching (ref. 1) to lie at wavelengths less than 3000Å. In the present work, the uv excited fluorescence was spectrally resolved. In addition, CF_4 was excited by electron impact and the resulting emission spectrum was observed with better spectral resolution to determine the origin of the fluorescence by observing its threshold energy. In particular, three types of measurement were made:

a) The fluorescence of CF_4 excited by uv at 919Å was detected and, by use of filters, found to lie between 1600 and 3200Å.

b) This fluorescence was also spectrally analyzed with a monochromator of 150Å resolution and appears to be a continuum lying between 2100 and 3150Å.

c) The emission spectrum arising from electron impact of CF_4 was analyzed with 8Å resolution and for electron energies from 13 to 22 eV this spectrum was a continuum similar to that excited by uv.

d) The short wavelength limits of the emission continuua excited by 919Å photons and 13 to 22 eV electrons were 2100Å and 1850Å respectively. Analysis suggests the final state resulting from these excitations of CF_4 is the CF_3 radical and a fluorine atom.

APPARATUS

Two experimental arrangements are described, one for the fluorescence experiment and another for the electron excitation experiment.

The fluorescence experiment apparatus schematic is shown in Fig. 50. The light source is a Hinteregger type (McPherson Model 630) DC capillary discharge operated windowless with argon flowing from the lamp through the monochromator entrance slit. This source provides sufficient intensity of the AII 919.8Å line to excite the fluorescence of CF_4. The 1 meter McPherson Model 225 normal incidence concave grating monochromator is used with wide (1 mm) entrance and exit slits to maximize throughput of the 919Å line radiation. A McPherson Model 665 dual beam attachment mounted behind the exit slit of the 1 m monochromator serves as the absorption and fluorescence chamber. An oscillating mirror in this device alternately reflects the light emerging from the exit slit to either side of the chamber at 6.6 cps. The beam of 919Å photons is monitored by a photomultiplier tube (A, Fig. 50) preceded by a window coated with sodium salicylate. The fluorescence is detected by an EMI 6256S low noise phototube (B, Fig. 50) mounted behind the exit slit of the 40 cm f/10 monochromator.

A quartz window directly ahead of the sodium salicylate coated window of phototube B rejects any 919Å radiation scattered by the grating of the 40 cm monochromator, since the primary beam of 919Å falls upon this grating. This geometry was chosen to allow observation of fluorescence produced along the entire path of the 919Å radiation through the gas in the scattering chamber. Because the collection efficiency for fluorescent photons varies along the path, quantitative estimation of fluorescent signal strength is difficult. The output of phototube B is detected as pulse counts by a multichannel analyzer. Two modes of data accumulation are employed. For spectral scans, the 40 cm monochromator is scanned slowly through the appropriate wavelength range and phototube pulses are accumulated in successive channels of the multichannel analyzer. Synchronization of channel advance with spectral scan rate of the monochromator produces a histogram type record of the fluorescent spectrum. In addition to the spectral scans, some data are taken by setting the 40 cm monochromator at a particular wavelength and integrating the fluorescent photon counts over a period of time. In this mode of operation the beam splitting mirror oscillates at 6.6 cps, thus chopping the signal, and the multichannel analyzer is synchronized with the chopper so that one group of channels collects only phototube noise counts and another group collects both signal and noise counts. The difference is the signal. This type of phase locked detection insures uniform

sampling of the phototube noise output and allows the detection of signals as small as a few percent of the noise. With the light fluxes and geometry available, such measures were essential to detection of spectrally resolved fluorescence.

Broadband detector observations were obtained using a modification of apparatus shown in Fig. 50 with the beam splitting device used as the scattering chamber. Phototube A was used as the fluorescence detector and the direct beam of 919Å radiation to it was blocked by a baffle so that only the freon on the left side of the scattering chamber was illuminated. A filter wheel in front of phototube A carried LiF, quartz and glass windows which could be positioned in front of the sodium salicylate window ahead of the phototube, thus providing broadband wavelength selectivity. The quartz window transmits at wavelengths longer than about 1600Å and the glass window transmits at wavelengths longer than about 3100Å although its transmission at 2940Å is 10%.

The electron impact excitation of CF_4 employs the 1 m monochromator. The light source (Fig. 50) is replaced by an electron gun and gas target chamber and signals are received by phototube A. In some cases, instead of processing the signals with the multichannel analyzer, DC currents can be measured, because signal to noise ratios are much higher than for the

fluorescence experiment. The electron impact excitation chamber is a cylinder about 5 cm in diameter and 7 cm long mounted ahead of the entrance slit of the 1 m monochromator. The cathode is a thoriated iridium filament behind two grids, adapted from a Varian ion gauge. Electrons are collected by a cylindrical electrode at ground potential. This arrangement is suitable for crude energy resolution experiments ($\sim$ 1 volt). Its principal virtue is its capability for high current operation, though results must be used with care since the electrons are not focused and secondaries are not suppressed. Resolution of the apparatus was established by measuring the onset energy of the N_2^+ 3914Å band. The instrumental correction was found to be the difference between the observed value of 19.6 eV and the known value of 18.75 eV for onset of the (0,0) band.

Absolute sensitivity information for the monochromator used in this experiment is not available. The relative spectral sensitivity of the combination of the 40 cm monochromator and phototube B was observed to be flat to within 20% from 2000 to 3200Å, by comparison of its sensitivity with that of phototube A using the dual beam apparatus shown in Fig. 50. The relative spectral sensitivity of the combination of the 1 m monochromator and phototube A was found to be flat from 2100 to 2400Å and to fall off gradually at longer wavelengths, so that the sensitivity at 2700Å is 70% of

that at 2400Å. This was determined by measurement of relative intensities of CO^+ 1st negative bands and NO γ bands excited by electron impact, using band strength data computed from Franck Condon factors (refs.37,38). The photo tubes were, as always, preceded by sodium salicylate coated windows.

EXPERIMENTAL OBSERVATIONS

The fluorescence of freon (CF_4) was observed in several different ways in the experiments reported here. UV-excited fluorescence was observed with a broadband detector, and with a monochromator providing modest spectral resolution. Electron impact induced fluorescence was observed with better spectral resolution. Our broadband fluorescence observations confirmed, in part, the results of Cook and Ching (ref. 1).

The results of a preliminary broadband experiment showed that most of the fluorescence of CF_4 excited by 919Å radiation was of wavelength longer than 1600Å and shorter than 3000Å, since the quartz filter transmitted it but the glass filter blocked most of it. Further spectral details were determined with the monochromator.

Spectrally resolved fluorescence of CF_4 was obtained with the experimental arrangement of Fig. 50 described above. Because fluorescence signals were very weak, it was necessary to

extract the signal from the phototube dark noise. Entrance and exit slits of the 40 cm monochromator were opened to 3 mm, yielding wavelength resolution of about 150Å. That is, a monochromatic spectral line would appear as a triangular feature with 150Å full width at half maximum intensity. With the light source running steadily and the 919Å line of argon entering the scattering chamber where a pressure of 0.025 torr of CF_4 was maintained by flowing in fresh gas to replace that pumped out through the monochromator slits, the 40 cm monochromator was scanned at 1Å per sec from 1500 to 3500Å. Pulses from phototube B were fed into the multiscaler and counted in 200 successive channels for 10 sec per channel. Each scan thus required 2000 sec, and 18 such scans were summed channel by channel by the multiscaler. Precautions were taken to insure synchronization of starting times of monochromator and multiscaler scans so the wavelength error of the scans was much less than the channel width of 10Å. Readouts of the spectrum were obtained after even numbered scans to allow checks of consistency, described below. The data for all scans were processed by adding together groups of 5 channels (50Å) and plotting the average of successive pairs of 5 channel groups. The result is displayed in Fig. 51a.

Similar analyses of the data taken in the scans 1-10 and 11-18 were plotted separately and confirmed the reproducibility

of the large scale structure in the spectrum at wavelengths longer than 2100Å, but indicated that features below 2100Å are not reproducible. The ordinate of Fig. 51a gives the number of signal counts in 5 channels for 18 scans. The standard deviation of the signal is estimated to be 100 counts/900 sec. The smaller oscillations in the curve plotted in Fig. 51a are within this range and therefore not significant. What is significant is the rise in signal at 2100Å, the dips at 2600Å and 3150Å, and the continuing rise in signal beyond 3200Å. Tests of fluorescent signal counting rate without CF_4 gas show that the spectrum depicted in Fig. 51a is attributable to CF_4 except for the gradual rise at wavelengths longer than 3100Å which is probably a result of scintillation of oils deposited on the beam switching mirror or other surfaces seen by the monochromator. The dashed line extending under the spectrum in Fig. 51a from the right is an estimate of the background radiation which should be subtracted from the signals shown. The true CF_4 fluorescence spectrum seems to be confined to the broad features between 2100 and 3150Å.

A number of electron impact spectra of CF_4 were observed at various electron energies. The spectrum in Fig. 51b was produced with 20 eV electrons. It appears continuous, rising from about 1900Å and extending to longer wavelengths. Again, because of fluctuations in noise, the smaller oscillations are not repeatable.

C-2

For the scan shown, the entrance and exit slits of the 1 m monochromator were set at 2 mm giving spectral resolution of 34Å. More detailed scans of parts of this spectrum with narrower slits failed to show any line or band structure.

The relative excitation cross section curve in Fig. 52 shows the light emitted by CF_4 at 2350Å (in a bandwidth of 34Å) for electron energies between 10 and 45 eV, normalized for variation of electron current with energy. The accuracy of this curve is poorest at low energies where signals are weak, but it tends to show that the electron induced fluorescence of CF_4 sets on below 14 eV and rises gradually to about 22 eV where a sharply rising component starts. From this curve one sees that an electron energy of 20 eV is sufficient to excite the fluorescence but is below that energy at which another process seems to begin. The CF_4 spectrum excited with 20 eV electrons (Fig. 51b) thus should correspond to that excited by 919Å photons (Fig. 51b).

A number of detailed scans of the electron impact spectrum between 1600 and 2100Å were made at electron energies of as low as 14 eV to determine the short wavelength limit of the continuous spectrum. This was found to lie at 1850 ± 10Å and the implications of this are discussed below.

A spectral scan of fluorescence of CF_4 produced by 60 eV electrons was made and has a different shape than

that at 20 eV. This scan was made with spectral resolution of 17Å and shows two continua; one near 1600Å and another at longer wavelengths. This result is much like that of Hesser and Dressler (ref. 39), who observed the same continua with 200 volt electrons. The onset of the 1600Å continuum was observed to occur at about 22 eV. The spectrum excited by 60 eV electrons also shows the CI 1930.93Å line. Figure 53 gives the excitation efficiency of this line as a function of electron energy. The onset occurs at 27.8 ± 1 eV. Table 6 summarizes the observations of continua excited by photon or electron excitation of CF_4.

ENERGETICS OF CF_4 FLUORESCENCE

Conclusions about the identity of radiating species can be drawn from the data on spectral distribution of radiation from CF_4 excited by uv photons or electrons. The electron impact excited spectrum of Figure 51b has a short wavelength limit at 1850 ± 10Å(6.7 eV). This was excited with 20 eV electrons. Similar spectra were excited with electrons of energy as low as 14 eV. Although these are not reproduced here, they all show the continuum with short wavelength limit at 1850Å. Thus, 14 eV electrons excite a state which yields photons of energy as high as 6.7 eV leading to a final state at 7.3 eV.

This result is also obtained by considering the fluorescent spectrum, Fig. 51a which has a short wavelength limit at about 2100Å. This was excited with 919Å photons (13.5 eV). Subtracting 5.9 eV (2100Å) yields 7.6 eV as the energy of the final state, in agreement with that found from the electron impact spectra. This state could be a state of the CF_4 molecule, but the diffuse absorption and emission suggest that dissociation is involved. The energies of the ground states of a number of dissociation products were computed from heat of formation data summarized in Table 7. Based on these data, the energies required to dissociate CF_4 to a radical and some number of fluorine atoms or molecules are summarized in Table 8. The first entry can be verified by considering the excitation function for the CI 1930 line, shown in Fig. 53. Subtracting the energy of the upper state of the line (7.68 eV) from the observed threshold of excitation (27.8 ± 0.1 eV) yields 20.1 eV as computed from the heat of formation data.

Since the final state after emission of a fluorescent photon in the continuum lies as low as 7.3 eV above the ground state of CF_4 the existence of CF_2 or CF as a product is ruled out. This leaves CF_3 + F as the most likely dissociation product, among the possibilities suggested in Table 8.

Table 6

Continua Excited in CF_4

Excitation Process	Short Wavelength Limit of Continuum
Photon 919.78Å (13.5 eV)	2100Å (5.9 eV)
Electrons	
> 13.2 eV*	1850Å (6.7 eV)
> 22 eV	1540Å (8.05 eV)
	2020Å (6.13 eV)

* Our observations of this continuum were made at electron energies > 14 eV. The lower limit is inferred from Cook and Ching's (ref. 1) optical absorption data.

Table 7

Thermochemical Data

Molecule	Heat of Formation (ref. 40)
CF_4	-220.5 kcal/mol
CF_3	-115
CF_2	-30 ± 10
CF	+74.4
C (gaseous state)	+172
F	+18.88

Table 8

Computed Dissociation Energies

Final State	Dissociation Energy
C + 4F	20.1 eV
CF + 3F	> 10 eV
CF + F_2 + F	> 10 eV
CF_2 + 2F	9.8 eV
CF_2 + F_2	8.2 eV
CF_3 + F	6.06 eV

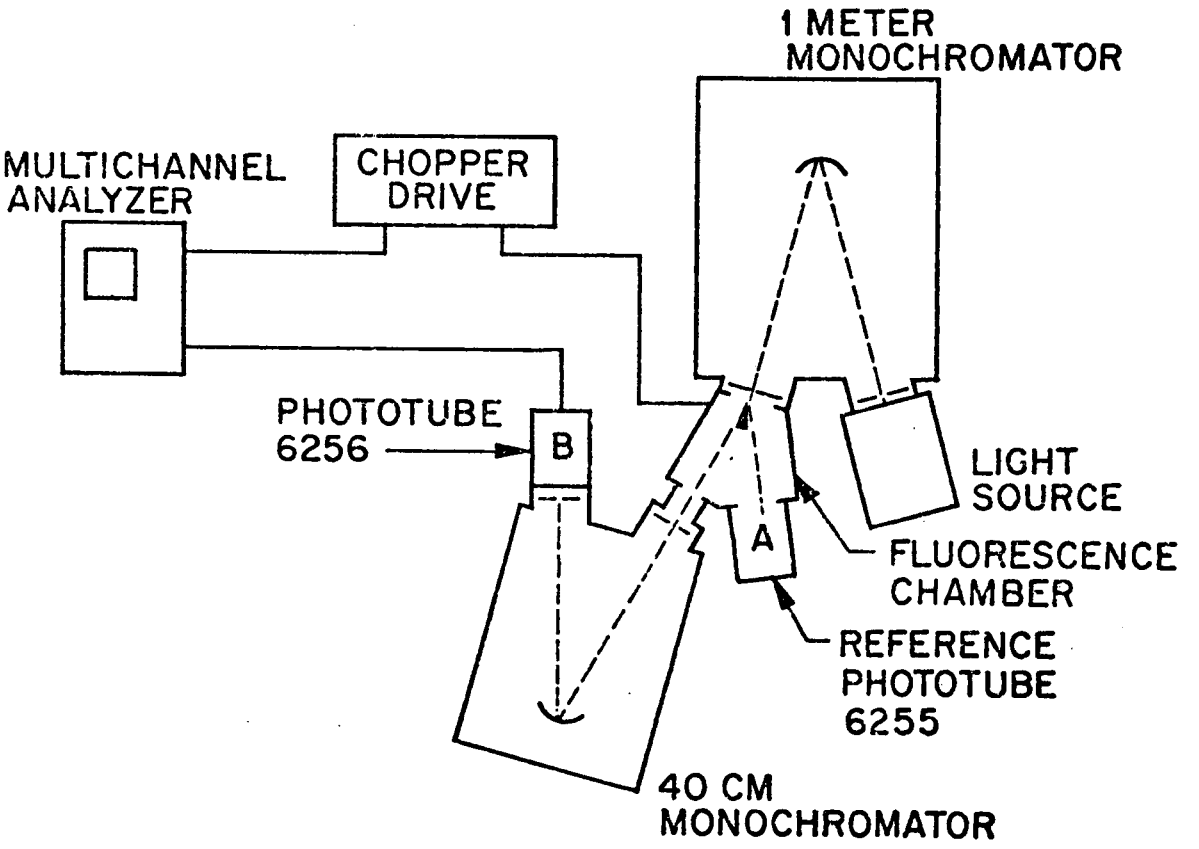

Figure 50 Schematic of apparatus showing arrangement used in making scans of UV excited fluorescence.

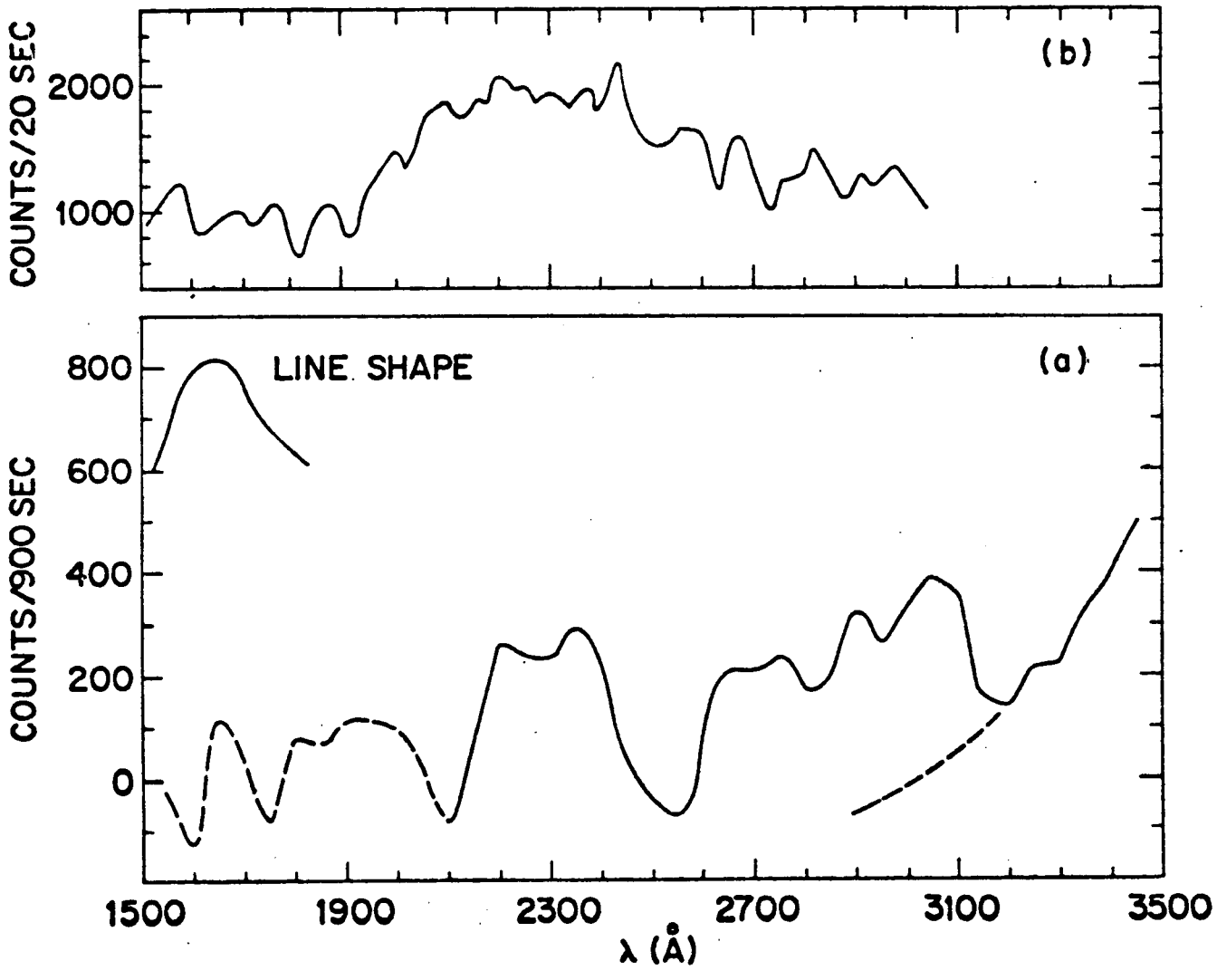

Figure 51 Fluorescence spectrum of CF_4 excited by 919.78Å photons. Shape of a narrow line with
(a,lower) this resolution (150Å) is shown at upper left. (Background of 10,000 counts/900 sec. has been subtracted.)

(b,above) Emission when CF_4 is excited by 20 eV electrons and measured with resolution of 40Å. The smaller oscillations in both curves are not significant.

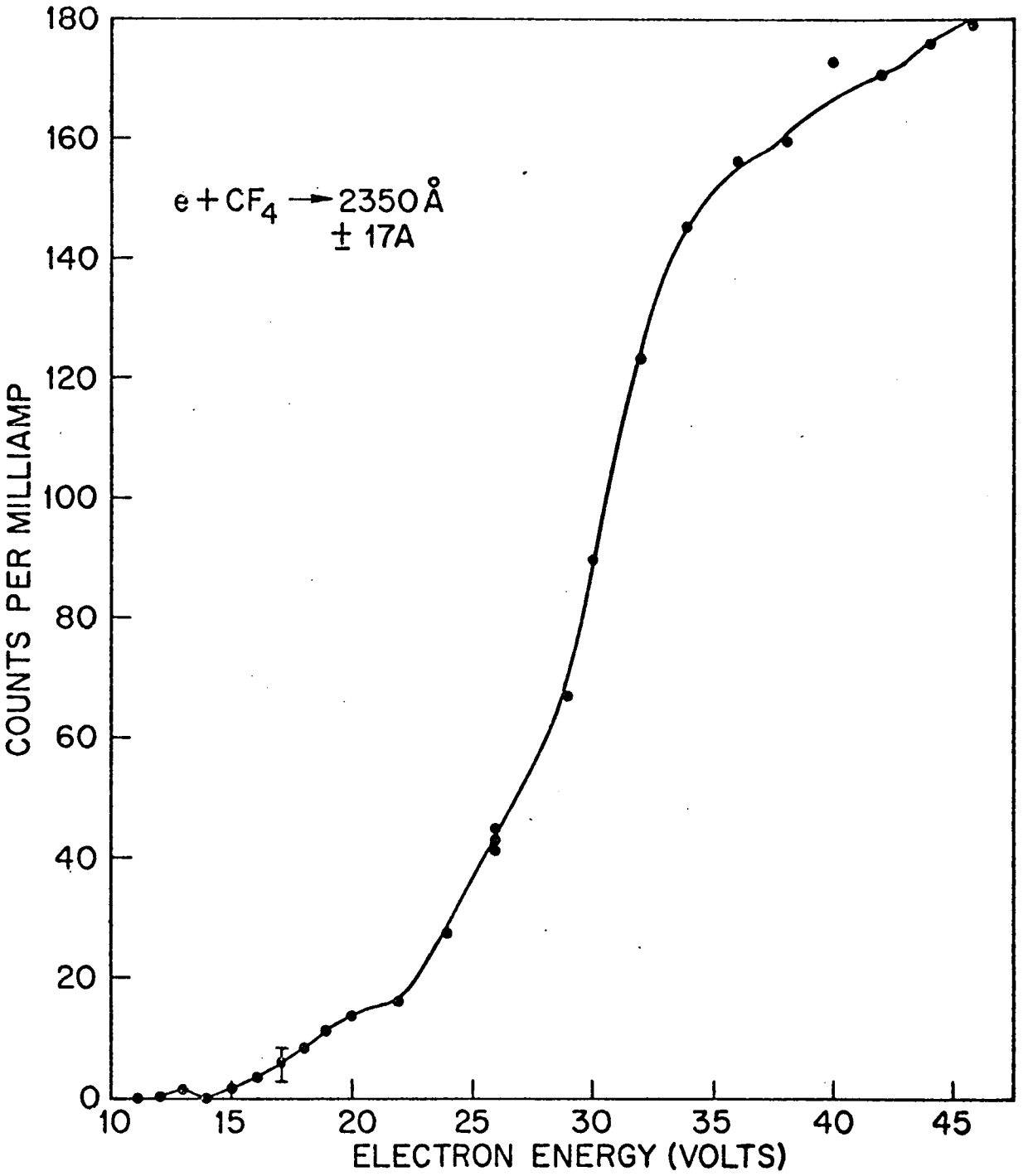

Figure 52 Excitation efficiency of continuum at 2350Å showing onset below 14 eV and sharper rise starting at 22 eV. (Calibration requires subtraction of 0.85 eV from energies on abcissa.)

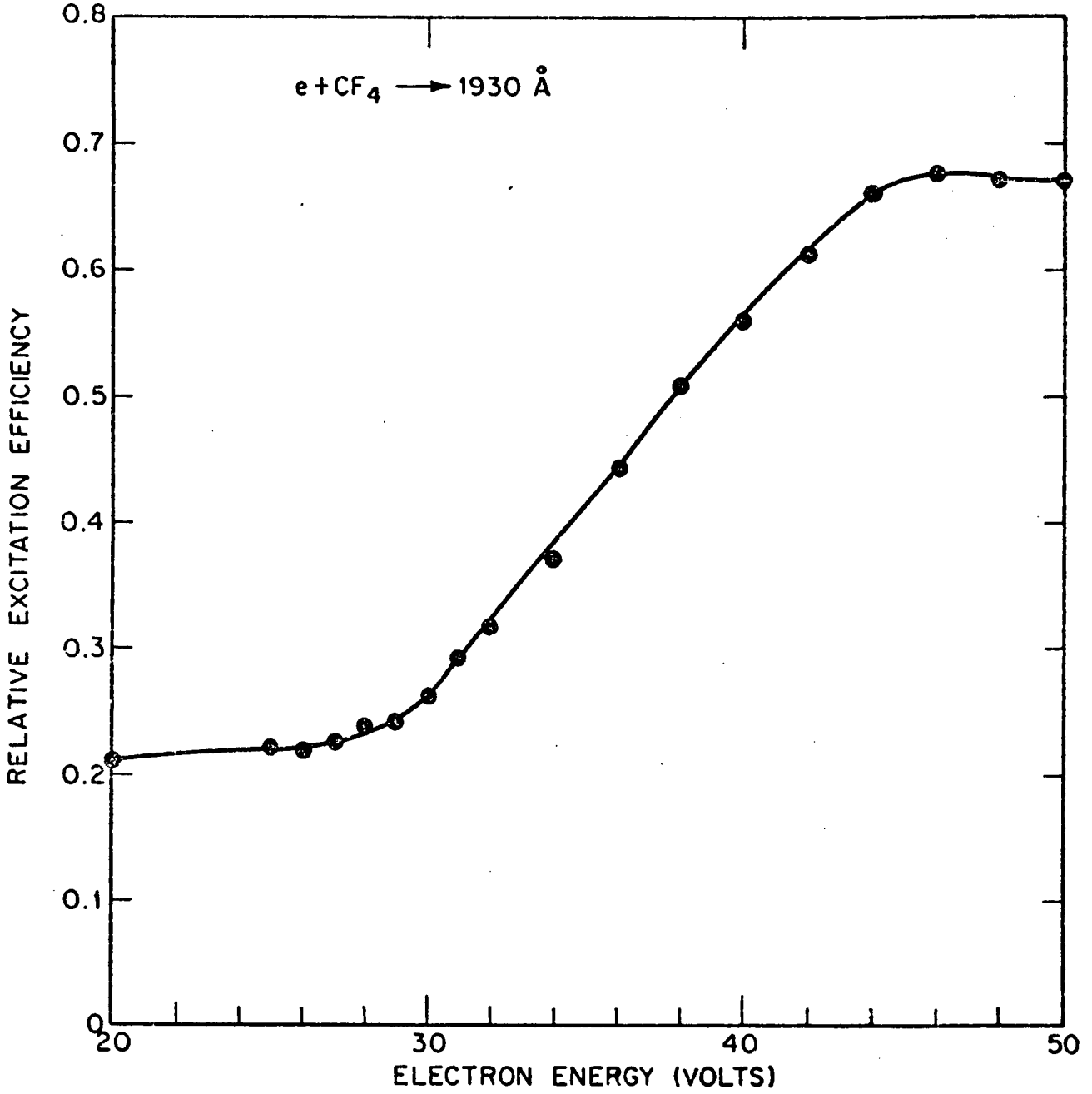

Figure 53 Excitation efficiency of CI 1930.93Å line. (Subtract 0.85 eV from abcissa values.)

REFERENCES

1. Cook, G.R. and B.K. Ching, J. Chem. Phys. 43, 1794 (1965).

2. Pearce, J.B., Lane, A.L. and Barth, C.A., "Mariner 6 and 7 Ultraviolet Spectrometer: In-Flight Measurements of Simulated Jovian Atmosphere" (created from the Dissociation Products of N_2H_4 used as a Course Correction Motor Fuel), Science 172, p. 941 (1971).

3. Barth, C.A., Hord, C.W., Pearce, J.B., Kelly, K.K., Anderson, G.P., and Stewart, A.I., "Mariner 6 and 7 Ultraviolet Spectrometer Experiment: Upper Atmosphere Data," J. Geophys. Res., 76, p. 2213 (1971).

4. Stephens, J.T., "Development of a Source Flow Program to Predict the Flow Field of a High Altitude Plume," LMSC/HREC D162230, Lockheed Missiles and Space Company, Huntsville, Ala., Aug. 1970.

5. Ring, L.R. and M.M. Penny, "Development of a Plume Impingement Analysis Computer Program Employing Source Flow Plume Definition Techniques - With User's Manual," LMSC/HREC D225257, Lockheed Missiles and Space Company, Huntsville, Ala., Sept. 1971.

6. Haukohl, J. and L.W. Spradley,"Multi-Specie Condensation in Expanding Flows," LMSC/HREC D162239, Lockheed Missiles and Space Company, Huntsville, Ala., June 1970.

7. Ames Research Staff, Equation, Tables, and Charts for Compressible Flow NACA TR1135 (1953).

8. JANAF Thermochemical Tables, Dow Chemical Company, Midland, Michigan, 1972.

9. Henke, B.L., Elgin, R.L., Lent, R.E. and Ledingham, R.B., "X-Ray Absorption in the 2 to 200A Region," Norelco Reporter, XIV, 112 (1967).

10. Edgell, W.F. and R.E. Moynihan, "Infrared Band Contours. I. Spherical Top Molecules," J. Chem. Phys., 27, 155 (1957).

11. Schürgers, M. and K.H. Welge, "Absorptionkoeffizient von H_2O_2 and N_2H_4 Zwischen 1200 and 200A," Z. Naturforsch 23a, 1508 (1968).

12. Imanishi, S., "Ultraviolet Absorption and Raman Effect for Hydrazine," Nature, 127, 782 (1931).

13. Giguere, P.A. and I.D. Liu, "On the Infrared Spectrum of Hydrazine," J. Chem. Phys., 20, 136 (1952).

14. Cook, G.R. and B.K. Ching, "Absorption, Photoionization, and Fluorescence of Some Gases of Importance in the Study of the Upper Atmosphere," Air Force Systems Command, SSD TDR-64-16, 30 Jan. 1965.

15. Huffman, R.E., Y. Tanaka, and J.C. Larrabee, "Absorption Coefficients of Nitrogen in the 1000-580A Wavelength Region," J. Chem. Phys., 39, 902 (1963).

16. Ching, B.K., G.R. Cook, and R.A. Becker, "Oscillator Strengths of the a, w, and A and C Bands of N_2," J. Quant. Spec. and Rad. Trans., 7, 323, (1967).

17. Watanabe, K., "Photoionization and Total Absorption Cross Section of Gases, " J. Chem. Phys., 22, 1564 (1954).

18. Nicolet, M., Memoires de La Societe Royale des Sciences de Liege, p. 319 (1961).

19. Sun, H. and G.L. Weissler, "Absorption Cross Sections of Carbon Dioxide and Carbon Monoxide in the Vacuum Ultraviolet," J. Chem. Phys., 23, 1625 (1955).

20. Inn, E. C.Y., K. Watanabe, M. Zehkoff, "Absorption Coefficients of Gases in the Vacuum Ultraviolet, Part III, CO_2," J. Chem. Phys., 21, 1648, (1953).

21. Ogawa, M., "Absorption Cross Sections of O_2 and CO_2 Continua in the Schumann and for UV Regions," J. Chem. Phys., 54, 2550 (1971).

22. Pierson, R.H., A.N. Fletcher, E. Gantz, "Catalog of Infrared Spectra for Quantitative Analysis of Gases," Analytical Chemistry, 28, 1218 (1956).

23. Barrow, G.M., Molecular Spectroscopy, McGraw Hill, New York 1962, p. 145.

24. Penner, S.S., Quantitative Molecular Spectroscopy and Gas Emissivities, Addison-Wesley, Reading, Mass., p. 310 (1959).

25. Hudson, R.D. and L.J. Kieffer, "Compilation of Atomic Ultraviolet Photoabsorption Cross Sections for Wavelengths Between 3000 and 10A," Atomic Data, 2, 205 (1971).

26. Huffman, B.L., Y. Tanaka, J.C. Larrabee, "Absorption Coefficients of Xenon and Argon in the 600-1025A Wavelength Region," J. Chem. Phys., 39, 902 (1963).

27. Wiese, W.L., M.W. Smith, and B.M. Miles, "Atomic Transition Probabilities," Vol. I, Nat. Bur. Stds., NSRDS-NBS-4 (1966).

28. Samson, J.A.R., "Techniques of Vacuum Ultraviolet Spectroscopy," John Wiley, N.Y., (1967).

29. Wiese, W.L., M.W. Smith and B.M. Glennon,"Atomic Transition Probabilities," Vol. I, Nat. Bur. Stds, NSRDS-NBS-4 (1966).

30. Johnson, F.S., Satellite Environment Handbook, published by Stanford University Press, 1961.

31. Hunten, D.M., "Airglow-Introduction and Review, The Radiating Atmosphere," (Proceedings of the Summer Advanced Study Institute, Aurora and Airglow, 1970, ed. by B.M. McCormac), D. Reidel Publ. Co., Dordrecht, Holland (1971).

32. Hinteregger, H.E., L.A. Hall and G. Schmidtke, "Solar XUV Radiation and Neutral Particle Distribution in July 1963 Thermosphere," Space Res. V, p. 1175, (1965).

33. Hesser, J.E., "Absolute Transition Probabilities in Ultraviolet Molecular Spectra," J. Chem. Phys., 48, 2518 (1968).

34. Bahr, J.L., A.J. Blake, J.H. Carver, and V. Kumar, "Photoelectron Spectra and Partial Photoionization Cross Sections for Carbon Dioxide," J. Quant. Spec. Rad. Transfer 9, 1359, (1969).

35. Okabe, H. and M. Lenzi, "Photodissociation of NH_3 in the Vacuum Ultraviolet," J. Chem. Phys., 47, 5241 (1967).

36. Donahue, T.M. and J.B. Kumer, "An Observation of the Helium I 584A Dayglow Between 400 and 1000 km," J. Geophys. Res., 76, 145 (1971).

37. Joshi, K.C., V.D.P. Sastri and S. Parthasarathi, J. Quant. Spectrosc. Rad. Transfer, 6, 215 (1966).

38. Spindler, R.J., L. Isaacson, and T. Wentink, Jr., J. Quant. Spectrosc. Rad. Transfer, 10, 621 (1970).

39. Hesser, J.E. and K. Dressler, J. Chem. Phys., 47, 3443 (1967).

40. Wagman, D.D. et al., NBS Tech. Note 270-3, Jan. 1968, Washington, D.C.